ELECTRON ACCEPTOR MOLECULES DEPOSITED ON EPITAXIAL GRAPHENE STUDIED BY MEANS OF LOW TEMPERATURE SCANNING TUNNELING MICROSCOPY/SPECTROSCOPY

Tesis doctoral presentada por
Manuela Garnica Alonso

Para optar al título de Doctor en Ciencias Físicas
Departamento de Física de la Materia Condensada
Universidad Autónoma de Madrid

Madrid, julio de 2013

Tesis presentada para optar al Grado de Doctor en Ciencias Físicas

Directores de tesis:

Prof. Amadeo López Vázquez de Parga

Prof. Rodolfo Miranda Soriano

Universidad Autónoma de Madrid
Departamento de Física de la Materia Condensada

Instituto Madrileño de Estudios Avanzados
Nanociencia

A todos los que
día a día han estado ahí.

Contents

Resumen

En esta tesis se presenta el estudio de dos moléculas aceptoras de electrones bien conocidas, TCNQ y F_4-TCNQ, sobre grafeno epitaxial. El crecimiento y caracterización de sus propiedades electrónicas y magnéticas se realizó mediante Microscopía y Espectroscopia Túnel de Barrido (STM/STS) en Ultra Alto Vacío y a baja temperatura.

El grafeno epitaxial se crece sobre Ru(0001) y Ir(111) mediante descomposición térmica de moléculas. A pesar de que en ambos casos la superficie de grafeno presenta un patrón de moiré, estos dos sistemas son complementarios en lo que se refiere a la interacción entre el grafeno y el metal. El balance entre las interacciones molécula-molécula y molécula-substrato es estudiada para ambas moléculas a diferentes recubrimientos mediante STM. El grafeno epitaxial nos permite la pasivación de la superficie altamente reactiva del metal permitiendo el estudio de moléculas individuales prácticamente inalteradas así como la formación de diferentes estructuras moleculares autoensambladas.

La espectroscopia túnel de barrido a baja temperatura es utilizada para dar a conocer la estructura electrónica de estas capas moleculares. En el caso de las TCNQ sobre grafeno/Ir(111), las moléculas se mantienen prácticamente neutras debido a la débil interacción con el sustrato. Por otra parte, en el caso de las TCNQ adsorbidas en grafeno/Ru(0001), estos experimentos, en concordancia con cálculos DFT+D2, mostraron la ocupación parcial del LUMO de la molécula de TCNQ neutra. Este orbital se divide en dos orbitales con espines opuestos, SOMO y SUMO. El papel de la capa de grafeno es modular la hibridización entre el electrón desapareado transferido a la molécula y los electrones de conducción del Ru, dando lugar a un efecto Kondo dependiente de la posición de absorción. Esta dependencia es confirmada para recubrimientos mayores de TCNQ y para moléculas de F_4-TCNQ en la misma superficie. Además, el efecto combinado de la interacción atractiva entre las moléculas de TCNQ y la ocupación parcial del LUMO da lugar a la formación de bandas intermoleculares extendidas espacialmente que permiten a las moléculas deslocalizar la carga adquirida. Estas bandas están divididas en espín, con sólo la banda de espín mayoritaria ocupada, como revelaron los cálculos DFT. La existencia del correspondiente orden magnético a largo alcance es detectado mediante experimentos de STM polarizados en espín a 4.6 K. Estos resultados son la primera evidencia experimental y teórica de la existencia de orden magnético a largo alcance en bandas deslocalizadas en una monocapa molecular puramente orgánica.

Abstract

This thesis presents a study of two well-known electron acceptor molecules, TCNQ and F_4-TCNQ, deposited on epitaxial graphene. The growth and characterization of the electronic and magnetic properties of these systems have been performed by means of Low Temperature Scanning Tunneling Microscopy and Spectroscopy (STM/STS) in Ultra High Vacuum.

A graphene layer is grown by chemical vapor deposition on Ru(0001) and Ir(111) surfaces. Although in both cases the graphene surface presents a moiré superstructure, these two systems are completely different from the graphene-metal interaction point of view. The relative strength between the molecule-molecule and molecule-substrate interactions is systematically studied for both molecules at different molecular coverages by means of STM. The epitaxial graphene passivates the highly reactive metallic surfaces allowing the study of almost unperturbed single molecules and the formation of self-assembly molecular structures.

Low temperature scanning tunneling spectroscopy is used to unveil electronic structure of these molecular layers. In the case of TCNQ on graphene/Ir(111), the weak molecule-substrate interaction keeps the molecules practically neutral. On the other hand, in the case of TCNQ deposited on graphene/Ru(0001), these experiments, in agreement with DFT+D2 calculations, reveal the partial occupation of the LUMO of the neutral TCNQ molecule. This orbital splits into a spin-up SOMO and a spin-down SUMO. We find that the graphene layer modulates the hybridization between the transferred unpaired electron and the Ru conduction electrons leading to a site dependent Kondo effect. This dependence is further confirmed for higher TCNQ coverages and for F_4-TCNQ molecules on the same surface. In addition to that, the combined effect of the attractive interaction between TCNQ molecules and the partial occupation of the LUMO gives rise to the formation of spatially extended intermolecular bands, that allow the molecules to delocalize the charge acquired. The bands are spin split, with only the majority spin band being occupied as revealed in the DFT calculations. The existence of the corresponding long-range magnetic order is detected by spin polarized STM at 4.6 K. These findings are the first experimental and theoretical evidence for the existence of long-range magnetic order in delocalized bands in a purely organic molecular monolayer.

List of Acronyms

STM Scanning Tunneling Microscope

STS Scanning Tunneling Spectroscopy

LT-STM Low Temperature Scanning Tunneling Microscope

VT-STM Variable Temperature Scanning Tunneling Microscope

SP-STM Spin Polarized Scanning Tunneling Microscope

SP-STS Spin Polarized Scanning Tunneling Spectroscopy

LEED Low-energy Electron Diffraction

TCNQ 7,7,8,8-Tetracyano-*p*-quinodimethane

F_4-TCNQ 2,3,5,6-Tetrafluoro-7,7,8,8-tetracyano-*p*-quinodimethane

DFT Density Functional Theory

UHV Ultra High Vacuum

FFT Fast Fourier Transform

DOS Density of States

LDOS Local Density of States

PDOS Projected Density of States

vdW van der Waals

HOMO Highest Occupied Molecular Orbital

LUMO Lowest Unoccupied Molecular Orbital

SOMO Single Occupied Molecular Orbital

SUMO Single Unoccupied Molecular Orbital

1 Introduction

The development of new organic electronic devices has generated a great deal of interest in the last decades. Notably, the growth of organic thin films on surfaces offers the opportunity of manufactured low cost devices with a broad range of new applications. To this aim, the first challenge is the design and synthesize of novel organic materials with the appropriated properties. In particular, small molecules based on carbon constitute promising building blocks to construct advanced materials. The further step is the adsorption of these organic precursors on solid surfaces and the investigation of the formation of long-range ordered surface assemblies. Considering that the molecular self-assembly on surfaces is a competition between molecule-molecule interaction and molecule-substrate interaction, a fundamental role is then played by the choice of the surface.

The ability of the Scanning Tunneling Microscope (STM) to obtain real space images of surfaces at atomic scale has played an important role in the understanding of basic phenomena occurring on surfaces since its invention in 80s by Gerd Binnig and Heinrich Rohrer [1]. In addition, it offers the possibility to characterize the electronic and magnetic properties of a surface by Scanning Tunneling Spectroscopy (STS) and Spin Polarized Scanning Tunneling Spectroscopy (SP-STS). Nevertheless, one of the great attractions of the STM nowadays is its ability to chemically identify and resolve the electronic states of organic molecules on surfaces with intramolecular resolution. These facilities convert STM in the perfect tool for the characterization of organic thin films and their interaction with solid surfaces. For this purpose, it is essential to work in Ultra High Vacuum (UHV) and low temperature. UHV environment maintains the sample surface in a known condition without contamination during the time scale of the experiments and ensures an atomic scale control of the molecular species. On the other hand, low temperature provides the required stability and energy resolution for the local spectroscopy measurements.

In this thesis, we study the molecular self-assembly of well known electron acceptor molecules, TCNQ and F_4-TCNQ, on epitaxial graphene. The molecular adsorption behavior and the electronic and magnetic properties of these systems are investigated by means of Low Temperature Scanning Tunneling Microscopy and Spectroscopy.

The adsorption of molecules on graphene has became a very active field of research in recent years, for the possibility not only of self-assemble and characterize organic thin films but also to tailor the electronic properties of graphene. Since the isolation of a single graphene flake by the group in Manchester in 2004, graphene has attracted a wide range of attention

from both a fundamental point of view and technological applications. For practical applications, however, large scale graphene samples supported on substrates have to be obtained. In this context, epitaxial graphene on metallic substrates have been demonstrated to be scalable to large-area production. On the other hand, the appearance of moiré superstructures due to the difference in lattice parameters between graphene and metals, converts the surface into an ideal playground to explore the mutual interaction between organic molecules in two dimensions. Depending on the metal, the interactions with the graphene and the final surface morphology are different, leading to different templates. The combination of both choices, metal and organic precursors, allows us to control the supramolecular structures and the electronic or magnetic properties of the system. This opens the possibility to add new functionalities to graphene.

1.1 Outline of the thesis

Motivated by this introduction, this thesis is organized as follows:

Chapter 2 gives a description of the experimental methods and set-up used in the course of this thesis. We firstly describe the basics and operational modes of a STM. It follows an introduction of elastic STS which provides a spatially resolved electronic map of the surface LDOS. Taking into account that the aim of the thesis is the study of organic molecules on surfaces we pay special attention to this particular case describing also the inelastic tunneling spectroscopy. We also consider the use of magnetic tips to resolve the magnetic properties of the surface by means of spin-polarized STS which is the experimental method used in the Chap.6. The chapter concludes with an overview of the instrumentation used in details.

In **Chapter** 3 a brief introduction to the growth of graphene on transition metals is given. Ultra-thin epitaxial films of graphite have been grown on solid surfaces since 1960s. However, the characterization of these films was hampered by the experimental limitations existing at that time. In the last years several groups have taken advantage of local probe techniques to study the geometric and electronic structure of graphene epitaxially grown on different metallic substrates. In particular, the most important characteristics of graphene/Ru(0001) and graphene/Ir(111) are described as to complementary examples from the graphene-metal interaction point of view.

Chapter 4 is devoted to the study of the adsorption of two electron acceptor molecules, TCNQ and F_4-TCNQ, on graphene growth on Ru(0001) and Ir(111). The subtle balance between molecule-molecule interaction, attractive for TCNQ and repulsive for F_4-TCNQ, and substrate-molecule interaction will determine the molecular self assembly. The effect of these

interactions on the molecular adsorption behavior is investigated by means of STM for each molecule in graphene grown in both substrates.

In **Chapter** 5 a combination of STS measurements and Density Functional Theory (DFT) calculations are used to elucidate the electronic properties of TCNQ on graphene/Ru(0001) and graphene/Ir(111). A complete analysis from single molecules to monolayer is given in both systems. The acquired charge and the formation of intermolecular bands in the case of TCNQ molecules on graphene/Ru(0001) unlike graphene/Ir(111) will add new properties to the organic layer that will be discussed in the next chapter.

Chapter 6 focuses on the magnetic properties of TCNQ molecules on graphene/Ru(0001). We will discuss the development of magnetic moment on single TCNQ molecules on graphene/Ru(0001) that is preserved upon monolayer formation. The appearance of a magnetic moment is verified by measuring the corresponding Kondo resonance with Local Tunneling Spectroscopy at low temperature. We find a dependence of the Kondo effect on the adsorption site which is further confirm for F_4-TCNQ adsorbed on graphene/Ru(0001). Furthermore, the existence of a long-range magnetic order on the TCNQ monolayer will be detected by SP-STS measurements at 4 K.

Finally, the results presented in this thesis are summarized in **Chapters** 7 and 8, followed by the bibliography and the list of publications.

2 Experimental Methods and Set-up

In this chapter, we review the physics, operation modes and characteristic of STM and the experimental set-up used in the course of this thesis. Firstly, a brief introduction of the basics of STM and the spectroscopy modes will be made followed by an overview of the instrumentation used.

2.1 Scanning Tunneling Microscope (STM)

One of the most important scientific advance in surface physics was the invention of the STM by G. Binnig and H. Rohrer at IBM Zürich in 1981 [1]. The STM is an imaging technique which provides direct, real-space information about the geometric and electronic structure of a surface with atomic resolution.

2.1.1 Basics

The operational principle of the STM is simple. A metallic tip approaches close enough to a conducting surface in such a way that a current can flow due to a quantum effect known as tunneling. Classically, the electrons from the tip (or the surface) cannot cross the potential barrier between them when the energy of the electron is lower than the potential barrier height. However according to quantum physics, electrons are described by wavefunctions which extend into the barrier and decay exponentially with its width and height. For a small distances between the tip and the surface, the tails of the wavefunctions overlap and the electrons can cross the barrier. The resulting tunneling current is related with the Density of States (DOS) at both tip and sample and is used to interpret the structure of the surface.

A schematic representation of a STM is shown in the Fig. 2.1. The tip position is controlled by a piezoelectric elements and a feedback circuit keeps the tunneling current constant by controlling the distance between tip and sample. Finally, a computer displays the data in addition to controlling the feedback and the tip position. In the most common mode, the so called constant current mode, the tunneling current is kept constant by means of a feedback loop meanwhile the tip scans over the surface, see Fig. 2.1. From this method, a map of the surface can be obtained registering the distance changes between the tip and surface to keep the tunneling current constant while moving the tip along the surface. Alternatively, the tunneling current can be recorded meanwhile the tip scans the surface at a constant height,

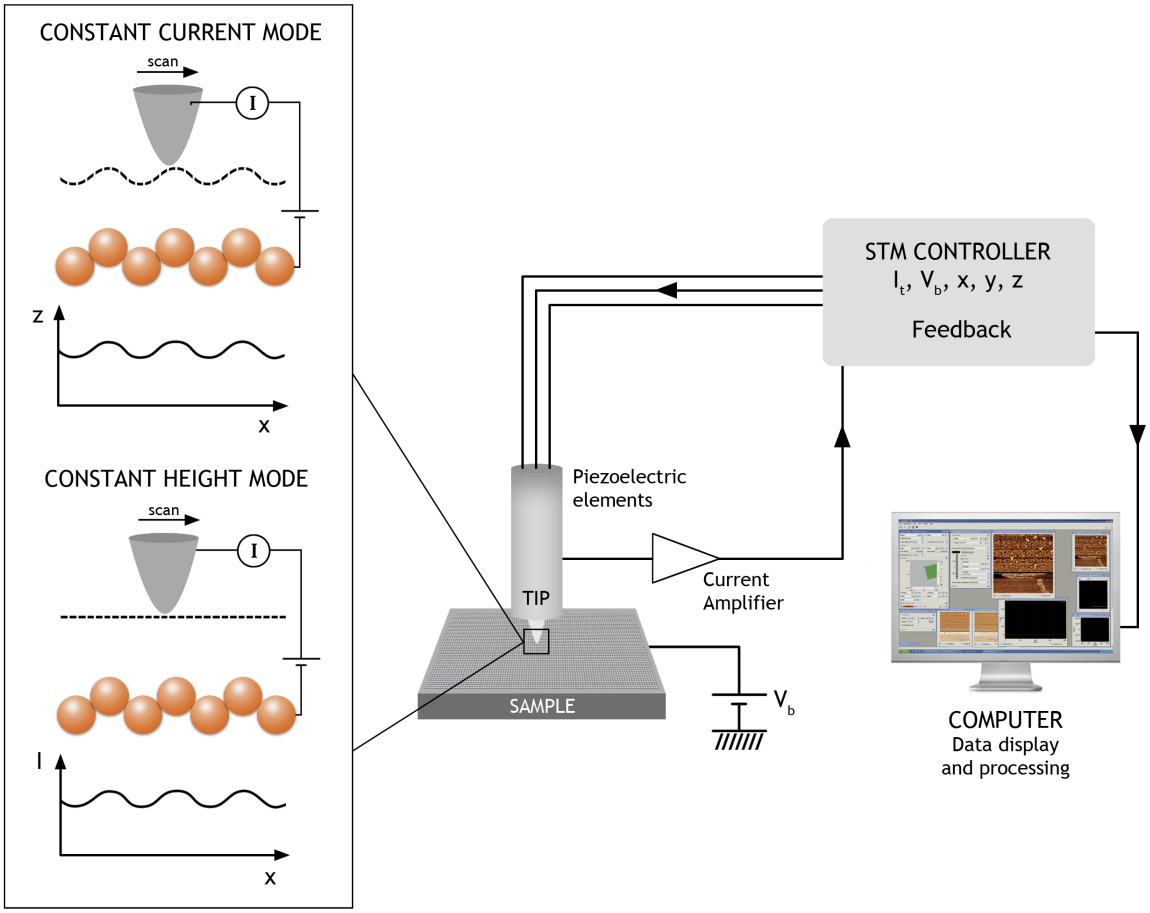

Figure 2.1: Alt Schematic representation and different topographic modes of STM operation. The tip is mounted in a piezoelectric elements for positioning and a feedback system controls the tip-sample distance during the scan. A software displays the data in addition to controlling the feedback and the position of the tip.

this is the so called constant height mode, but requires an atomically flat surface.

2.1.2 Theory of STM

A theoretical approach for understanding the dependence of the tunneling current on the states of the tip and surface will be described in this subsection. Most of the theoretical treatment to the tunneling process are based on the work of J. Bardeen in 1960 [2] to study metal-oxide-metal tunnel junctions. In first-order Bardeen's formalism, the tunneling current can be written as follows:

$$I = \frac{2\pi e}{\hbar} \sum_{\mu\nu} f\left(E_\mu\right) \left[1 - f\left(E_\nu + eV\right)\right] \left|M_{\mu\nu}\right|^2 \delta\left(E_\mu - E_\nu\right), \tag{2.1}$$

where $f(E)$ is the Fermi function, V is the applied voltage between the tip and the surface, $|M_{\mu\nu}|$ is the matrix element between μ states of the tip and ν states of the surface, and E_μ and E_ν are the energy of the electronic states for tip and the surface. In the Bardeen formalism, $|M_{\mu\nu}|$ depends only on the wave functions of the tip ψ_μ and surface ψ_ν and can be calculated as:

$$M_{\mu\nu} = \frac{\hbar^2}{2m} \int d\mathbf{S} \cdot \left(\psi_\mu^* \nabla \psi_\nu - \psi_\nu \nabla \psi_\mu^* \right), \tag{2.2}$$

where the integral is performed over any plane within the barrier. In order to obtain a quantitative value for the tunneling current, the states ψ_μ and ψ_ν have to be calculated. In 1983, J. Tersoff and D.R. Hamann [3] developed a theory of STM based on the general formalism describe above. They treated the surface as a normal electrode, while the tip was modeled as a locally spherical potential well approached to the surface. Then, the surface wave function was described in the form:

$$\psi_\nu = \frac{1}{\Omega_s^{1/2}} \sum_G a_G exp \left[\left(k^2 + |\mathbf{k_G}|^2 \right)^{1/2} z \right] exp \left(i \mathbf{k_G} \cdot \mathbf{x} \right), \tag{2.3}$$

where Ω_s is sample volume, $k = (2m\Phi)^{1/2}/\hbar$ is the decay length in vacuum, Φ is the work function, $\mathbf{k_G} = \mathbf{k}_\parallel + \mathbf{G}$ is the wave vector where $\mathbf{k}_\parallel$ is the surface Bloch wave vector of the states and $\mathbf{G}$ is a surface reciprocal lattice vector. In the case of the tip, the wave function is described by asymptotic spherical form:

$$\psi_\mu = \frac{1}{\Omega_t^{1/2}} c_t k R e^{kR} \left(k|\mathbf{r} - \mathbf{r_0}| \right)^{-1} e^{-k|\mathbf{r}-\mathbf{r_0}|}, \tag{2.4}$$

where Ω_t is the tip volume and R is the local radius located in the center of curvature of the tip $\mathbf{r_0}$, and d is the distance of nearest atom approach to the surface. Expanding the tip wave function in the same form as the surface and neglecting the possible angular dependence of ψ_μ, the matrix element 2.2 can be evaluated. The result is:

$$M_{\mu\nu} = \frac{\hbar^2}{2m} \frac{4\pi}{k\Omega_t^{1/2}} k R e^{kR} \Psi_\nu \left(\mathbf{r_0} \right). \tag{2.5}$$

For low temperatures, if $k_B T$ is small, the Fermi function can be approximated by a step function. Thus, substituting into 2.1 the tunneling current is given by:

$$I = \frac{32\pi^3}{\hbar k^4} e^2 V \Phi^2 R^2 e^{2kR} \frac{1}{\Omega_t} \sum_{\nu\mu} |\Psi_\nu \left(\mathbf{r_0} \right)|^2 \delta \left(E_\mu - E_F \right) \delta \left(E_\nu - E_F \right). \tag{2.6}$$

One can introduce the concept of Local Density of States (LDOS) per energy interval for the tip and the surface as follows:

$$\rho_s\left(E,\mathbf{r_0}\right)=\sum_{\nu}|\Psi_\nu\left(\mathbf{r_0}\right)|^2\delta\left(E_\nu-E_F\right), \tag{2.7}$$

$$\rho_t\left(E_F\right)=\frac{1}{\Omega_t}\sum_{\mu}\delta\left(E_\mu-E_F\right). \tag{2.8}$$

Note that $\rho_s\left(E,\mathbf{r_0}\right)$ is the surface LDOS at the tip position $\mathbf{r_0}$. Thus, the tunneling current expression can be rewritten as:

$$I\propto\sum_{\nu}|\Psi_\nu\left(\mathbf{r_0}\right)|^2\delta\left(E_\nu-E_F\right)\equiv\rho_s\left(E,\mathbf{r_0}\right) \tag{2.9}$$

In this approximation, the current is just proportional to the surface LDOS at the tip position because the tip is considered atomically sharp and with a constant LDOS. This simple model was extended by N. Lang [4], who recalculated the tunneling current considering the tip and the sample as two planar metallic electrodes with a small bias voltage between them and one adsorbed atom on each electrode. Including these assumptions, the tunneling current in the energy window eV is:

$$I\propto\int_{E_F}^{E_F+eV}dE\,\rho_t\left(E-eV\right)\rho_s\left(E\right)T\left(z,E,eV\right). \tag{2.10}$$

$T\left(z,E,eV\right)$ is a transmission coefficient for an electron in the tunnel barrier. The Eq. 2.10 highlights the difficulties in the interpretation of the STM data due to the fact that the tunneling current is a convolution of the density of states of the tip and sample modulated by the transmission coefficients. In the next section a description of how to interpret the electronic information will be detailed.

2.2 Scanning Tunneling Spectroscopy (STS)

Following the theoretical description of the tunneling current, it is possible to see that STM is a powerful tool to resolve the electronic states of a surface with subnanometer spatial resolution. In that sense, the STS provides a spatially resolved electronic map of the surface LDOS. Firstly in this section, we will describe the elastic STS technique. Because this thesis investigates the adsorption of molecules on graphene, we also study the tunneling process across a molecule and the inelastic process associated with the excitation of vibrational modes in the molecules. Finally, we consider the use of magnetic tips to resolve the magnetic properties of the surface by means of spin-polarized STS, to study the magnetic moment acquired by the molecules deposited on graphene, Chap. 6.

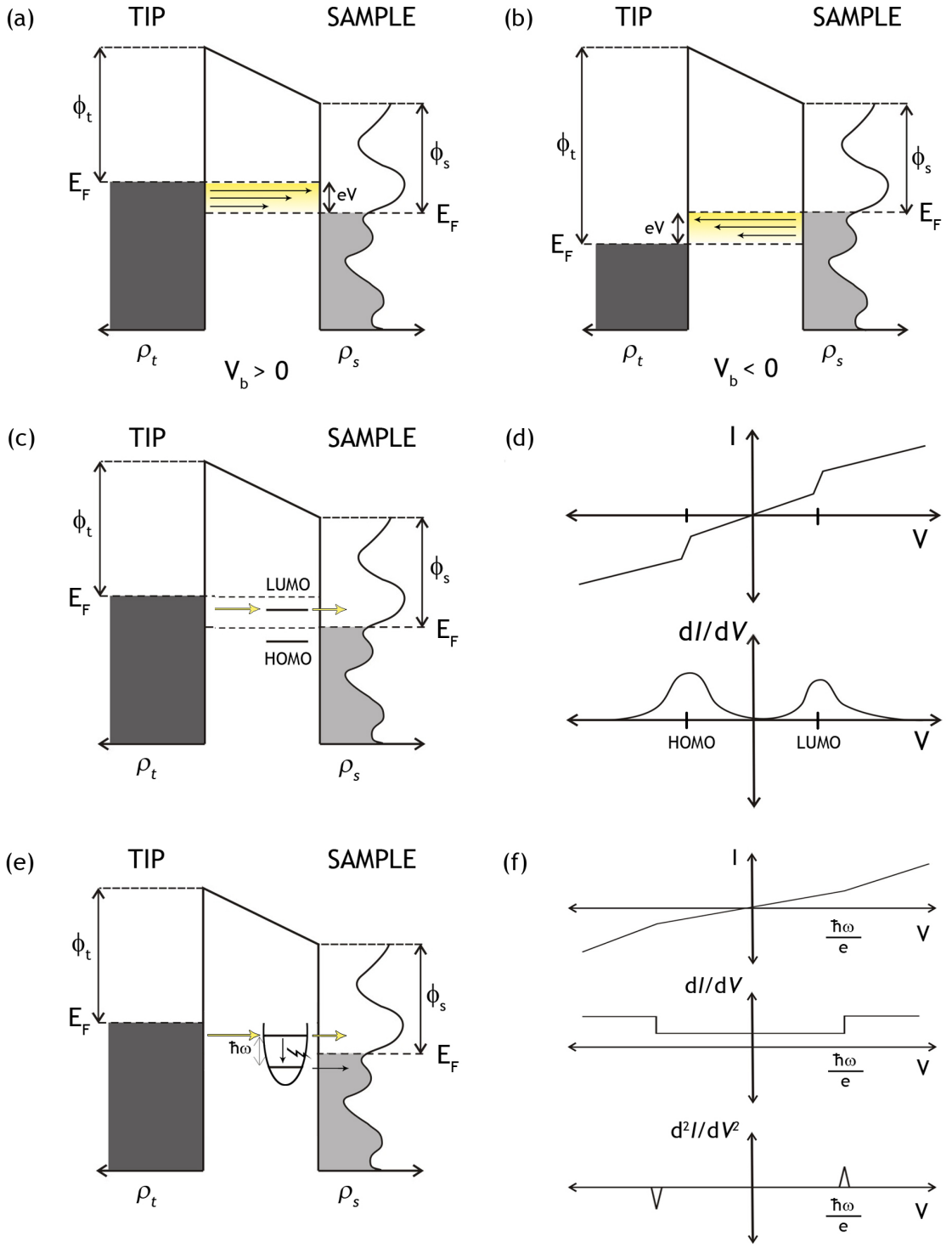

Figure 2.2: Energy diagram for a tunnel barrier in the constant tip LDOS approximation. (a) For a positive bias voltage $V_\mathrm{b} > 0$ and (b) for negative bias voltage $V_\mathrm{b} < 0$. The size of the arrows within the tunneling barrier sketches the dependence on the tunneling probability with the bias voltage. (c) Schematic energy diagram for STS through a molecule and (d) the corresponding I/V and $\mathrm{d}I/\mathrm{d}V$ spectra where the molecular levels are indicated. (e) Inelastic STS energy diagram and (f) the consequences of opening of the inelastic channel in the I/V, $\mathrm{d}I/\mathrm{d}V$ and $\mathrm{d}^2I/\mathrm{d}V^2$ signal.

2.2.1 Elastic STS

As demonstrated before, the tunneling current can be calculated from Eq. 2.10. In the semi-classical Wentzel-Kramers-Brillouin (WKB) approximation, the tunneling transmission coefficient is given by:

$$T\left(z,E,eV\right)=exp\left(-\frac{2z\sqrt{2\pi}}{\hbar}\sqrt{\left(\frac{\Phi_s+\Phi_s}{2}\right)+\left(\frac{eV}{2}\right)-E}\right). \tag{2.11}$$

Accordingly, the transmission coefficient depends on the bias voltage V applied between the tip and the sample being largest when $E=0$ for negative bias ($eV<0$) or $E=eV$ for positive bias ($eV>0$). In Fig. 2.2a and 2.2b, the size of the arrows within the tunneling barrier sketches the dependence on the tunneling probability with the bias voltage. For positive bias voltage, electrons from the vicinity of the Fermi energy of the tip can cross the tunnel barrier and go into the unoccupied states of the sample. Contrariwise, at negative voltages, the tunnel current comes from the electrons from occupied states around the Fermi level of the sample that go into unoccupied states of the tip. Therefore, the STM can be used in the spectroscopy mode to access the LDOS of the sample but in an asymmetric way with more resolution for the unoccupied sample DOS. The derivative of the current-voltage spectrum provides a direct information of the LDOS of the surface, where at a specific point on the surface, while the feedback is switched off, the tunneling current is recorded as a function of a varying bias voltage, an the resulting derivative is proportional to LDOS:

$$\mathrm{d}I/\mathrm{d}V\propto\rho_s\left(E\right). \tag{2.12}$$

The most common way to perform the STS experiments is the acquisition of a spatial map of the $\mathrm{d}I/\mathrm{d}V$ signal. It consists of the acquisition of a spectrum at each pixel of the topographic image in the constant current mode. During the scan, the tip stops at each pixel of the image and for a fixed distance between the tip and the sample determined by the set point parameters, the feedback circuit is switched off and the bias voltage is ramped at the same time that the current is registered. This method allows us to build real-space images of the surface LDOS.

In the same way, we can use STS experiments to extract information about the electronic states of molecules adsorbed on surfaces. Figure 2.2c shows the sketch of these experiments. When a molecule is deposited on a surface, its molecular levels are generally broadened and shifted due to the interaction with the surface. When the interaction is weak, the molecules preserve their molecular fingerprints in such way that in the STS experiments, when the bias voltage tunes one of the molecular orbital levels of the molecule, the resulting $\mathrm{d}I/\mathrm{d}V$ spectra will present a peak which corresponds to that molecular orbital, Fig. 2.2d. Likewise, in the

topographic mode under specific bias parameters the STM images can reveal intramolecular resolution characteristics of their molecular orbitals.

2.2.2 Inelastic STS

An intrinsic characteristic of the molecules is the molecular vibration, and inelastic tunneling spectroscopy is a useful technique to obtain local information about the excitation processes of a molecule. Figure 2.2e shows a schematic representation of this inelastic process. In an STS experiment, when the applied bias voltage is higher than a quantum of vibration of the molecule, a new channel, the inelastic channel, is opened in the tunneling process. Therefore, the tunneling current will increase for $|eV| > \hbar\omega$ because a fraction of electrons can tunnel trough the molecule and excite its internal states. In practice, a change in the slope of the I/V spectra occurs leading to the appearance of steps in the conductance spectra and peaks in the $\mathrm{d}^2I/\mathrm{d}V^2$ spectra as can be seen in Fig. 2.2f. The inelastic peaks in the $\mathrm{d}^2I/\mathrm{d}V^2$ curves appear symmetrically in energy around the Fermi level.

Molecular vibrations have energies in the range of a few tenths of meV and the innelastic channel represents, in the most favorable case, less than 10 % of the tunneling current. Consequently, to detect the weak $\mathrm{d}^2I/\mathrm{d}V^2$ signal, a high resolution in energy and high stability in the tunnel junction are required, or in other words, low temperatures and lock-in techniques are necessary. The lock-in technique consists of adding a small *ac* modulation with a frequency, higher than the frequency response of the feedback circuit, to the bias voltage. By means of the lock-in the tunneling current, oscillating with the frequency superimposed in the bias voltage, is detected. By applying a Fourier expansion, the resulting tunneling current can be decomposed in the base of the applied modulation frequency ω [5]:

$$I\left(V,t\right) = I_0(V) + \varepsilon\frac{\mathrm{d}I}{\mathrm{d}V}\cos\left(\omega t\right) + \frac{\varepsilon^2}{4}\frac{\mathrm{d}^2I}{\mathrm{d}V^2}\cos\left(2\omega t\right) + \cdots \tag{2.13}$$

where ε is the *ac* voltage modulation with frequency ω, and t is time. The detection of the response oscillating with frequency 2ω with a lock-in instruments will provide a value proportional to $\mathrm{d}^2I/\mathrm{d}V^2$. Experimentally, the *dc* signal is scanned along the energy window of interest, searching for features in the $\mathrm{d}^2I/\mathrm{d}V^2$ signal. These experiments require a very high stability because, in order to enhance the signal to noise ratio, long integration times are needed. Thus, low temperatures are necessary to improve the quality of the spectra as well as to maximize the temporal averaging of the measurements. However, the interpretation of the spectra is not straightforward because upon a molecule adsorb in a surface, the molecular conformation may change and these perturbations may produce new vibrational states as well as a shift of the vibrational frequencies known for the molecules in the gas-phase.

2.2.3 Spin polarized STS

In this subsection, we will briefly describe spin polarized spectroscopy mode which offers the possibility to investigate the magnetic properties of a surface at the atomic-scale [6]. The combination of this technique with the previous ones will provide a complete description of a surface.

The idea of SP-STS is to use a magnetic tip to scan a magnetic surface, as shown in Fig.2.3a. In most cases, the magnetic tips are made by covering clean W tips with a magnetic material, controlling the thickness, the sensitivity of the tips can be switched from in-plane to out of plane [6]. In the representation in the Fig. 2.3b, it is possible to see how in this case the spin-up band is different than the spin-down band resulting in a spin polarization of the tunnel current. The polarization is defined by the difference between the number of electrons in minority and majority bands:

$$P_{t,s}(E) = \frac{\rho^{\uparrow}_{t,s}(E) - \rho^{\downarrow}_{t,s}(E)}{\rho^{\uparrow}_{t,s}(E) + \rho^{\downarrow}_{t,s}(E)}. \tag{2.14}$$

Considering the Eq. 2.10 as starting point and assuming a constant LDOS for the tip, D. Wortmann *et al.* [7] obtained the following expression for the the tunneling conductance in the limit of a small applied bias voltage:

$$\mathrm{d}I/\mathrm{d}V \propto n_t n_s \left(1 + P_t P_s \cos\theta\right), \tag{2.15}$$

where $n_t = \rho^{\uparrow}_t + \rho^{\downarrow}_t$ and $n_s = \rho^{\uparrow}_s + \rho^{\downarrow}_s$ are the total density of states of the tip and the sample, respectively. According to Eq. 2.15 in the SP-STS experiments, the tunneling conductance depends on the spin polarized LDOS at the Fermi energy of the tip and the surface and on the relative orientation of their magnetization axes. Thus, the intensity of the spin polarized $\mathrm{d}I/\mathrm{d}V$ signal will be at maximum (minimum) for parallel (antiparallel) magnetization directions of the tip and the surface, $\theta = 0^\circ$ ($\theta = 180^\circ$), and it will vanish for $\theta = 90^\circ$.

In order to test the magnetic sensitivity of our Fe covered tips Spin Polarized Scanning Tunneling Microscope (SP-STM) experiments were performed on Mn thins films grown on Fe(001) (see Fig 2.3c and 2.3d). Mn thins films grown on Fe(001) present a layered antiferromagnetic structure. Therefore, the surface magnetization is in opposite direction in adjacent atomic terraces. Due to the Fe thickness used to cover the W tips, the tips are sensitive to the in-plane magnetization. Figure 2.3c shows a topographic STM image of a screw dislocation on a Mn film 7 monolayer thick. Around the screw dislocation, the local Mn thickness increases smoothly by one atomic layer around the core of the screw dislocation. The difference in the angular orientation of the magnetization of tip and sample gives rise to a contrast in the $\mathrm{d}I/\mathrm{d}V$ map at $+0.2\,\mathrm{V}$ in this area as expected from the layered antiferromagnetic structure, see Fig. 2.3d.

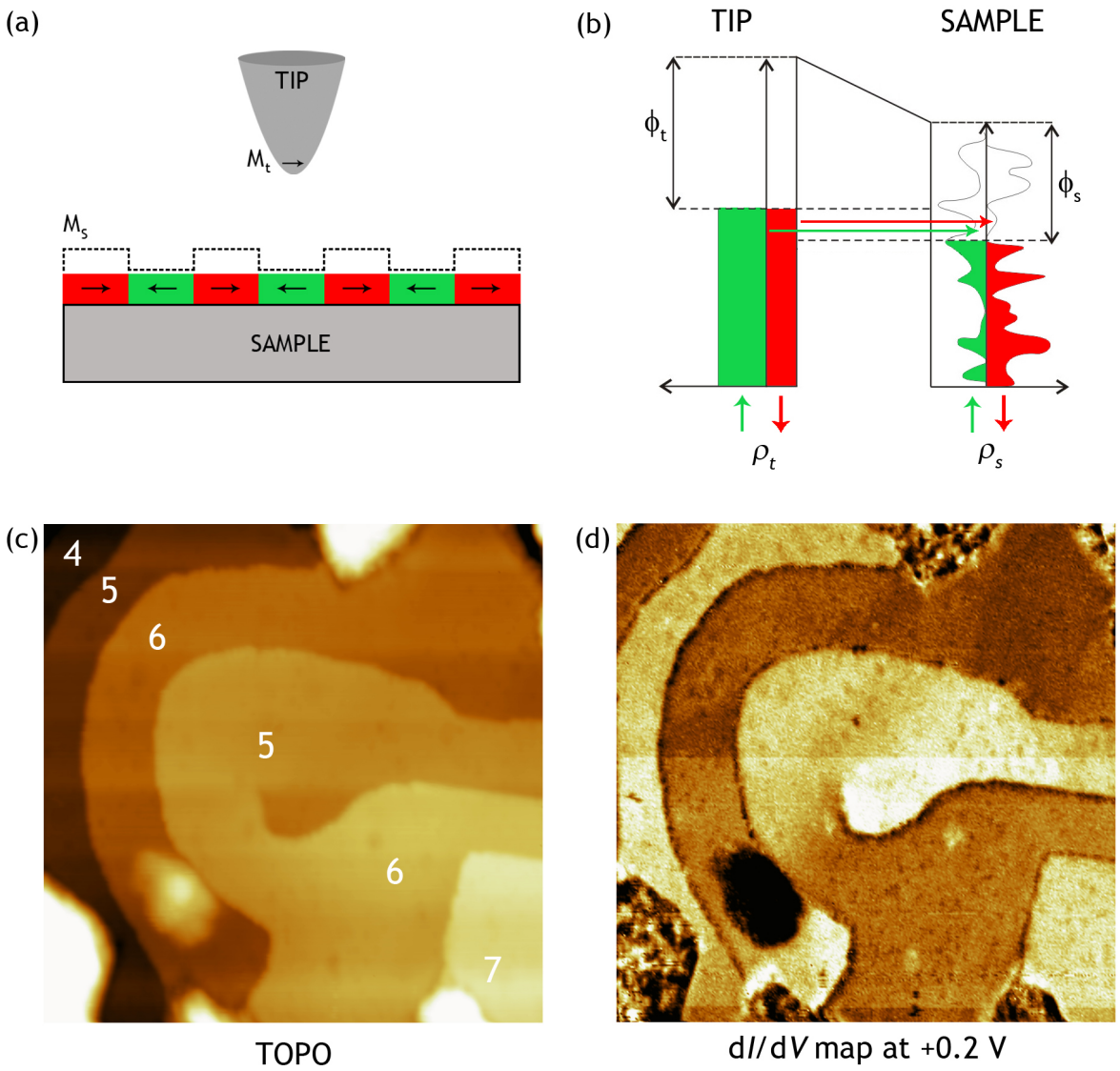

Figure 2.3: Spin polarized STS. (a) Schematic representation of the constant current mode for magnetic tip with in-plane magnetization scanning a magnetic surface with antiparallel domains. (b) Spin-dependent tunneling in a magnetic tunnel barrier. The majority and minority electrons of the tip tunnel into the empty majority and minority states in sample respectively. (c) An STM topographic image ($80 \times 80\,\mathrm{nm}^2$) of an Fe(001)-screw dislocation covered with 7 ML of Mn ($V_\mathrm{b} = -1.0\,\mathrm{V}$, $I_\mathrm{t} = 0.5\,\mathrm{nA}$). The numbers indicate the local thickness of the Mn film. (d) Spin polarized $\mathrm{d}I/\mathrm{d}V$ map at $V_b = +0.2\,\mathrm{V}$ measured simultaneously with the topography in (c). The maximum contrast in the $\mathrm{d}I/\mathrm{d}V$ map is as expected from the layered antiferromagnetic structure of the Mn thin films grown on Fe(001). The image has been measured at room temperature using a W tip coated with 20 ML of Fe.

Recently, the combination of state of the art SP-STS and spin resolved *ab initio* calculations has been used to show spin contrast through single magnetic molecules [8, 9] demonstrating the power of this technique to obtain magnetic information with atomic-scale resolution even in organic materials.

2.3 Instrumentation

Most of the experiments shown in this thesis have been performed in a home-built UHV system equipped with an Omicron Low Temperature Scanning Tunneling Microscope (LT-STM), located at Scanning Probe Microscopies and Surfaces Laboratory at the Madrid Institute of Advanced Research in Nanoscience (IMDEA-Nanoscience). This section will provide a description of the experimental set-up facilities.

2.3.1 General description

The design of the UHV system was done by Dr. Juan José Hinarejos, the details were described in Dr. Fabian Calleja's thesis [10] and Dr. Sara Barja's thesis [11]. Figure 2.4 shows a picture of the experimental set-up. The UHV system consists of a fast entry chamber, a tip preparation chamber, a sample preparation chamber and an STM chamber. All the chambers, except the STM chamber, were designed in-house and built in the workshop of Universidad Autónoma de Madrid. They are mounted on an aluminum frame supported by four pneumatic air dampers (Newport I-2000) to reduce the coupling of vibrations from the floor. Tips and samples are inserted (taken out) through the fast entry chamber without breaking the vacuum of the rest of the system. This small chamber is pumped by a membrane pump (PFEIFFER MVP 055-3) and a turbo molecular pump (PFEIFFER TMU 071P) and reach a pressure of 10^{-9} mbar. A magnetic transfer bar facilitates the transfer of tips and samples from the fast entry chamber to the tip and/or sample preparation chambers. In the following sections, a description of preparation and STM chambers will be presented.

2.3.2 Sample preparation chamber

The sample preparation chamber is equipped with the standard UHV preparation tools: a Quadrupole Mass Spectrometer (QMS) (PFEIFFER Prisma 80), an ion gun (SPECS IQE 11-A), gas inlets (Ar, O, N, ethylene), Low-energy Electron Diffraction (LEED), Auger Electron Spectroscopy (AES) and several evaporators. It is pumped by a turbo molecular pump (PFEIFFER TMU 512P) backed with a 2-stage piston pump (PFEIFFER XtraDry 150-2), and an ionic pump (Gamma Vacuum). After baking and degassing the system, the base pressure reached is 1×10^{-10} mbar. The partial pressures of residual gases are checked with the QMS. The pressure is measured by ionization gauge tubes, Bayard-Alpert type, with tungsten filaments capable of measuring pressures between 6×10^{-3} to 4×10^{-11} mbar.

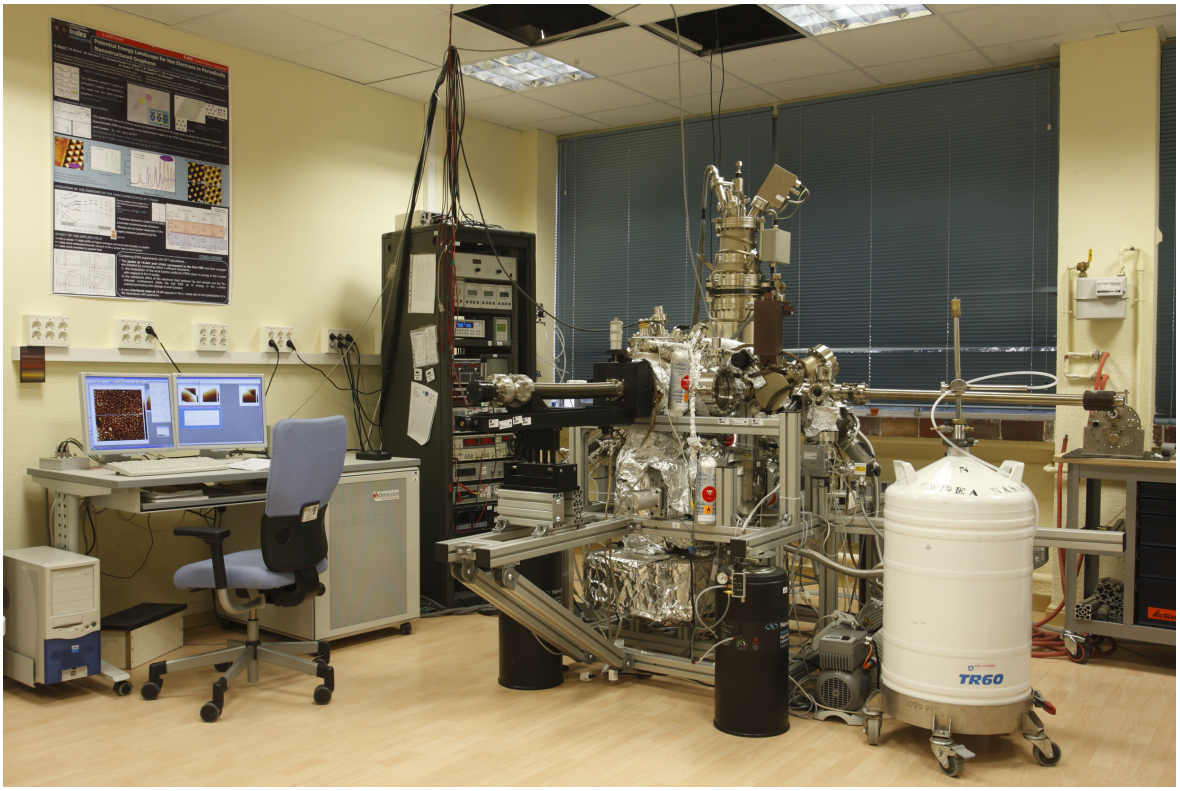

Figure 2.4: Picture of the UHV system.

The chamber also includes a manipulator to move the sample and the tip during the preparation steps and for transferring it into the STM or to the transfer bar. It can move the sample in the three spatial directions with a precision of 0.5 μm in x-y and 0.5 mm in z, and besides, it can rotated 360° around the z axis. The manipulator stage is compatible with Omicron tip and sample holders. The samples used in the work of this thesis were cylindrical single crystal metals (diameter=5 mm, width=0.2 mm), mounted on a Ta plate with spot-welded pieces of tantalum foil (see Fig. 2.5b).

Samples preparation consists of cycles of ion sputtering and annealing. Sputtering is performed by generating an Ar^+ ion beam by establishing a partial pressure of Ar in the chamber (4×10^{-6} mbar) through a leak-valve and then focusing it onto the sample by an ion sputtering gun. For an ion-beam energy of 1.5 keV, we obtain a ion current into the sample of 10 μA. After the sputtering, an annealing treatment is necessary to recover an atomically flat and well ordered surface. It is done by heating with electronic bombardment from a filament located in the manipulator stage at a distance of 0.3 mm below the sample holder. A few amps ($\sim$ 3 A) of current in the filament and a high voltage (800 V) applied between the filament and sample holder, lead to electron acceleration and heating of the sample. By this method, we can reach temperatures of 1500 K in 2-3 minutes, required for cleaning the metallic substrate and growth the graphene layers. Preliminary surface analysis methods

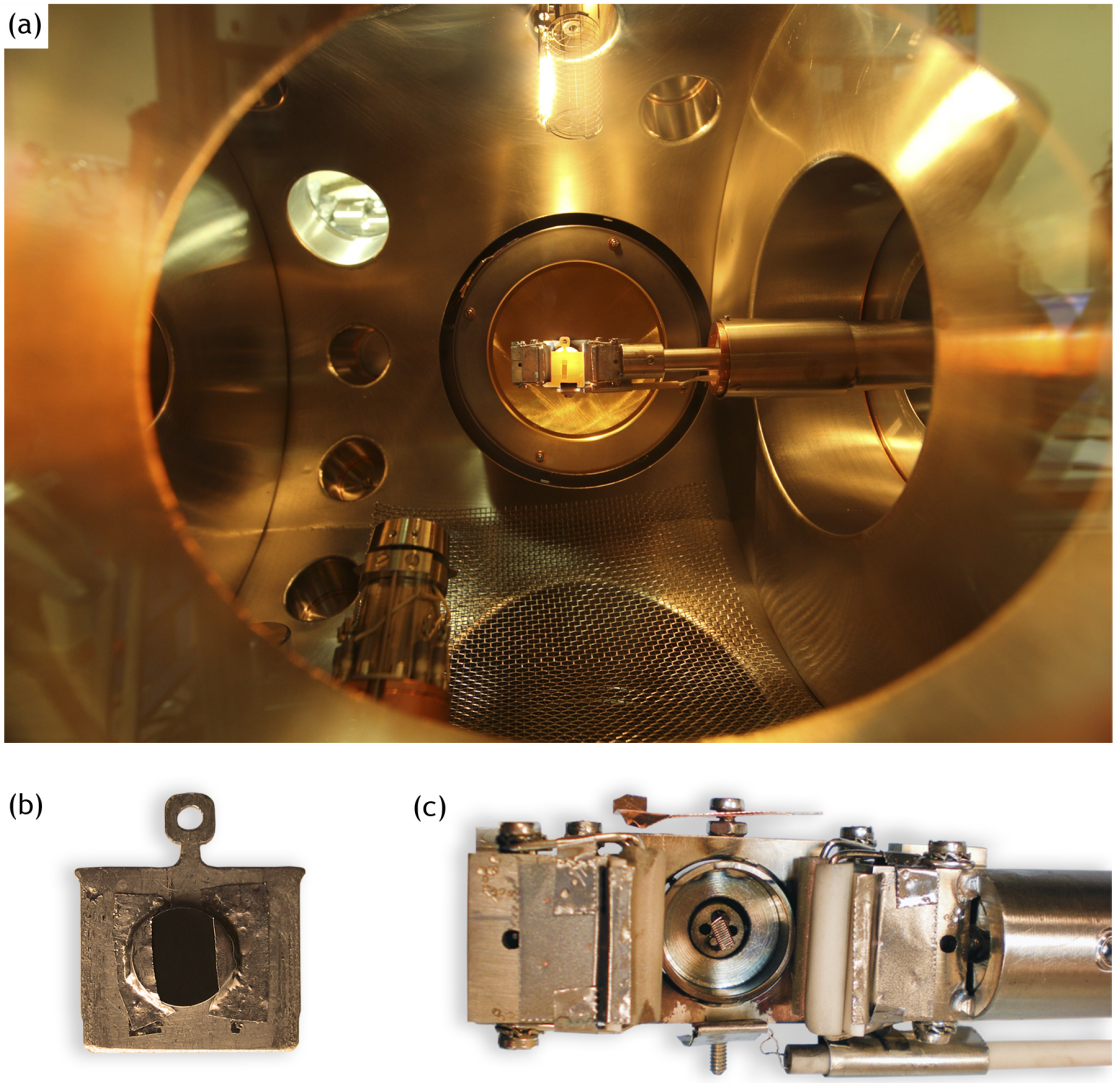

Figure 2.5: Sample preparation chamber. (a) Picture of the sample preparation chamber during the annealing process of a sample into the manipulator. (b) Picture of one of our sample holders. It consist in a metal single crystal of Ru(0001) with a circular shape (diameter=5 mm, width=0.2 mm) mounted on a Ta plate with spot-welded pieces of Ta foil. (c) Top-view of the manipulator end without a sample. In the center, the filament for heating through electronic bombardment is visible.

can be done before transferring the samples to the STM chamber. Omicron SPECTRA-LEED with AES capabilities is installed in the chamber and allows the determination of the surface structure and chemical composition after its preparation and before the LT-STM experiments.

The chamber is also equipped with an Omicron EFM 3T evaporator and a Kentax TCE-BCS 3 cell UHV evaporator. The Omicron evaporator allows higher temperatures and is designed for deposition of metals such as Fe, Co, Pb or Cu. The Kentax evaporator, the one mainly

used during this thesis, allows a precise temperature control with a limit of 800 K and is designed for molecular evaporation. This evaporator is separated from the main chamber by a gate valve and pumped down through the tip preparation chamber. This configuration allows the refilling or change of the molecules in the crucible without breaking the UHV of the main chamber. It includes 3 independent and separately controllable evaporation cells that allows co-evaporation of two material simultaneously. The molecular evaporation is done with the sample at room temperature and a distance about 10 cm. The evaporation temperature is kept constant (353 K for TCNQ and F_4-TCNQ) meanwhile the time is varied depending on the desired coverage. The coverage is calibrated using the STM.

2.3.3 Tip preparation chamber

The tip preparation chamber was designed to anneal the tip and coat it with different materials. It is located between the sample preparation chamber and the fast entry chamber and is independently pumped by a similar system as the sample preparation chamber, a turbo molecular pump (PFEIFEER TMU 261P) connected to a 2-stage piston pump (PFEIFFER XtraDry 150-2) and a pressure sensor Bayard-alpert type (Edwards D02999380).

Our tips are made by chemically etching, with 5 M KOH, a W polycrystalline wire (purity 99.99 %) with a diameter of 0.4 mm. Then, the tip is fixed to an omicron tip holder and introduced into the chamber on a tip carrier plate. The W tips generated by electrochemical etching are covered with a dense oxide layer and other contaminants. To remove them, an *in-situ* tip sputtering and an annealing treatment is necessary. For this purpose, a home-built system was implemented in the chamber. Tip annealing is achieved by forming a "bad contact" between the tip and a Ta foil (as shown in Fig. 2.6a) and passing a current through it. Since the most resistive point is the contact itself the heating is very localized, and this prevents damaging the tip carrier. In order to clean the tip apex, it is sputtered by Ar^+ with an energy of 2.5 keV during 30 minutes and subsequently heated. This treatment produces clean tips and sharp enough for a normal topographic imaging and STS experiments. However, for SP-STM experiments further tip preparation steps are required. Obtaining a tip suitable for SP-STM experiments with high spin polarization, nondestructive magnetic imaging and a high spatial resolution is a difficult task. The selection of the coating material and the thickness is fundamental to obtain stable tips with non-zero magnetic moment [6]. In this thesis, the tips were covered *in-situ* with approximately 20 ML of Fe sublimated from a Fe rod (99.9 % purity) heated by electron bombardment. The evaporation rate is 1 ML per minute. The shape of the tip before coating is decisive for the final magnetization anisotropy of the deposited magnetic layer. Fe films on W tip apex have an in-plane anisotropy. Therefore, sharp Fe-coated tips usually do not detect the sample's in-plane magnetic information. To prevent this, the Fe evaporation was performed just after the annealing treatment in order to get a blunt tip to promote the in-plane magnetization sensitivity, as shown in the schematic

representation in Fig. 2.6d. Special care must be taken with these tips during approaching the surface in order to avoid a possible tip crash.

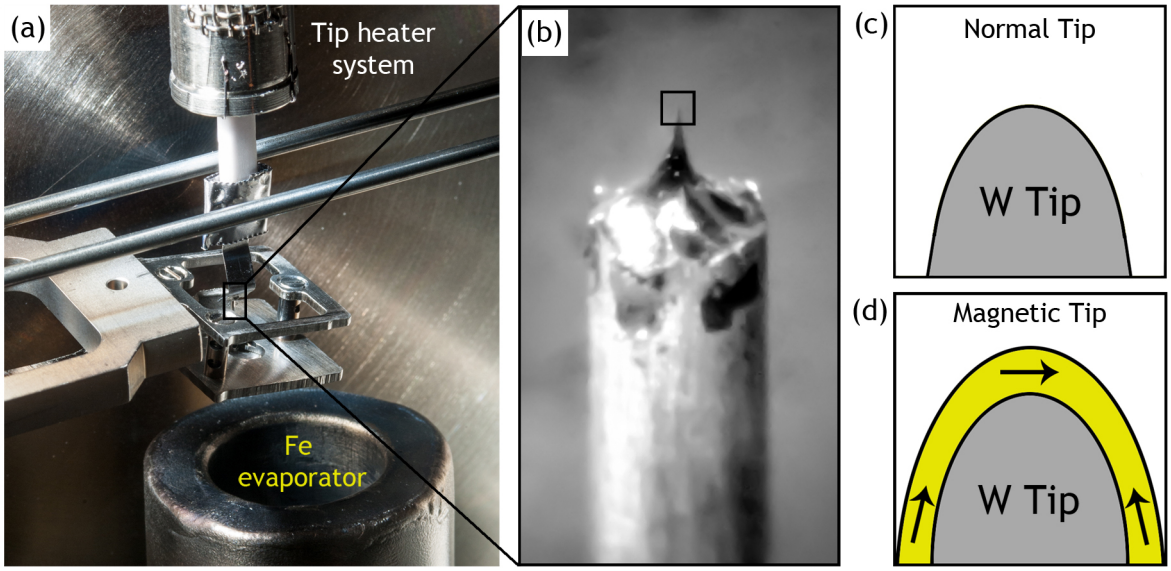

Figure 2.6: Tip preparation chamber. (a) Picture of the tip preparation chamber with the tip annealing system in action. (b) Zoom of the W tip and a sketches of (c) normal W tip after preparation procedures and (d) a magnetic tip where the magnetization distribution for a thin-film of Fe is represented.

2.3.4 Low Temperature STM chamber

The LT-STM chamber is connected to the sample preparation chamber and has its own pumping system. A turbo molecular pump (PFEIFFER TMU 261P) backed by a 2-stage piston pump (PFEIFFER XtraDry 150-2) and an ionic pump (Gamma Vacuum). The base pressure reached is 1×10^{-10} mbar although the ionization gauge tubes, Bayard-Alpert type (Edwards D02999380), record pressures below 1×10^{-11} mbar when the temperature is stabilized at 4.6 K.

A sketch of the chamber is shown in Fig. 2.7a. The LT-STM cryostat is based on a Liquid Helium (LHe) bath cryostat and a surrounding Liquid Nitrogen (LN_2) bath, fully housed in the UHV chamber. The LT-STM stage is located just below the cryostats and equipped with an ultimate vibration isolation system that employs a very efficient damping system based on the combination of spring suspension and eddy current damping, see Fig.2.7b. In combination with the careful design of the UHV chamber and the supporting frame, the stability is in the picometer range. The stage can be on three different positions thanks to a lifting mechanism. In the cool position, the stage is in direct thermal and mechanical contact with the base of the LHe cryostat, guaranteeing fast cooling down. The tip and sample exchange should be done in the intermediate position where the STM is locked but with some

freedom of movement. Finally, the stage can be released into the eddy current damping system for the STM experiments. With this cryogenic and isolation system, the LT-STM can work at 4.6 K during 28 h. The LT-STM is equipped with a low noise preamplifier SPM PRE 4 able to work with currents between 1 pA and 330 nA with an excellent signal-to-noise ratio.

The tip and sample transfer from manipulator into the STM is done using a UHV wobble stick. Besides, samples and tips can be stored in a carousel located in the UHV chamber with 6 storage positions.

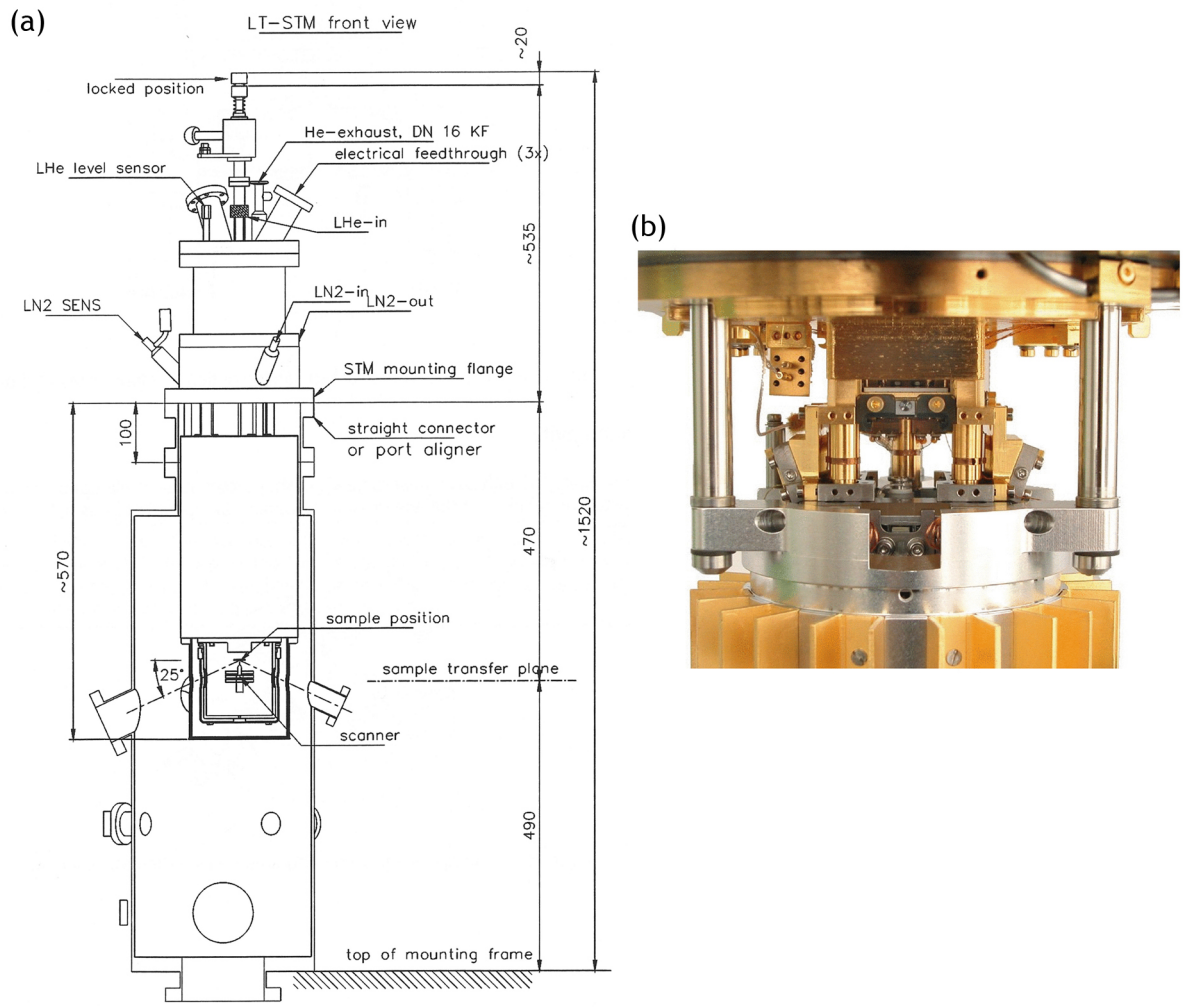

Figure 2.7: (a) Sketch of the LT-STM chamber. (b) Picture of the LT-STM stage from www.omicron.de.

3 Graphene on metallic substrates

This chapter gives an introduction to the growth of graphene on transition metals. After some remarks of the history of graphene on metallic surfaces, we present an overview of the most important studies on the particular cases of graphene/Ru(0001) and graphene/Ir(111). These two systems are completely different from the graphene-metal interaction point of view, graphene on Ru(0001) can be considered as a model of strong interaction and graphene on Ir(111) as a weak interaction system, while the difference in the lattice parameter between graphene and the metal is similar.

3.1 A brief history of graphene-metal interfaces

Graphene is one of the most promising materials nowadays. There are several routes to fabricate graphene, one of them is the growth of a graphene layer on metals which has been studied for quite some time in surface science [12–14]. The formation of graphene layers was firstly observed after high temperature annealing of single crystals like Pt(100) and Ru(0001) [15, 16]. The origin of this graphitic layers was the segregation of carbon impurities from the bulk of the metal. The first experiments explicitly designed to grow these carbon layers were carried out in 1960s [17] and they consisted in exposing several substrates to hydrocarbon gases as benzene, ethylene and methane. The result was the dehydrogenation of hydrocarbons and the formation of ultra-thin epitaxial films of graphite on transition metal surfaces.

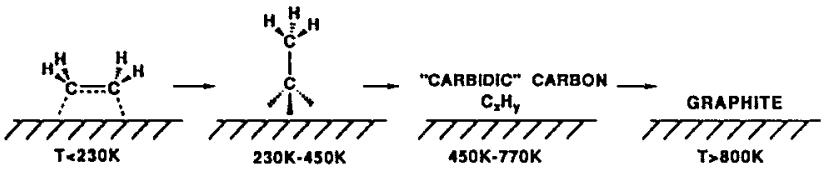

Figure 3.1: Schematic review of what was previously known about the adsorption and decomposition of ethylene on Pt(111). Image taken from [13].

During the '70s and '80s, there were a lot of studies focused on the influence of surface carbon on the catalytic activity of transition metals, the vibrational properties of the graphene films including the phonon dispersion relation and its modification by the intercalation of a

third material between the graphene overlayer and the metallic substrate, and the appearance of moiré superstructures. All these properties were investigated by means of High-Resolution Electron Energy-Loss Spectroscopy (HREELS) and Ultraviolet Photoelectron Spectroscopy (UPS) together with X-ray Photoelectron Spectroscopy (XPS), LEED and STM. For instance, the temperature dependence experiments of ethylene adsorption in Pt(111) by STM and LEED were able to clarify what is the critical temperature for the graphite layer formation (Fig. 3.1).

The experiments mentioned above paved the way for the new studies of the structural and electronic properties of graphene grown on metallic substrates [18–20] that appears after the work done by Geim, Novoselov and co-workers [21]. Graphene grown on metallic substrates is an efficient way to produce large graphene samples with a high structural quality which is a requisite for most practical applications. From a fundamental point of view graphene grown on metallic substrates is a very interesting system because, depending on the metallic substrate, the chemical interaction with the graphene layer is different and, accordingly, the graphene properties are modified.

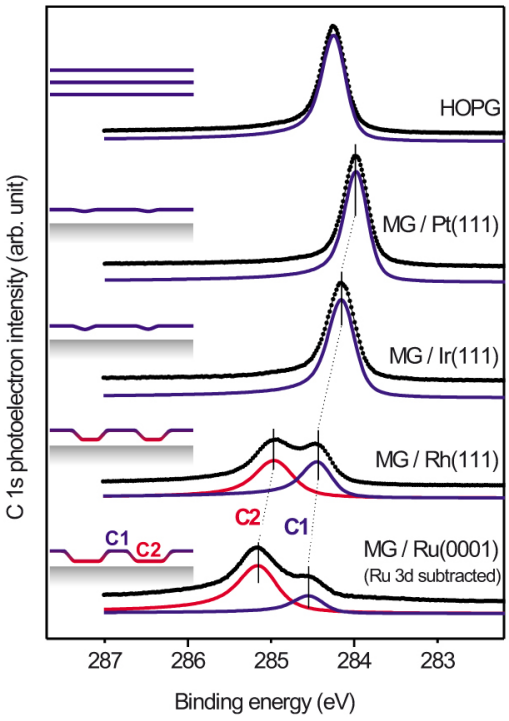

Figure 3.2: C 1s photoelectron spectra taken in normal emission from monolayer graphite adsorbed on several lattice mismatched transition metal surfaces. Photon energy is 400 eV. For graphene/Ru(0001) the Ru 3*d* signal is subtracted. The C 1*s* photoelectron spectrum from HOPG is shown for comparison. Schematics illustrate resulting graphene morphology. Figure taken from [22].

Photoelectron Spectroscopy (PES) and Near-Edge X-ray Adsorption Fine Structure (NEXAFS) experiments on graphene grown on the series Pt(111)-Ir(111)-Rh(111)-Ru(0001) surfaces, reveal that the carbon's chemical interactions are different along the series. The degree of interfacial orbital hybridization between graphene and metallic states is rising in the series due to the reduction of the *d* band occupancy of the metals [22]. Figure 3.2 shows the C 1*s* photoelectron spectra for graphene/metal systems compared with a spectrum measured on Highly Oriented Pyrolytic Graphite (HOPG). The C 1*s* photoelectron spectrum of HOPG presents only one component at 284.23 eV, the same occurs for graphene on Pt(111) and Ir(111) where the spectra show only one peak shifted in energy as is expected for a different carbon environments and a small charge transfer between graphene and the metallic substrate. On the other hand, for graphene/Rh(111) and graphene/Ru(0001), the C 1*s* line splits in two different components with energy separations of 0.53 and 0.60 eV, respectively. This splitting is attributed to the presence of two types of carbon atoms, one weakly bound to the metal atoms and another one strongly bound, as a consequence of the spatial corrugation of the graphene layer and the incommensurate registry between the graphene lattice and the metallic one. The spatial corrugation and the incommensurate registry are due to the difference in lattice parameters between graphene and the metallic substrate which leads to the formation of a moiré superstructure, the superposition of two lattices with different periodicities that generates a third periodicity that is known as moiré pattern. Hence, graphene grown on most metals presents a moiré pattern. The following sections will give a detailed description of two different systems, graphene/Ru(0001) and graphene/Ir(111).

3.2 Graphene on Ru(0001)

The graphene/Ru(0001) system has been investigated by STM [19, 23–25], LEED [26] , XPS [22], X-ray Diffraction (XRD) [27, 28], Photoemission of Adsorbed Xe (PAX) [29], Helium Atom Scattering (HAS) [30] and DFT [31–33]. In this section, we will describe how we grew graphene on Ru(0001) and the fundamental geometric and electronic properties of the system.

3.2.1 Graphene preparation on Ru(0001)

The substrate is a single crystal of Ru exposing the (0001) surface, which was cleaned in UHV by ion sputtering and annealing to 1400 K. The ion sputtering was made by Ar^+ ions ($E = 1.5\,kV$ and $P = 2 \times 10^{-6}$ mbar) in normal incidence to the surface and the annealing by electron bombardment. Following this treatment, the ruthenium surface was exposed to an oxygen partial pressure of 6×10^{-7} mbar for 2 minutes (32 L) while the sample was held at 1150 K. The objective of this oxygen treatments is to remove carbon impurities segregated from the bulk. After this treatment the sample heating was switched off leaving the sample

to cool down under the oxygen partial pressure for 5 minutes. During this cooling process, an oxygen 2×2 superstructure forms on the Ru(0001) surface protecting it from further contamination [10]. Once the pressure in the chamber was recovered the sample was flashed at 1400 K to remove the oxygen from the surface leading an atomically clean and ordered Ru surface. The graphene samples are then grown by thermal decomposition of ethylene. The Ru crystal, kept at 1150 K in UHV, was exposed to a partial pressure of ethylene of 10×10^{-8} mbar for 10 minutes (48 L). The ethylene molecules reach the surface and dehydrogenate, the hydrogen atoms desorb and carbon atoms diffuse on the surface and form the graphene layer. As a result of this procedure, large domains of graphene are grown on the surface as shown in Fig. 3.3.

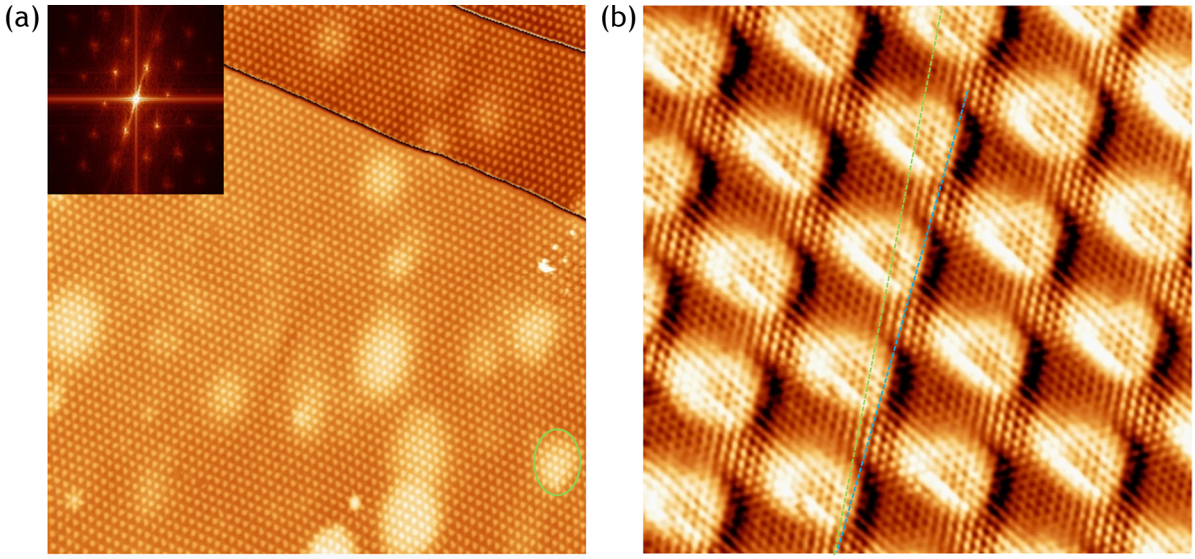

Figure 3.3: (a) A $200 \times 200\,\mathrm{nm}^2$ STM image of graphene on Ru(0001). The color scale has been adjusted independently on every terrace. The green circle encloses a subsurface argon bubble in the Ru(0001) substrate. The inset shows the FFT of the image showing the existence of a single hexagon and well-defined spots, a clear indication of long-range order on the moiré superstructure. (b) Atomically resolved STM image ($13 \times 13\,\mathrm{nm}^2$) of the complete graphene monolayer grown on Ru(0001) recorded at 4.6 K in an area free of defects ($V_b = -1\,\mathrm{mV}$, $I_t = 1\,\mathrm{nA}$). The green dotted line in the topographic image follows the high-symmetry direction of the C atomic rows in the graphene layer. The blue dotted line shows the direction of the moiré superstructure. Images taken from [30].

3.2.2 Characterization of graphene/Ru(0001)

As it was previously discussed, the difference in lattice parameters between graphene (0.246 nm) and ruthenium (0.271 nm) causes the appearance of a moiré pattern, resulting in the formation of a periodic bright protrusions separated by 2.93 ± 0.08 nm. Figure 3.3a shows an STM image of a single domain with a lateral size of 200 nm. All the bumps in the terraces

are aligned as shown by the hexagonal pattern in the two-dimensional (2D) Fast Fourier Transform (FFT) of the image shown in the inset. The only defects present in the image are bubbles of argon (green circle) buried in the Ru substrate during ion bombardment of the crystal [34, 35] that appear as cloudy regions. In the atomically resolved images recorded on these highly perfect graphene overlayers (Fig. 3.3b), we can notice a rotation between the moiré superstructure and the graphene lattice. The green dotted line indicates the high symmetry $[11\bar{2}0]$ direction of the carbon lattice and the blue dotted line the corresponding high symmetry direction of the hexagonal moiré pattern. They are clearly rotated with respect to each other by $(4.5 \pm 0.5)^\circ$. As discussed by N'Diaye *et al.* [18], the moiré pattern magnifies the rotation between the atomic lattices and allows us to determine small rotation angles between the atomic lattices from STM images. If $\varphi_{gr,Ru}$ is the angle between the graphene atomic lattice and the ruthenium one, and $\varphi_{\text{gr,moiré}}$ the angle between the graphene atomic lattice and the moiré, considering the difference between lattice parameters and assuming no distortion in the atomic lattice parameter for graphene and ruthenium, it is possible to find the following relation:

$$\varphi_{\text{gr,moiré}} = 9.96\, \varphi_{\text{gr,Ru}}\,. \tag{3.1}$$

Therefore, the carbon atomic direction $[11\bar{2}0]$ is rotated by 0.5° respect to the ruthenium direction $[\bar{1}010]$. This misalignment might be the explanation for the contradiction between the periodicity $C(25 \times 25)/Ru(23 \times 23)$ [27] obtained with XRD by measuring the deformation of the last ruthenium layers and the moiré periodicity $C(11 \times 11)/Ru(10 \times 10)$ obtained from the STM images [19]. However, all the important features of this surface are present in the $C(11 \times 11)/Ru(10 \times 10)$ unit cell. Figure 3.4 shows a scheme of such unit cell, the color code indicates the relative height of the carbon atoms. Depending on the registry of the graphene honeycomb ring with respect to the ruthenium atoms, we can distinguish four areas: *atop*, *fcc*, *hcp* and bridge (area between the *fcc* and *hcp* regions). In the *atop* areas no carbon atoms are placed on top of the Ru atoms contrary to the *fcc* and *hcp* areas where carbon atoms from one of the triangular sublattices of graphene are placed just above a Ru atom. The carbon atoms located on top of Ru atoms are chemically bonded and appear dark in the atomic resolution STM images, whereas the non-interacting atoms appear bright (Fig. 3.4) [36]. This effect allows us to distinguish between these two areas. In the rest of the thesis, *hcp* and *fcc* regions will be depicted in blue and red triangles respectively.

As can be seen in Fig. 3.4, there is a spatial modulation in the interaction between the atoms of carbon and Ru, going from no interaction in the high areas to strong interaction in the low ones [22]. This spatially modulated chemical interaction, in turn, modulates the electronic structure of graphene. Figure 3.5 shows spatially resolved $\mathrm{d}I/\mathrm{d}V$ tunneling spectra and maps close to the Fermi level measured at 300 K by A.L. Vázquez de Parga *et al.* [23]. The experiments are compared with model calculations for an isolated graphene layer in which

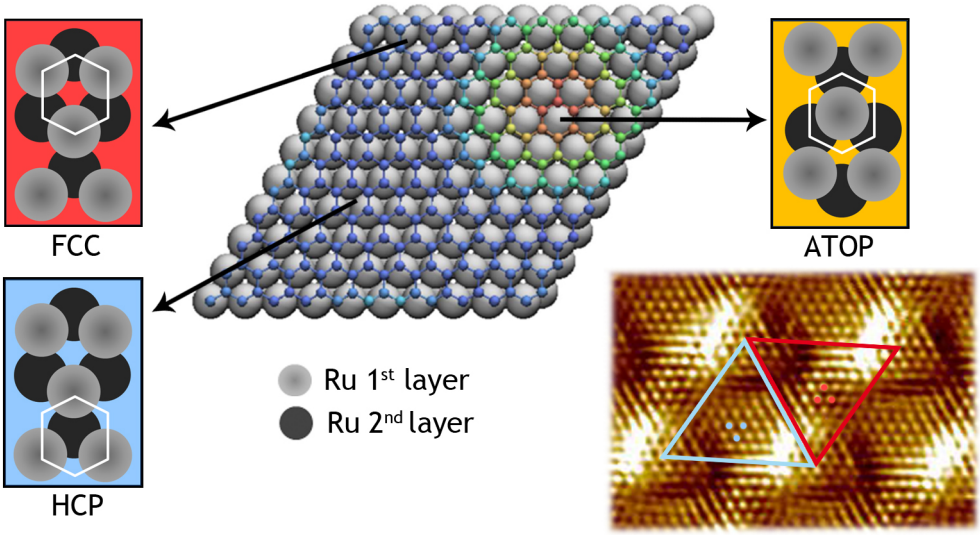

Figure 3.4: Calculated ground state geometry of graphene/Ru(0001) with $C(11 \times 11)/Ru(10 \times 10)$ periodicity. C atoms of the graphene monolayer are printed in different colors depending on their relative height, while Ru atoms are printed in grey. Four different regions can be distinguish depending on the position of the carbon atom ring with respect to the second ruthenium layer: *atop*, *hcp*, *fcc* and bridge (area between the *fcc* and *hcp* regions). A STM image with atomic resolution ($8 \times 5\,\mathrm{nm}^2$, $V_\mathrm{b} = -1\,\mathrm{mV}$, $I_\mathrm{t} = 1\,\mathrm{nA}$) is shown. The color dots indicate the positions of the carbon atoms visible that correspond to the nonbonding ones [33]. Blue and red triangles indicate the *hcp* and *fcc* regions, respectively.

the effect of the substrate has been considered to result in: (i) a shift of the Dirac point by $-0.3\,\mathrm{eV}$ due to doping; (ii) the introduction of a finite lifetime caused by hybridization of the orbitals with the band of the substrate; and (iii) a (11×11) periodic potential. The experimental $\mathrm{d}I/\mathrm{d}V$ spectrum, which is proportional to the LDOS, and the calculations show that the occupied LDOS close to the Fermi level is larger on the high regions of the moiré, while the empty LDOS is larger at the low regions of the graphene layer (Fig. 3.5b and 3.5c). This effect is extremely robust and indicates that the valence band is depleted in the low areas, while the conduction band is depleted at the high parts of the graphene layer. Thus, graphene/Ru(0001) surface presents inhomogeneneties in the charge distribution around the Fermi level producing an ordered array of electron pockets, as can be visualized in the real space in the $\mathrm{d}I/\mathrm{d}V$ maps of Fig. 3.5a.

The electronic effects are also behind the change in the apparent corrugation of the STM images with the bias voltage. Figure 3.6c shows STM topographic images recorded at representative sample biases measured at 4.6 K. A defect in the superstructure, encircled with blue, provides an absolute reference against possible drift between the images. The blue line highlights that the regions visualized as bumps at negative sample voltages (occupied

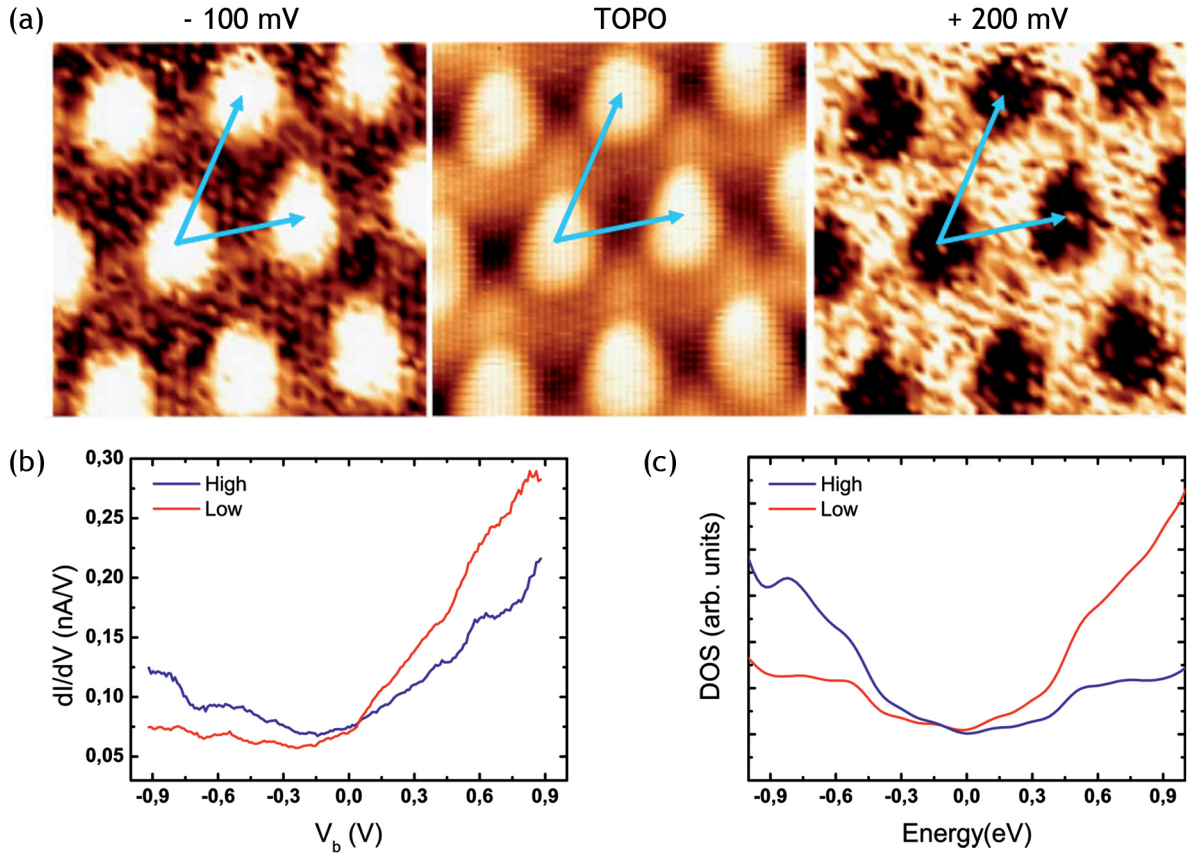

Figure 3.5: (a) The left and right images in the upper panel are maps of $\mathrm{d}I/\mathrm{d}V$ at $-100\,\mathrm{mV}$ and $+200\,\mathrm{mV}$ and reflects the spatial distribution of the LDOS below and above the Fermi level, respectively, for an extended graphene layer on Ru(0001). The central image shows the topographic image recorded simultaneously. (b) $\mathrm{d}I/\mathrm{d}V$ curves recorded at 300 K on the higher (blue curve) and lower (red curve) areas of the rippled graphene monolayer. (c) Calculations of the spatially resolved LDOS for an isolated, (11×11) periodically corrugated graphene layer. The spectra correspond to the high (blue curve) and low (red curve) regions of the rippled graphene layer. Figure adapted from [23].

states), are seen as depressions at $+2.8\,\mathrm{V}$ (empty states). When imaging occupied states, the apparent corrugation is rather constant ($\sim 1\,\text{Å}$), as expected because electrons at the Fermi level represent the larger contribution to the tunneling current, but the corrugation decreases continuously when injecting electrons in the empty states of graphene and becomes negative above $+2.6\,\mathrm{V}$. This behavior is fully reversible. A comparison between experimental results obtained for different experimental conditions and DFT calculations is shown in the plot Fig. 3.6b. The apparent corrugation calculated by including (excluding) van der Waals (vdW) corrections is in good (poor) agreement with that observed in STM experiments. The effect of vdW or dispersion forces plays a crucial role in this system and they are responsible for a reduction of 25% in the apparent corrugation of the moiré pattern. The value of the real corrugation and the origin of the high apparent corrugation in the STM images have been

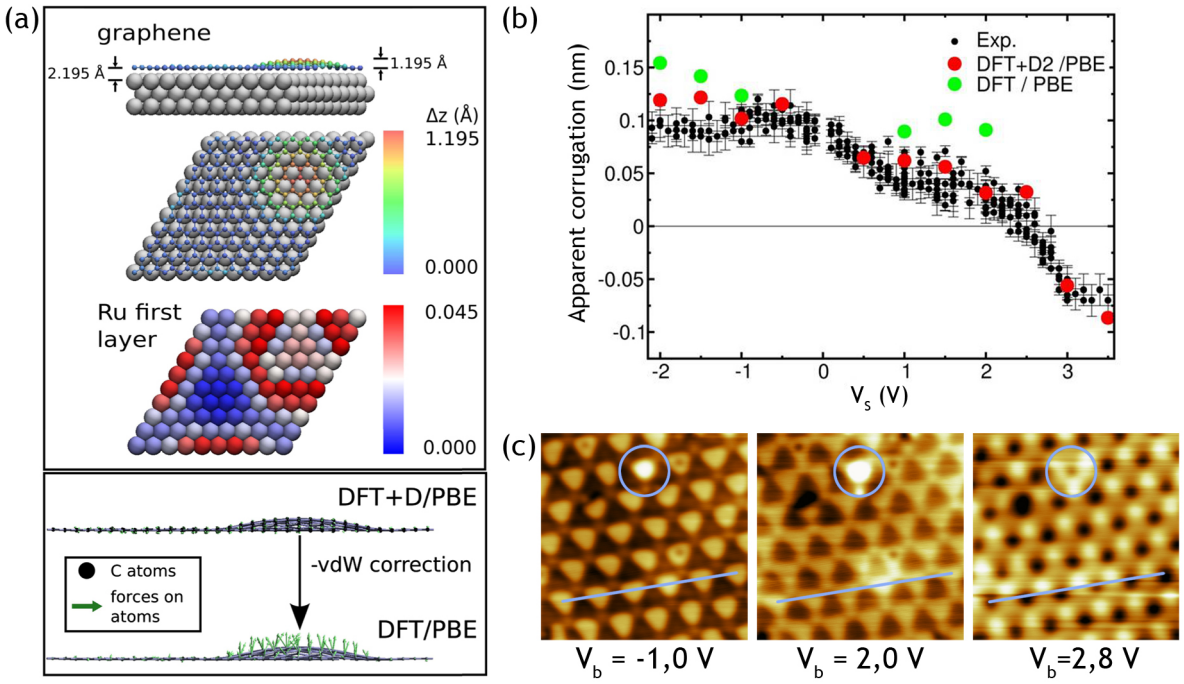

Figure 3.6: (a) Calculated ground state geometry of graphene/Ru(0001) and reconstruction of Ru topmost layer. Residual forces (arrows) acting on the C atoms of the graphene layer at the DFT + D2/PBE level (top) and when the correction due to dispersion forces is removed (bottom). (b) Variation of the apparent corrugation with bias voltage. Black dots: experimental results obtained with many different experimental conditions (tip, tunneling current, samples and temperature). Red dots: theoretical results with vdW correction. Green dots: idem without vdW corrections. (c) Topographic STM images at three selected sample bias voltages. [33, 37]

controversial. A summary is shown in Table 3.1. The calculated corrugation including vdW (1.195 Å) lies in between the values proposed in LEED and Surface X-ray Diffraction (SXRD) experiments and is higher than that inferred from HAS. The reason for the latter discrepancy is unknown. Interestingly, the role of the vdW interactions in the low areas of the moiré is weaker than in the high areas as a consequence of the rather strong covalent interaction between C and Ru atoms in this region. As proved by the minimum Ru-C distance which is only 0.105, 0.035, and 0.038 Å smaller than that obtained without vdW corrections in [31, 38] and the present work, respectively, for the same unit cell.

The modulation in the chemical bonding between graphene and ruthenium within the moiré unit cell modifies the surface dipole that has a direct influence on the surface potential. The modulation in the surface potential has been explored by means of PAX [29] and STS and first-principles calculations [37]. The PAX technique is based on the idea that the binding energy of the core or valence levels of physisorbed Xe on a surface depends on the value of the surface potential of its adsorption site [39]. Figure 3.7 shows the results of photoemission

Technique	Corrugation	Reference
STM	1.1 Å (−0.8 V) − 0.5 Å (+0.8 V)	[19, 23–25]
HAS	0.15 − 0.4Å	[30]
LEED	1.5 −Å	[26]
SXRD	0.82 − 1.5Å	[28]
DFT	1.19 − 1.7Å	[31, 33, 38]

Table 3.1: Geometric corrugations obtain for different techniques on graphene/Ru(0001).

from adsorbed xenon on graphene/Ru(0001) where two Xe $5p_{1/2}$ lines, separated by 240 meV, are present. This is a clear indication of a corrugated electrostatic surface potential.

The energy position of the Field Emission Resonances (FERs), which are detected by STM when applying voltages larger than the work function of the sample, presents a strong spatial variation of the order of 0.25 eV in the surface potential values depending on the position in the moiré pattern. Theoretical calculations not only reproduce this shift in energy but also identify the electronic state responsible of the contrast inversion in the STM images for bias voltages higher than +2.6 V. This peak appears in the $\mathrm{d}I/\mathrm{d}V$ spectra at +3.0 V only in the lower areas of the moiré. Its origin is traced back to the hybridization and confinement of a Ru(0001) surface resonance with the unoccupied density of states of graphene [11, 37]. In summary, this periodically rippled graphene on Ru(0001) behaves as a superlattice of shallow attractive potentials for electrons injected in the energy range of the first image states, with both quantum dot-like, spatially localized electronic states [11].

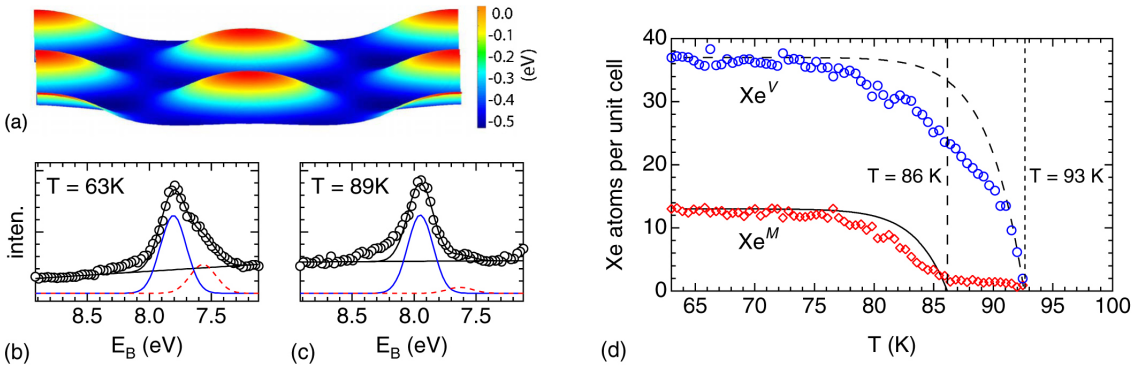

Figure 3.7: Xe adsorption on graphene/Ru(0001). (a) Calculated electrostatic potential map 3.8 Å above the outermost carbon atoms, (b) and (c) He I_α excited Xe $5p_{1/2}$ spectra for two Xe coverage during thermal desorption. At high coverage two spectral components may be distinguished. (d) Spectral weights of the two Xe species as a function of temperature. Blue open circles stand for the high binding energy and red open diamonds for the low binding energy component. Image taken from [29].

3.3 Graphene on Ir(111)

Unlike ruthenium, iridium presents a very low solubility of C in bulk. It means that the growth of graphene on Ir(111) can not be produced by impurity carbon segregation. Besides, the weak interaction between the Ir(111) surface and graphene give rise to the appearance of several moiré superstructures and characteristic defects when growing graphene on iridium making the temperature a crucial parameter in the graphene production. The different moiré superstructures, defects and electronic properties will be discussed hereafter.

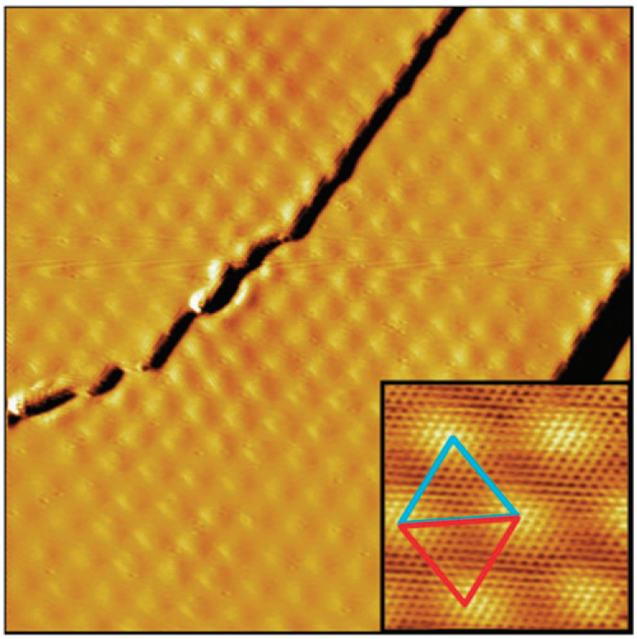

Figure 3.8: STM image ($32 \times 32\,\mathrm{nm}^2$, $V_b = 1\,\mathrm{V}$, $I_t = 15\,\mathrm{nA}$) of the (10×10) moiré pattern of graphene epitaxially grown on the Ir(111) surface. The image has been differentiated along the x-direction. The inset ($5 \times 5\,\mathrm{nm}^2$, $V_b = 2\,\mathrm{mV}$, $I_t = 100\,\mathrm{pA}$) shows an atomically resolved image of the moiré superstructure. Red and blue triangles mark the two halves of the unit cell with a different stacking sequence (*hc*p and *fcc*). [40]

3.3.1 Graphene preparation on Ir(111)

The Ir(111) surface was prepared by several cycles consisting of sputtering by a 1.5 keV Ar^+ ion beam and followed by flash annealing of the Ir crystal at 1500 K. This treatment is enough to obtain a clean Ir(111) surface. In this case, no oxygen exposure is required because, as it was previously mentioned, the Ir crystal does not contain carbon impurities. The graphene layers were grown by thermal decomposition of ethylene during 4 minutes at a partial pressure of $P = 10 \times 10^{-8}$ mbar (19.2 L) and substrate temperature above 1200 K. Then, we flashed the surface to 1400 K. The result is an almost complete graphene monolayer

where a number of rotation domains are found with the (10×10) moiré being the most common structure [11]. Figure 3.8 shows a long range STM image of graphene/Ir(111) surface grown by this procedure.

3.3.2 Characterization of graphene/Ir(111)

E. Loginova *et al.* [41] studied in detail the atomic structure of four different moiré superstructures of graphene on Ir(111) by means of Low-Energy Electron Microscopy (LEEM), LEED and STM. Previously, N'Diaye *et al.* [42, 43] reported the formation of well-ordered domains of a moiré superstructure with a periodicity of 9.32 Ir lattice constants. This structure corresponds to a perfect alignment, 0° rotation (R0) between the graphene layer and a chosen in-plane direction of the Ir(111) surface, and can be identified with C(10×10)/Ir(9×9) periodicity.

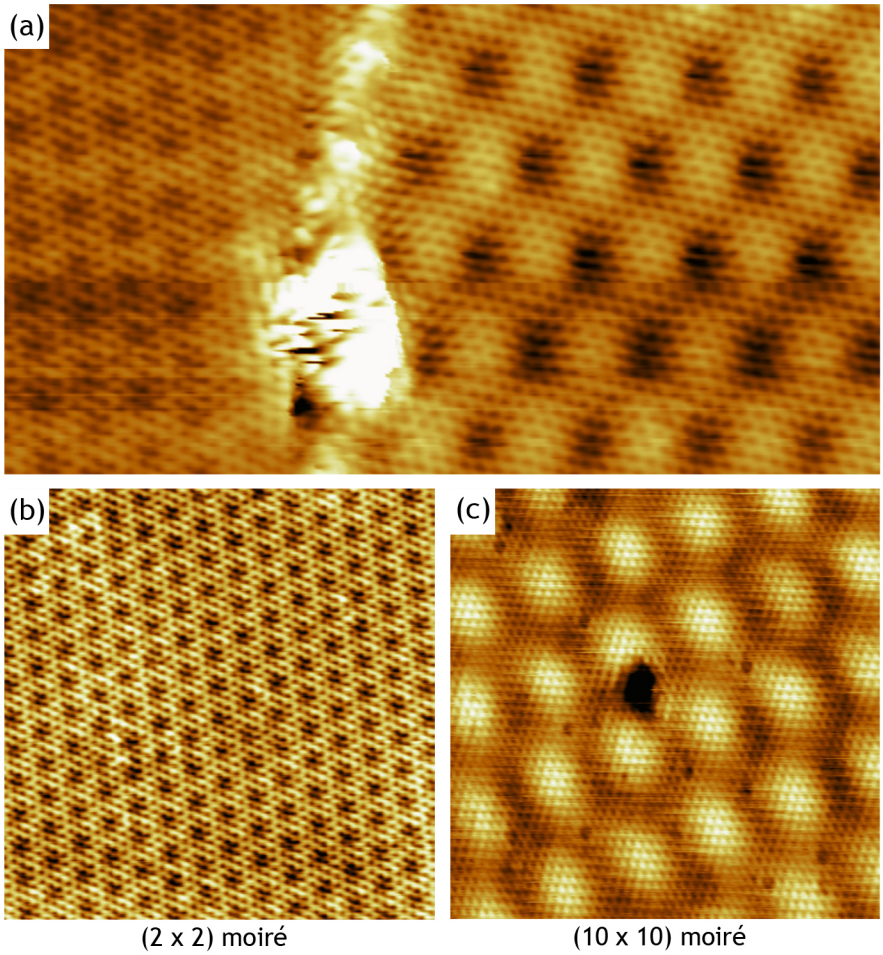

Figure 3.9: (a) Atomic resolution STM images of a monolayer of graphene/Ir(111) where a boundary between two rotational domains is visible ($13 \times 7\,\mathrm{nm}^2$, $V_\mathrm{b} = 10\,\mathrm{mV}$, $I_\mathrm{t} = 600\,\mathrm{pA}$). STM images ($11 \times 11\,\mathrm{nm}^2$) of (b) R30 domain ($V_\mathrm{b} = 10\,\mathrm{mV}$, $I_\mathrm{t} = 600\,\mathrm{pA}$) and (c) R0 domain ($V_\mathrm{b} = -1\,\mathrm{V}$, $I_\mathrm{t} = 50\,\mathrm{nA}$).

In our samples, we found long domains of the latter structure (Fig. 3.8) and small patches of another moiré superstructure which corresponds to a periodicity of C(2 × 2)/Ir(1 × 1) and a rotation of 30° (R30) between the graphene and Ir(111) high symmetry directions. In Fig. 3.9 both structures are visible. The (10 × 10) moiré (Fig. 3.9c) presents a small corrugation of 30 pm with a 2.45 nm periodicity and is visualized by STM as an hexagonal array of protrusions or holes depending on the tunneling parameters [42]. While, the (2 × 2) moiré (Fig. 3.9b) is far less corrugated, only 16 pm, and presents a lateral periodicity of 5 Å.

Henceforth, we will discuss in detail the (10 × 10) moiré because it is more abundant on our samples. This superstructure has been previously used as a template for metal cluster growth [18, 44]. The (10 × 10) moiré presents a preferential adsorption site that is related to a specific registry between the carbon and the iridium atoms. The registry is similar to the one for the graphene/Ru(0001) system as can be seen in Fig. 3.10. For instance, in the *atop* areas a honeycomb carbon ring is centered above an iridium atom. In the other configuration a carbon atom sits on top of an iridium atom, situating its three neighbors in threefold hollow sites on the Ir(111) surface. These areas correspond to the *hcp* and *fcc* regions, depending on the position of the honeycomb ring with respect to the second iridium layer.

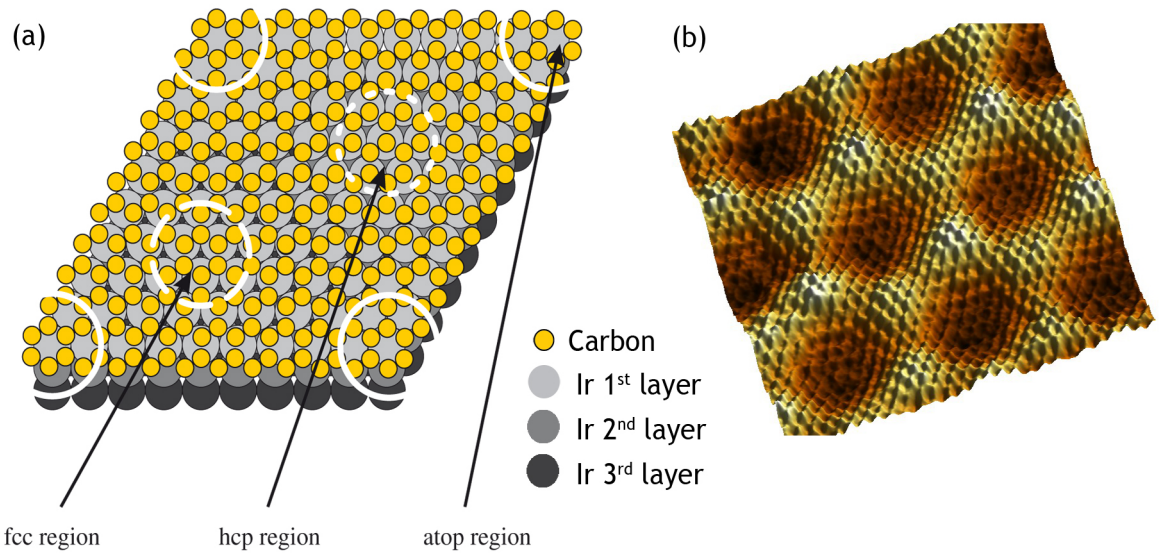

Figure 3.10: (a) Unit cell of the (10 × 10) superstructure of graphene/Ir(111) surface where the carbon atoms correspond to yellow balls and the iridium ones are the gray balls. The darker shades of gray represent the second and third layers of the iridium substrate. We can distinguish three different regions: *atop* (white arcs in the corners of the unit cell), *fcc* (dashed circle) and *hcp* (dotted circle). Image taken from [43]. (b) 7.4 × 6.5 nm^2 3D topographic image of graphene/Ir(111) showing the moiré modulation with the atomic corrugation superimpose (V_b = 0.3 V, I_t = 100 pA).

This huge unit cell was studied from a theoretical point of view firstly by Feibelman [45]. In his calculations nonlocal-correlation effects responsible for the vdW interactions were

not included. Nevertheless, the calculations were enough to explain the origin of the experimentally observed metal cluster pinning [18, 44] to the graphene moiré but they are questionable due to the tendency of exchange-correlation functionals (Local Density Approximation (LDA)) to overestimate the binding energies. Recently, using state of the art calculations, it has been shown that including the vdW interaction allows an accurate picture of graphene/Ir(111) system [46]. Contrary to the previous calculations, it has been demonstrated that the binding between graphene and iridium is not pure physisorption, but chemically modulated. In the *hcp* and *fcc* regions a small charge transfer occurs leading to a shift of the Dirac point of 0.2 eV above E_F in agreement with the experimental values [47]. In conclusion, graphene/Ir(111) system presents a small charge accumulation across the moiré unit cell between Ir substrate and graphene C atoms, signaling a weak bond formation.

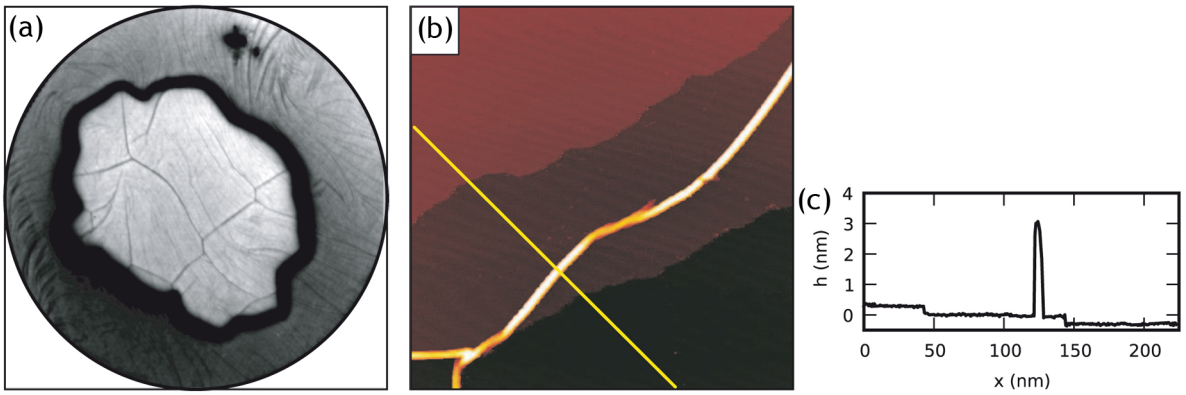

Figure 3.11: (a) LEEM image (field of view: 10 μm, electron energy: 2.8 eV) of a graphene flake on Ir(111) at room temperature. (b) STM topography ($240 \times 240\,nm^2$) of the same surface with a wrinkle. The bright line corresponds to the profile given in (c). Figure taken from [48].

An experimental evidence of the weak interaction between graphene and iridium, apart from the observation of several moiré structures, is the appearance of wrinkles during the growth process. Figure 3.11 shows a graphene/Ir(111) surface with several wrinkles measured by A. T N'Diaye *et al.* [44]. The left panel shows a LEEM image of a graphene flake on Ir(111) where branched lines defects are visible. The authors identify these structures with wrinkles of the graphene layer due to the fact that the wrinkles never appear in the bare Ir(111) surface. The middle panel corresponds to a STM image of the same surface where a long line defect is shown. In our samples, we too found this kind of defects. The origin of these wrinkles has been explained to be the difference in the thermal expansion coefficients of graphene and iridium [41, 48]. When graphene layer is formed at 1300 K is flat on the Ir(111) but when the system cools down, Ir contracts by 0.8 % while graphene does not change its lateral size, forming wrinkles with the extra material. Such defects have not been reported in strongly interacting systems like graphene/Ru(0001).

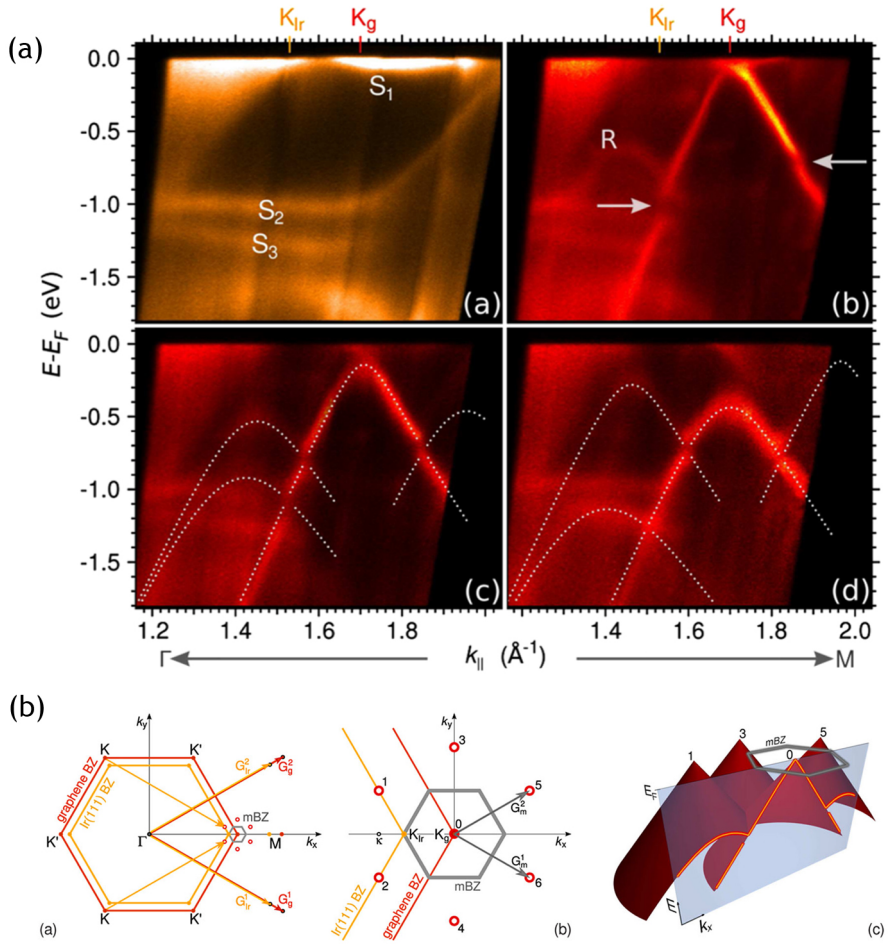

Figure 3.12: (a) ARPES spectrum of clean Ir(111) and of graphene cover with Ir(111) at the same and different azimuth angle. (b) Brillouin zone of the Ir(111) surface and graphene lattices. Open dots denote the vertices of Dirac cones replicated by moiré reciprocal vectors. Figure taken from [47].

Concerning the electronic structure, graphene on Ir(111) is close to freestanding graphene. A proof of this is that Dirac cone, graphene's most relevant intrinsic signature, is preserved [47]. Figure 3.12a shows the Angle-Resolved Photoemission Spectroscopy (ARPES) spectra of clean Ir(111) and graphene/Ir(111) along Γ-K-M, where the graphene Dirac cone is expected. The main features of graphene/Ir(111) spectra are the presence of a shifted Dirac cone due to the p-type doping and the opening of minigaps in the cone due to the moiré superperiodicity. The appearance of these minigaps can be understood with the Fig. 3.12b where the Brillouin zone of graphene and Ir(111) is drawn. The superperiodicity of the moiré lattice gives rise to the formation of replica cones and minigaps at the Bragg planes between the primary and replica cones. These features prove the long-range structural quality and uniformity of epitaxial graphene/Ir(111).

3.4 Conclusions

In this chapter, the growth of graphene on two metallic substrate, Ir(111) and Ru(0001), have been discussed. In both cases, the graphene was grown by chemical vapor decomposition of ethylene on the hot metallic surfaces. The results are long-range domains of highly-perfect, periodically rippled graphene. The different interaction of the graphene overlayer with the ruthenium and iridium leads to different electronic properties on the graphene layer.

In the case of graphene/Ru(0001), the graphene monolayer presents a hexagonal array of bumps with an average separation of 3 nm. This geometric modulation of the surface gives rise to the appearance of charge inhomogeneties on the moiré superstructure, observed with spatially resolved dI/dV maps and confirmed with a simple theoretical model. The apparent corrugation of the moiré pattern presents a strong variation with the bias voltage applied between the tip and the sample. STS experiments and DFT calculations suggest that the variation with bias voltage is due to a strong electronic effect. The value of the real geometric corrugation is still a subject of controversy. Finally, the exploration of the electrostatic potential energy landscape by PAX and STS indicates a modulation of the surface potential for graphene/Ru(0001).

For graphene/Ir(111) the graphene layer remains almost flat and its electronic structure is almost unaltered. The weak interaction leads to the formation of several rotational domains. In our samples, we found long areas of a 2.5 nm hexagonal periodicity that correspond to a (10×10) moiré and small patches of (2×2) moiré structure. In both cases, the superstructures are less corrugated than graphene/Ru(0001) and the apparent corrugation does not change with the bias voltage, highlighting the almost negligible interaction between graphene and iridium. Moreover, LEEM and STM experiments show the formation of wrinkles in the graphene layers during the cooling process. These defects are not observed in systems with a strong interaction between the graphene overlayer and the metal surface. They are related to the difference in the thermal contraction of the Ir substrate relative to the graphene layer during the growth process at high temperature. To conclude, a description of the electronic structure of the system was done based on the result of ARPES experiments. These measurements show that graphene/Ir(111) presents a shifted Dirac cone due to the slightly p-doping by the substrate comparable to the freestanding graphene.

4 Molecular self-assembly on epitaxial graphene

In this chapter, we study the adsorption of two electron acceptor molecules, TCNQ and F_4-TCNQ, on graphene grown on Ru(0001) and Ir(111). As it was discussed in the previous chapter, both surfaces exhibit a moiré pattern, but their electronic and surface potential modulation due to this geometric corrugation are completely different. Graphene grown on Ru(0001) presents a sizeable modulation in its electronic properties due to the spatially modulated interaction between the graphene overlayer and the Ru(0001) substrate. Contrary, the electronic properties of graphene on Ir(111) are uniform along the moiré unit cell. TCNQ and F_4-TCNQ are well known electron acceptor molecules. The main difference between them is the substitution of the four hydrogen atoms in the central ring of the TCNQ molecule (see Fig. 4.1a) for four fluorine atoms in the F_4-TCNQ. This substitution modifies the expected intermolecular interaction been attractive for TCNQ and repulsive for F_4-TCNQ. Considering than the molecular self-assembly on surfaces is a competition between molecule-molecule interaction and molecule-substrate interaction, the relative strength of these interactions on the molecular adsorption behavior is investigated for each molecule in both surfaces.

4.1 TCNQ

TCNQ (Fig. 4.1a) is formed by a central quinoid ring surrounded by four hydrogen atoms and two dicyanomethylene termination groups ($C(CN_2)$). Figure 4.1b and 4.1c show the frontier molecular orbital for TCNQ molecule in the gas-phase, Highest Occupied Molecular Orbital (HOMO) and Lowest Unoccupied Molecular Orbital (LUMO) respectively. The main difference between them is the node that appears in the middle of the molecule in the LUMO.

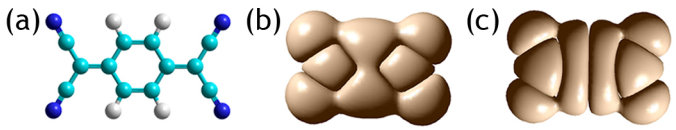

Figure 4.1: (a) Chemical structure of TCNQ molecule (dark blue = nitrogen atoms, gray = carbon atoms, white = hydrogen atoms). Frontier molecular orbital of TCNQ in gas-phase, (b) HOMO and (c) LUMO.

TCNQ is a well known electron acceptor molecule and has the capability of taking up to two electrons in gas-phase. The extra electrons are efficiently delocalizated in the central ring which loses the quinoid character increasing the aromaticity. This charge transfer process may come from a counterpart molecule developing Charge Transfer Complexes (CTC) [49], from a transition-metal ions in the metal coordination frameworks [50, 51] or from a surface-molecule interaction [52–54]. Regarding to the last case, previous STM experiments show that when it is deposited on a metallic surface, the electronic structure of TCNQ is strongly perturbed by the surface electrons. In the case of TCNQ on copper, due to the strong interaction between the cyano groups and the copper atoms, the molecule bends to allow the nitrogen to lie on top of surface copper atoms and it is not possible to take images of the spatial distribution of molecular orbitals [52, 53]. On the other hand, when the molecule is adsorbed on a weakly interacting substrate like Au(111), the charge transfer between gold and the molecule is small and the molecule lies flat on the surface [54].

4.1.1 TCNQ on graphene/Ru(0001)

Firstly, we studied the adsorption of TCNQ on the graphene/Ru(0001) surface at different coverages. The molecules are deposited on the surface at room temperature. At this temperature, the TCNQ molecules are free to move on the surface and it is necessary to cool down the sample at 4.6 K to be able to imaging individual molecules. In fact, the molecular freedom to diffuse on the graphene surface makes necessary the use of very low tunneling currents (below 100 pA) during the LT-STM measurements to avoid the interaction between the tip and the TCNQ molecules.

Figure 4.2 shows representative STM images recorded at 4.6 K after deposition of TCNQ molecules at room temperature. In Fig. 4.2b and 4.2c, we can easily identify the bumps of the moiré pattern superimposed with some bright protrusions that we associate with the molecules because, at this particular bias voltage, the intramolecular resolution resembles the LUMO shape of the molecule on the gas-phase (Fig. 4.1b). This is a clear indication of a weak molecule-substrate interaction. However, the substrate is playing a role in the molecular adsorption because all the molecules are placed in the low areas of the moiré pattern. As demonstrated earlier (Sec. 3.2), there is a difference in the value of the surface potential of the order of 0.25 eV between the high and low areas of the moiré. This surface potential corrugation forces the molecules to adsorb in the lower areas in the early stages of coverage as it was reported for phthalocyanines [55, 56], perylene tetracarboxylic diimide (PTCDI) and related derivatives [57], and perylene-3,4,9,10-tetracarboxylic dianhydride (PTCDA) [58] on similar surfaces. From our STM images, we can conclude that in the case of TCNQ on graphene/Ru(0001), there is no preferred adsorption site within the lower areas of the moiré unit cell. In agreement with this experimental observation, the DFT+D2 calculations performed by Daniele Stradi [36] under the supervision of Prof. Fernando Martín from the

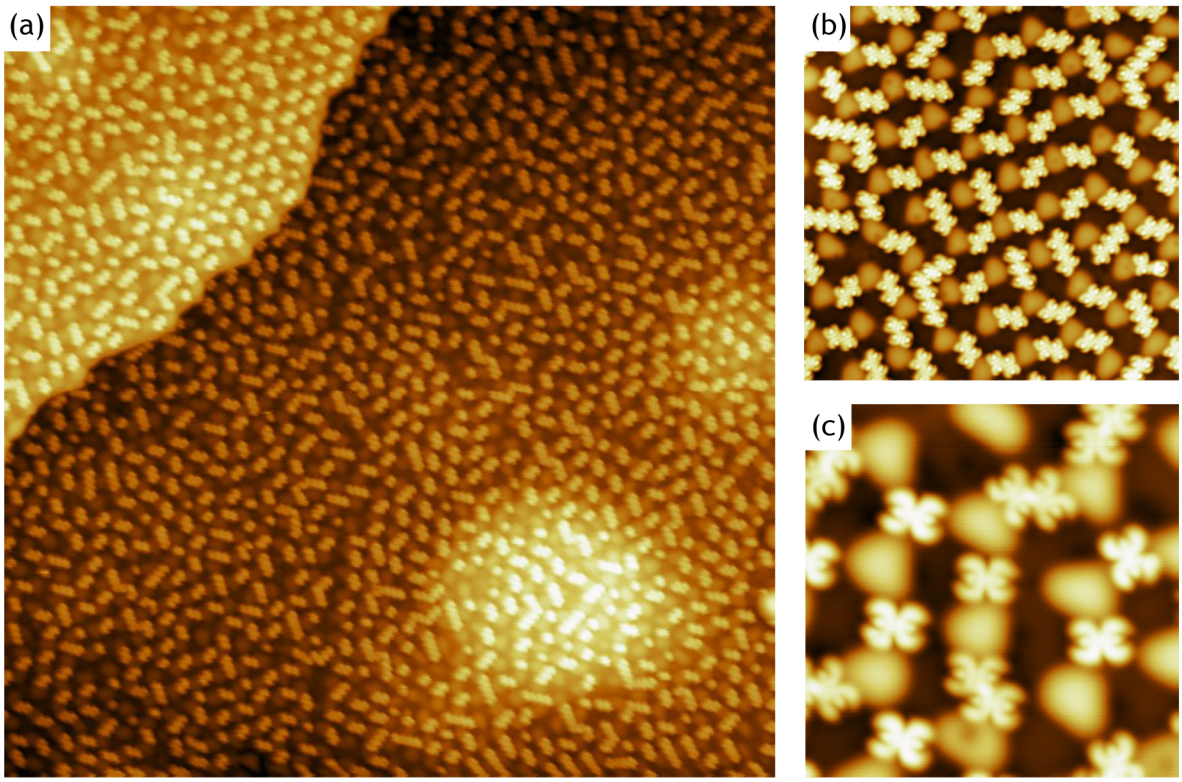

Figure 4.2: STM images of early stages coverage of TCNQ on graphene/Ru(0001). The corresponding sizes and set point parameters are: (a) $100 \times 100\,\mathrm{nm}^2$, $V_b = 1\,\mathrm{V}$ and $I_t = 50\,\mathrm{pA}$; (b) $20 \times 20\,\mathrm{nm}^2$, $V_b = -1\,\mathrm{V}$ and $I_t = 20\,\mathrm{pA}$ and (c) $10 \times 10\,\mathrm{nm}^2$, $V_b = -0.5\,\mathrm{V}$ and $I_t = 50\,\mathrm{pA}$

Chemistry Department of UAM, show a difference of less than 50 meV between the different adsorption sites in the lower area of the moiré.

Even at very low coverages, a close inspection of STM images measured at 4.6 K (see Fig. 4.2 as example) reveals the coexistence of isolated molecules with dimers, trimers and chains of up to 6 molecules. To study the nature of the bonding between the TCNQ molecules, the group of F. Martín has performed DFT+D2 calculations for the gas phase TCNQ dimer and for the adsorbed TCNQ dimer on graphene/Ru(0001). The calculations indicate that the dimer is stable in the gas phase with a formation energy of $E_{form} = -0.15\,\mathrm{eV/molecule}$ and is stabilized via a saturated C≡N$\cdots$H−C bond between a cyano group of one molecule and the hydrogen in the central ring of the other one. For the dimer adsorbed on the graphene/Ru(0001) surface, the adsorption energy per molecule is $10 - 20$ meV higher than for an isolated molecule [36]. This small difference in the adsorption energy for isolated molecules respect to the ones in the dimer is compatible with the coexistence of monomers and molecular chains when the TCNQ molecules are deposited on the surface at room temperature and then cool down to 4.6 K. In addition, the shape of the intermolecular region of the TCNQ dimer differs from that obtained as the sum of two TCNQ monomers on graphene/Ru(0001),

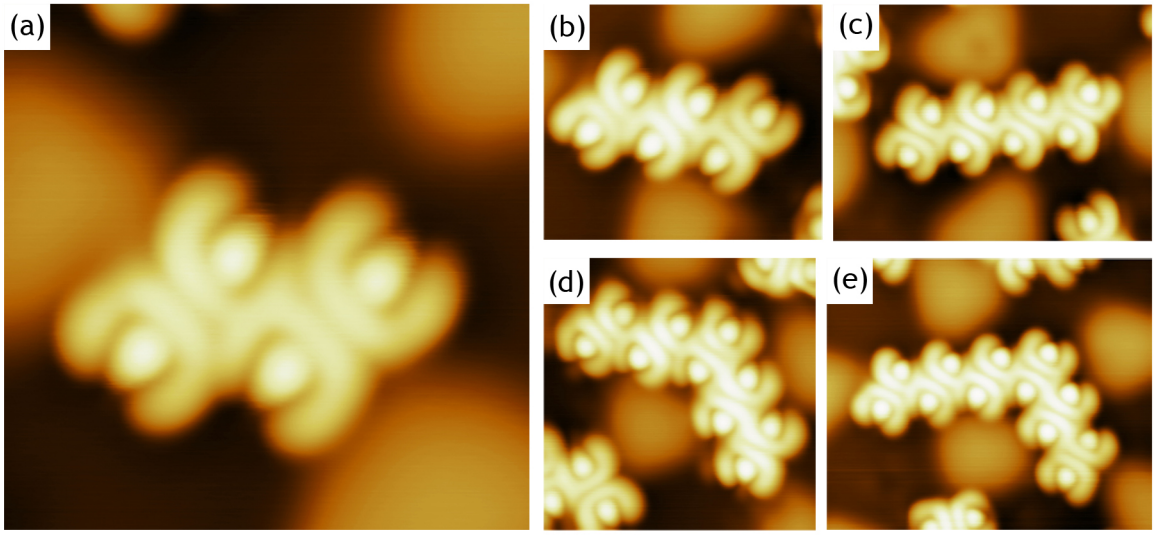

Figure 4.3: Chain formation of TCNQ on graphene/Ru(0001). All the images were acquired at 4.6 K with $V_b = -0.8$ V and $I_t = 40$ pA. The corresponding sizes are: (a) $3 \times 3\,nm^2$; (b) $3.8 \times 3.2\,nm^2$; (c) $5.4 \times 4\,nm^2$; (d) $4.5 \times 4.5\,nm^2$ and (e) $6 \times 5\,nm^2$.

thus suggesting some additional interaction between the two molecules. Experimentally, in the topographic image of the dimer (Fig. 4.3a), it can be clearly seen that the orbital of one molecule overlaps with the orbital of the other one. This interaction can be understood as the formation of a spatially extended intermolecular orbital. The incipient formation of this spatially extended orbital detected for dimers further develops as the coverage of TCNQ increases, as can be seen for the trimer and chains of molecules (Fig.4.3). A complete analysis of this interaction will be precisely described in the next chapter where the electronic properties and calculations of the system will be discussed.

Increasing the coverage, the molecular chains start to grow always avoiding the upper areas of the moiré, see Fig. 4.3d and 4.3e, giving rise to a zig-zag structure and forcing the rotation of the TCNQ molecules with respect to the moiré and allowing simultaneously the formation of the hydrogen bonds. At 1/3 ML coverage, these chains extend over hundred of nanometers and they are only interrupted by steps or defects (see Fig. 4.4). The formation of the chains is determined by molecule-molecule interaction but the distance between them is governed by the moiré pattern. Zooming in one domain (Fig. 4.5a), one can see that all the molecules along the chains point towards the same direction, as is expected for a directional hydrogen bond. Increasing slightly the coverage, the combined effect of the preferential adsorption in the lower areas of the moiré and the formation of hydrogen bonds allows us to produce a highly ordered porous molecular network with a periodicity of 3 nm, see Fig. 4.5b. Increasing more the deposition time, not more molecules fit in the lower areas and therefore, some of them are adsorbed on the upper areas of the moiré always maximizing the number

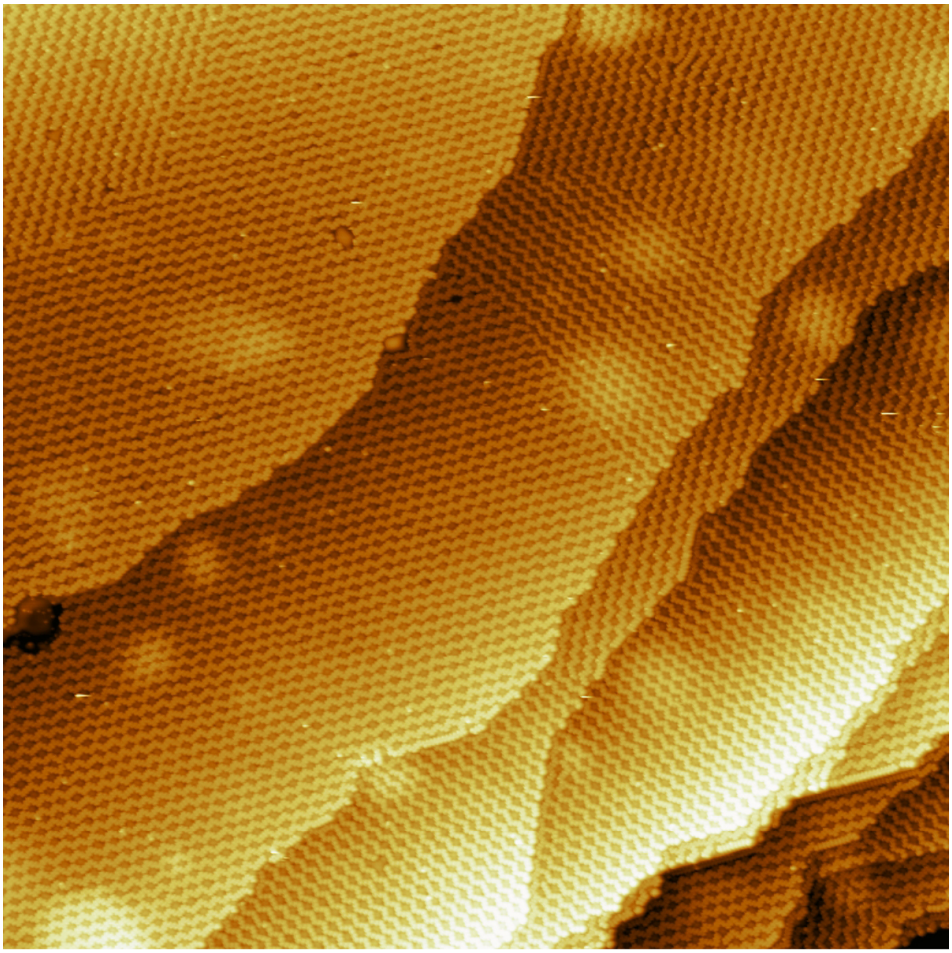

Figure 4.4: Large STM image ($175 \times 175\,\mathrm{nm}^2$, $V_b = -1\,\mathrm{V}$, $I_t = 10\,\mathrm{pA}$) taken at 77 K of intermediate coverage of TCNQ on graphene/Ru(0001).

of hydrogen bonds with the neighboring molecules (green circle on Fig. 4.5b). When the coverage is further increased, islands presenting a close packed structure appear coexisting with the porous network (Fig. 4.5c). At this stage, we can clearly see how the chain formation and the following close packed structure implies the rotation of the TCNQ molecules with respect to the high-symmetry directions of the moiré lattice. The (12×12) moiré unit cell vectors are drawn in Fig. 4.5c. As can be seen, the molecules in the molecular chains and in the close packed island are aligned along the long diagonal of the moiré unit cell (white arrow Fig. 4.5c). This rotation with respect to the high-symmetry directions of the moiré allows, at the beginning, the stabilization of the chain via hydrogen bonds avoiding at the same time the upper areas of the moiré and is finally translated to the monolayer.

The close packed molecular structure continues growing upon the completion of the TCNQ monolayer (Fig. 4.5d) and forming domains with lateral sizes of the order of hundreds of nanometers. The lateral size of the molecular domains is comparable with the domains

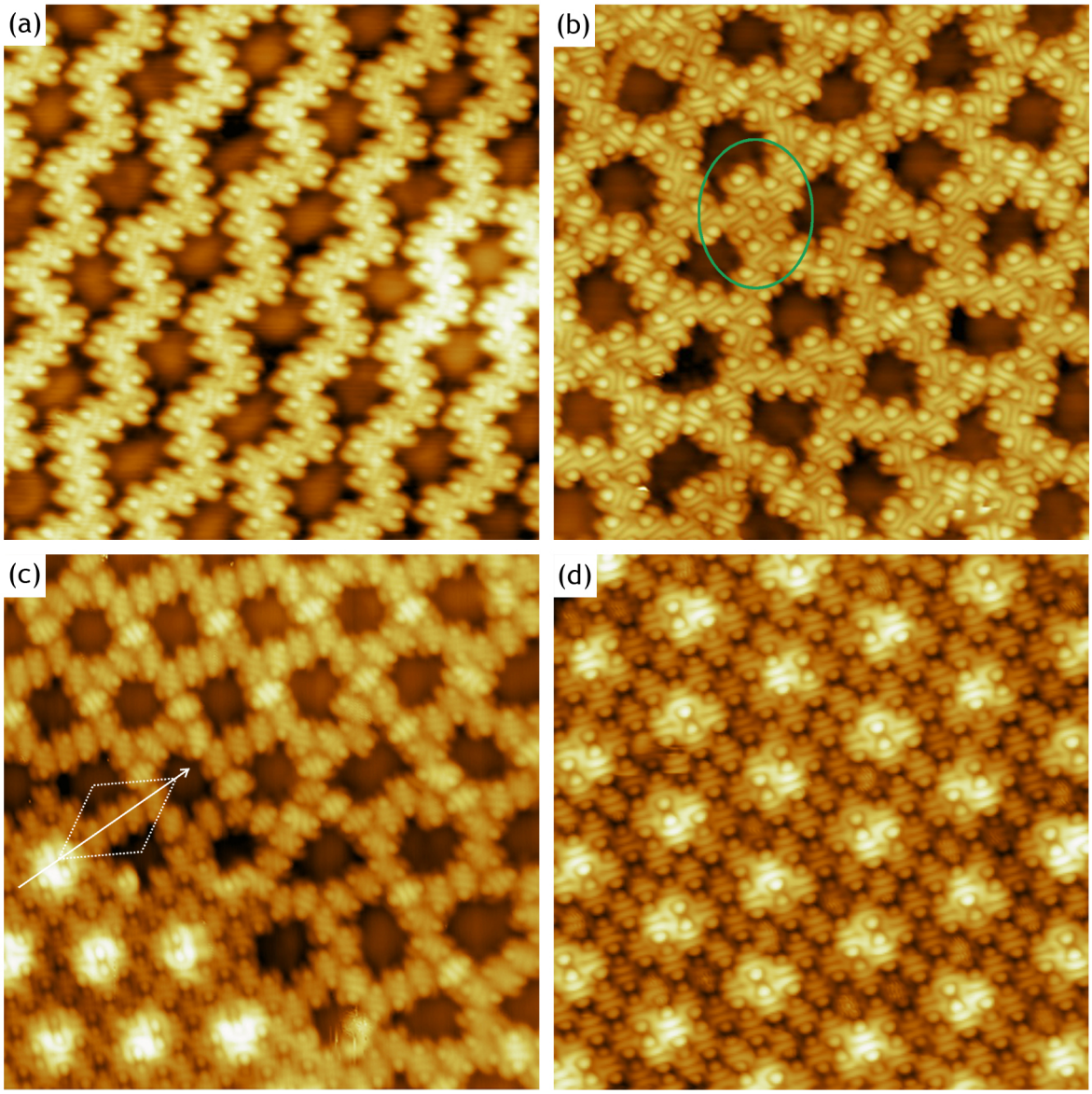

Figure 4.5: Coverage evolution of TCNQ on graphene/Ru(0001). (a) $15 \times 15\,\mathrm{nm}^2$, $V_b = -1\,\mathrm{V}$, $I_t = 20\,\mathrm{pA}$; (b) $15 \times 15\,\mathrm{nm}^2$, $V_b = -1\,\mathrm{V}$, $I_t = 50\,\mathrm{pA}$, (c) $15 \times 15\,\mathrm{nm}^2$, $V_b = 1\,\mathrm{V}$, $I_t = 50\,\mathrm{pA}$ and (d) $15 \times 15\,\mathrm{nm}^2$, $V_b = 2\,\mathrm{V}$, $I_t = 100\,\mathrm{pA}$.

size for graphene grown on Ru(0001) [30]. Figure 4.6 shows a series of images with different lateral size acquired on the same area where it is possible to observe how the presence of defects in graphene/Ru(0001) surface leads to the appearance of domains in the TCNQ layer. Figure 4.6b confirms that the domain boundary presents in the monolayer is pinned at the defect of the graphene which is not covered by TCNQ molecules. The relative orientation between domains can be determined in the zoom in of the domains boundary of the Fig. 4.6c. In this particular case, the relative angle between domains is 120°.

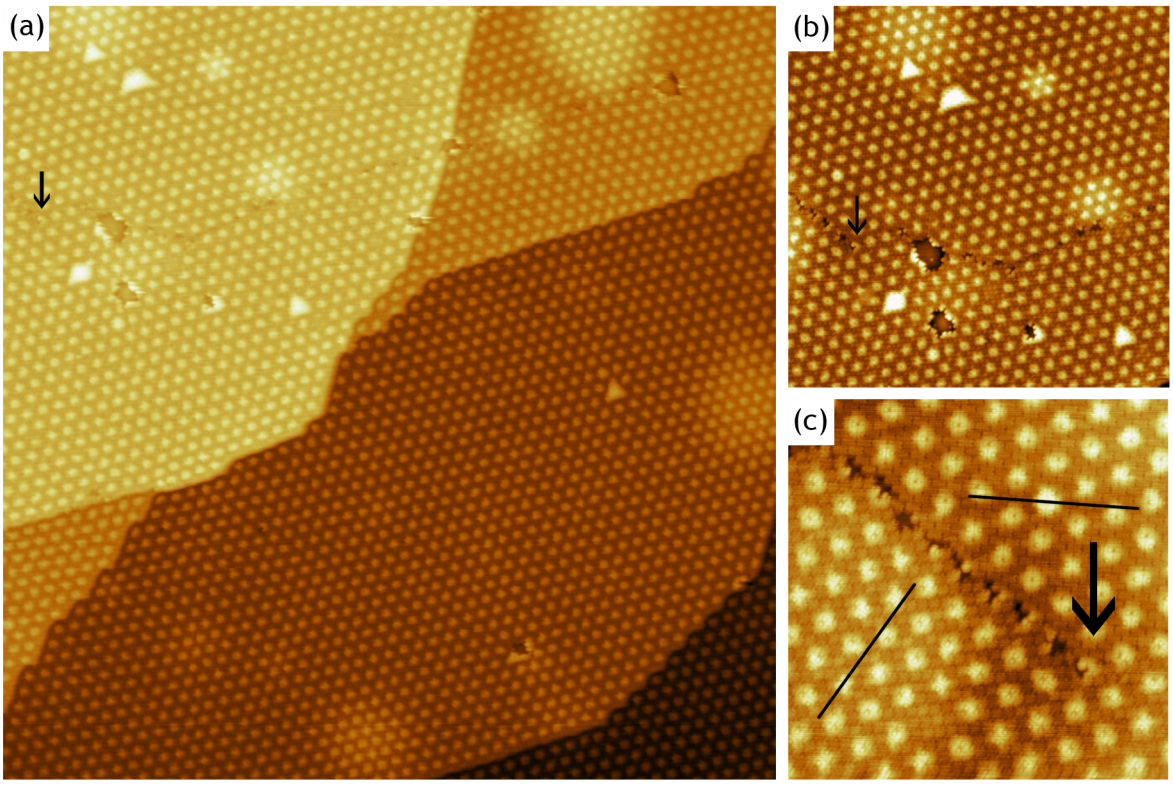

Figure 4.6: Series of STM images of a domain wall (a) $150 \times 150\,\mathrm{nm}^2$, (b) $70 \times 70\,\mathrm{nm}^2$ and (c) $28 \times 28\,\mathrm{nm}^2$, taken at $V_b = -1\,\mathrm{V}$ and $I_t = 50\,\mathrm{pA}$ in the same area. The arrows mark the same position in all images, the boundary between the domains with a relative orientation of 120 degrees.

As was discussed earlier, the analysis of the STM images reveals that the TCNQ molecules form an angle respect to the high-symmetry directions of the moiré. Figure 4.7a shows an atomically resolved image of the moiré pattern with the high-symmetry directions of the moiré marked by dotted black lines. The black arrow indicates the long diagonal of the (12×12) moiré unit cell. On the other hand, Fig. 4.7b shows a molecular resolved STM image after deposition of a TCNQ molecules. To determine the structure of the molecular layer relative to the substrate, the high-symmetry directions of the moiré (black dotted lines) and the molecular axis (yellow arrows) are drawn. As it can be seen, the long molecular axis forms 50° respect to the other molecular axis which in turn, coincides with the long diagonal of the moiré unit cell. This result is a consequence of the hierarchical way of growing that was discussed before, see Fig. 4.5c.

As we observed in the STM images, Fig. 4.6, and as it can be expected from the superimposition of an oblique lattice and an hexagonal one, a certain number of rotational domains appears. In order to obtain the molecular unit cell and the number of domains, we performed LEED experiments. These experiments were performed in the group of Prof. Roman Fasel at EMPA (Switzerland). In this laboratory, there is an UHV system that contains

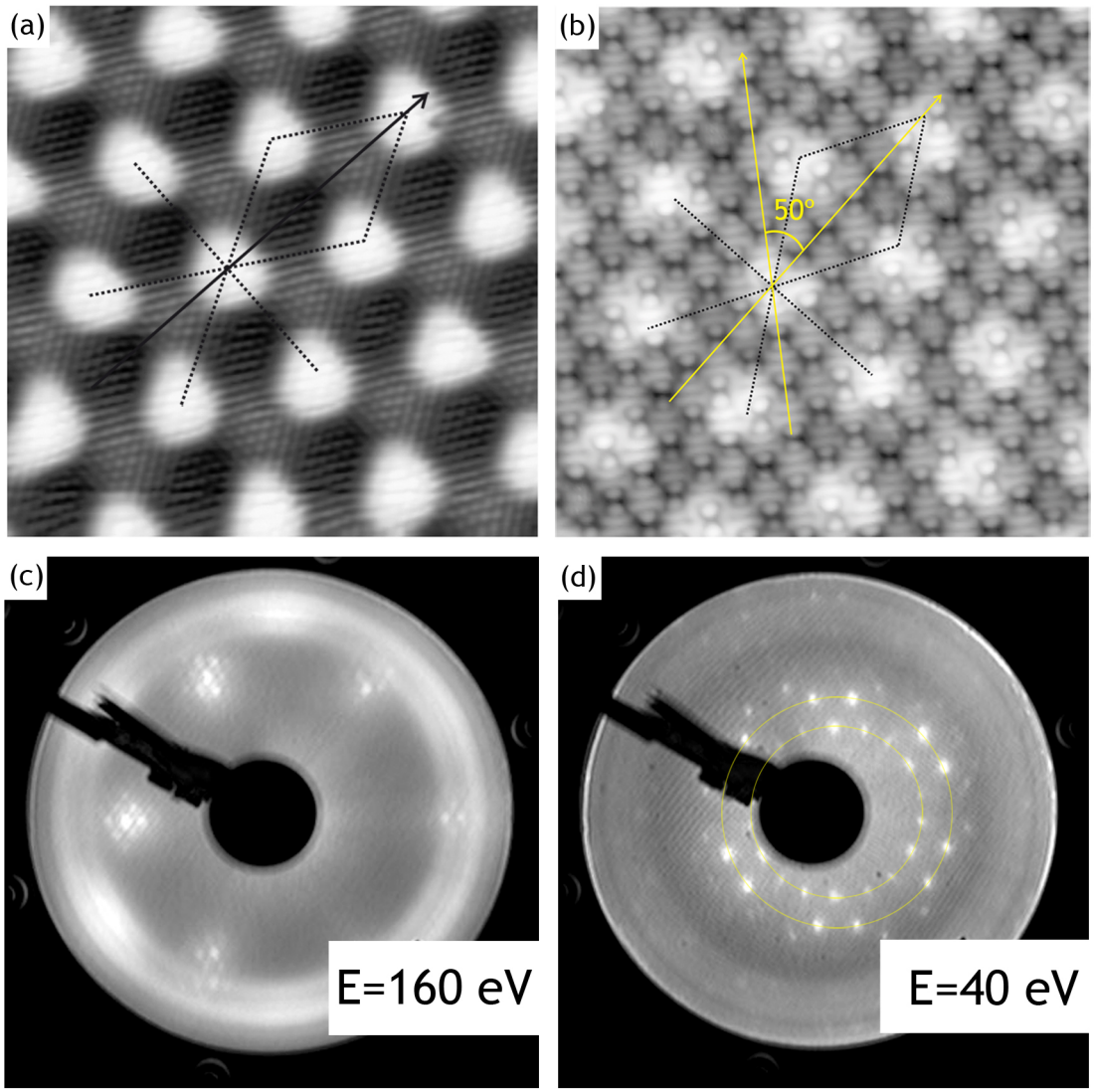

Figure 4.7: STM images taken at 4.6 K on (a) bare graphene/Ru(0001) ($12 \times 12\,\mathrm{nm}^2$, $V_b = -5\,\mathrm{mV}$, $I_t = 100\,\mathrm{pA}$) and (b) cover with a monolayer of TCNQ molecules ($12 \times 12\,\mathrm{nm}^2$, $V_b = 2\,\mathrm{V}$, $I_t = 50\,\mathrm{pA}$). The high-symmetry directions of the moiré are marked by black dotted lines and the black arrow indicates the long diagonal of the unit cell. The molecular axes marked by yellow arrows, are rotated 50° and not aligned with respected to the moiré lattice. LEED pattern from (c) bare graphene/Ru(0001) and (d) cover with TCNQ molecules, the spots are distributed around two concentric circumferences.

a Variable Temperature Scanning Tunneling Microscope (VT-STM) and an Omicron Micro-Channel Plate Low-Energy Electron Diffraction (MCP-LEED). The weak interaction between graphene and molecules requires the use of a MCP-LEED because the molecules do not resist the classical LEED beam currents. Figure 4.7c shows the typical LEED pattern taken with an electron energy of 160 eV for clean graphene/Ru(0001) and Fig. 4.7d is the corresponding pattern for a TCNQ monolayer on graphene/Ru(0001) at 40 eV. Figure 4.7d shows several

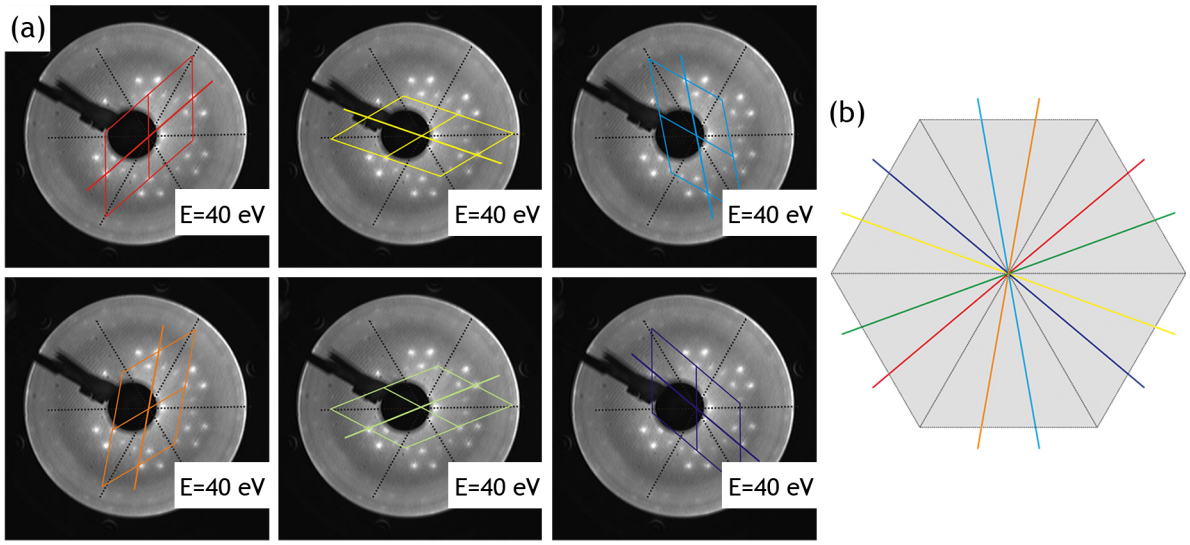

Figure 4.8: (a) Unit cell of the six domains drawn in LEED pattern of TNCQ/graphene/Ru(0001) at 40 eV. (b) Geometric representation of the relative angle between the high-symmetric directions of the moiré lattice and one molecular axis.

spots distributed around two concentric circumferences that determine the size of the two lattice vectors of the oblique molecular lattice. We attribute these spots to six different domains. Each domain is sketched in Fig. 4.8a with different colors and superimposed with the dotted black lines that represent the high-symmetry directions of the moiré. The domains are generated rotating clockwise the same oblique unit cell in such a way that one molecular lattice vector forms 20° with respect to a high-symmetry direction of the moiré lattice or the molecule long axis 50° with the long diagonal of the moiré unit cell. A summary of this construction is represented in Fig. 4.8b where the six possible configurations are sketched. This scenario is consistent with our experimental observations.

The quantitative analysis of the Fig. 4.7b was done using Au(111) as reference in order to obtain the parameters of the molecular unit cell. Due to the non-spherical geometry of the MCP, a fringe field is applied between grid 2 and the MCP to preserve k_{II} in the LEED pattern. Therefore, the observed spots need to be corrected. The c_{fac} denotes the correction factor which might be dependent on the energy and the spot position r_{spot}. The LEED pattern measured for a clean Au(111) surface allows us to obtain the relationship between c_{fac} and observed r_{spot}. In conclusion, the obtained unit cell vectors are $a_1 = 8.39\,\text{Å}$, $a_2 = 9.76\,\text{Å}$, with an angle $\gamma = 50°$. These values are in good agreement with the real-space images measured directly by STM. The formation of an oblique lattice, instead of a square lattice like in the case of TCNQ on Au(111)[54], and the misaligned between molecules and moiré is a consequence of competition between intermolecular and molecule-substrate interactions.

4.1.2 TCNQ on graphene/Ir(111)

To show the effect of the substrate in the molecular adsorption, we repeat the previous experiments for in graphene/Ir(111) [40]. As demonstrated earlier (Sec. 3.3), in this case the interaction between the graphene and the metal is weaker than in the case of graphene/Ru(0001), leading to the appearance of several moiré superstructures [11]. In our samples, the most abundant is the (10×10) moiré periodicity but there is still some patches of (2×2) moiré. The corrugation of these moirés is between 0.2 and 0.4 Å, much smaller than in the case of ruthenium, and the surface potential is almost homogeneous in each moiré, with only a small difference between them. It is worth noting that this surface is very different than graphene/Ru(0001) although the surface is still graphene.

Figure 4.9a shows a large STM image of graphene/Ir(111) surface after the deposition of a small amount of TCNQ molecules. Although at this particular tunnel parameter the moiré superstructure is not visible, it is possible to identify the characteristic wrinkles of graphene on iridium. We can also observe some small protrusions at the edges of the steps. Zooming in these areas (Fig. 4.9b) shows that these protrusions correspond to TCNQ molecules. The molecules adsorb both parallel and perpendicular to the step edge and correspond to molecules which have diffused from terrace. This behavior is a clear indication of low diffusion barriers for the TCNQ molecules and converts the image acquisition in a cumbersome task, even at low temperatures and worst than in the case of TCNQ/graphene/Ru(0001). From these data, we can conclude that the diffusion barrier for the molecules on the surface is lower than in the case of graphene/Ru(0001).

Contrary to the growth of two dimensional metallic clusters in graphene/Ir(111) [18, 44], not preferential adsorption sites within the moiré unit cell are found for the TCNQ molecules. Increasing the coverage, the steps edges act as nucleation points for the molecules which begin to arrange in a close packed structure along the steps. These structures grow forming well-ordered islands which preserves its structural continuity across the steps, see Fig. 4.9c. The TCNQ islands are stable at the temperature of our experiments (77 K and 4.6 K) allowing us to acquire high resolution images of the boundaries of the islands, as the one shown in Fig. 4.9d.

Figure 4.10a shows the typical STM topographic image obtained for a molecular coverage equivalent to one monolayer. The TCNQ monolayer exhibits the same arrangement as the close packed islands and is only interrupted by the characteristic wrinkles of graphene/Ir(111) which are not covered with molecules. In order to obtain information about the molecular structure, we calculated the FFT of the large STM topography shown in Fig. 4.10a. Figure 4.10b shows the corresponding FFT, the spots corresponding to the moiré superstructure are indicated by a white dotted hexagon and several spots that correspond to the molecular lattice are indicated by yellow dotted lines (Fig. 4.10b). A molecular resolved STM image of the TCNQ monolayer (Fig. 4.10c) gives directly the real-space molecular structure. The

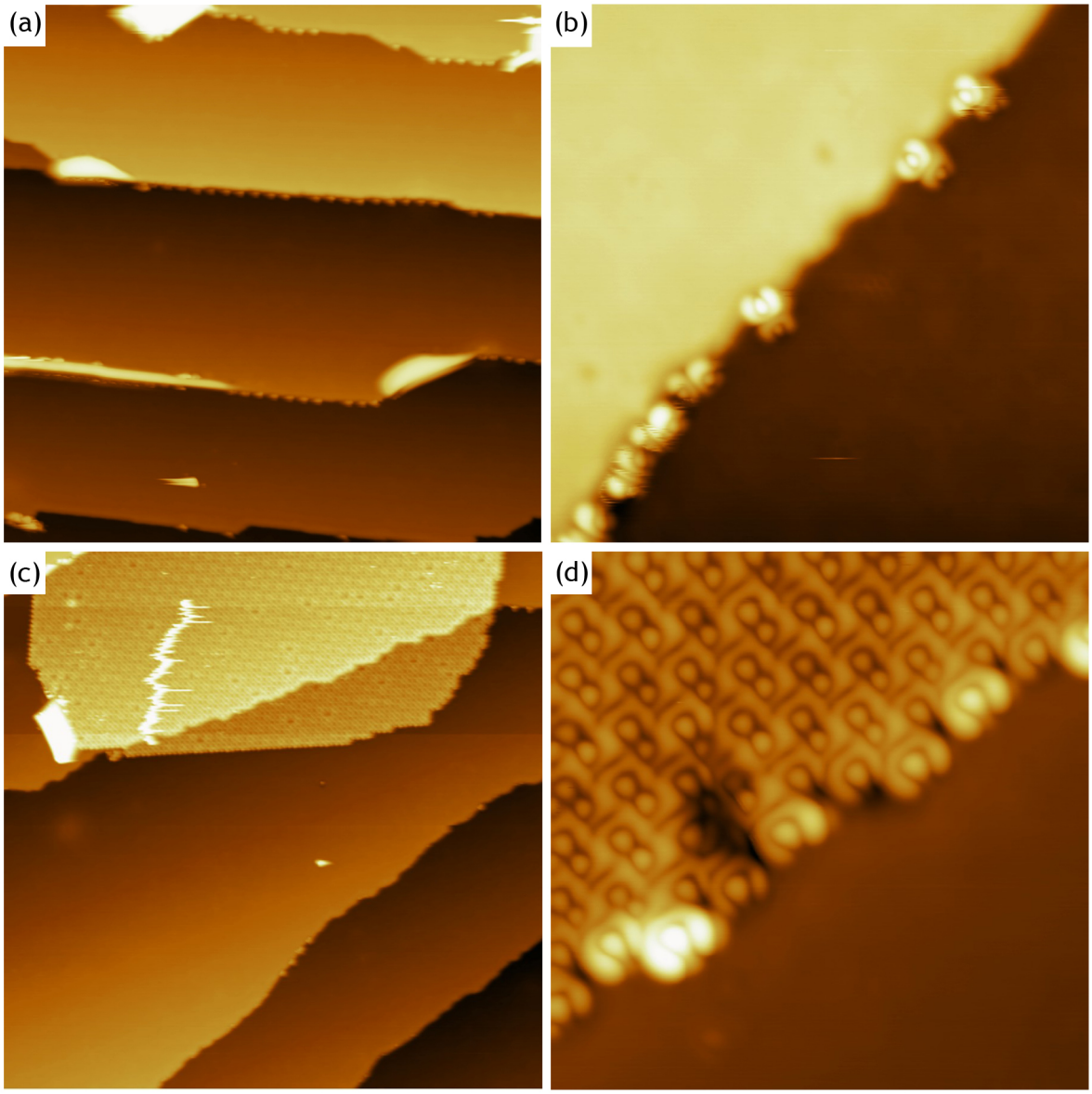

Figure 4.9: STM images for low coverage of TCNQ on graphene/Ir(111). At the beginning the TCNQ molecules adsorb at the step edges. (a) $100 \times 100\,\mathrm{nm}^2$, $V_\mathrm{b} = 1\,\mathrm{V}$, $I_\mathrm{t} = 10\,\mathrm{pA}$. (b) $15 \times 15\,\mathrm{nm}^2$, $V_\mathrm{b} = -1\,\mathrm{V}$, $I_\mathrm{t} = 10\,\mathrm{pA}$). Increasing the coverage the molecules form islands. (c) $100 \times 100\,\mathrm{nm}^2$, $V_\mathrm{b} = 1\,\mathrm{V}$, $I_\mathrm{t} = 50\,\mathrm{pA}$. (d) Island edge ($9 \times 9\,\mathrm{nm}^2$, $V_\mathrm{b} = 1\,\mathrm{V}$, $I_\mathrm{t} = 20\,\mathrm{pA}$).

yellow arrows indicate the unit cell vectors of the adsorbate lattice and the white arrows the moiré unit cell vectors. The investigations of the FFT images lead to an almost square molecular lattice where the length of the unit cell vector is 0.9 ± 0.1 Å and the angle is $84 \pm 1°$. One of the molecular axes is rotated by $22 \pm 1°$ with respect to one high-symmetry direction of graphene lattice. For this reason, several domains are observed in the STM images. Similar results were obtained for cobalt phthalocyanine (CoPc) on graphene/Ir(111) [59] and

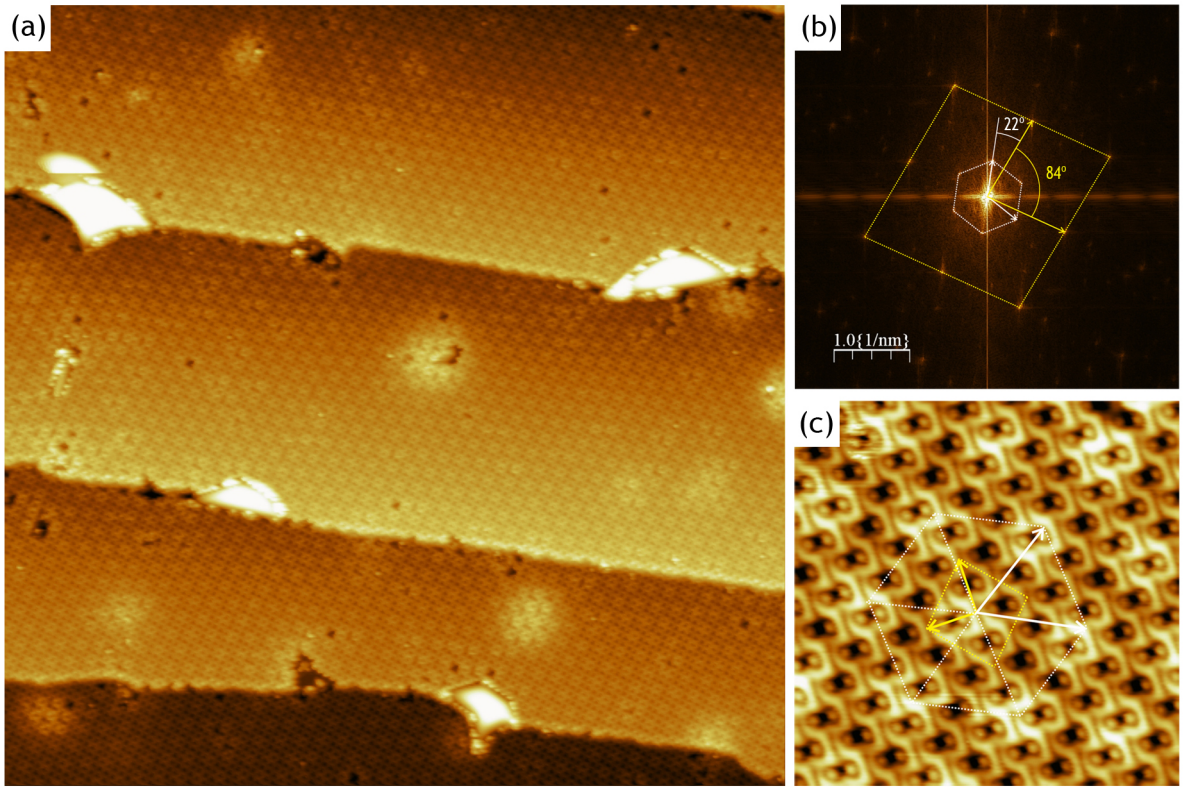

Figure 4.10: (a) Large STM image ($100 \times 100\,\mathrm{nm}^2$, $V_b = 1\,\mathrm{V}$, $I_t = 40\,\mathrm{pA}$) of a self-assemble domain of TCNQ on graphene/Ir(111). The moiré superstructure of graphene is superimposed with the molecular corrugation. (b) FFT of the image (a). The white dotted hexagon indicates the high-symmetry directions and the white arrows correspond to the unit vectors of the moiré unit cell. The molecular unit cell is indicated by dotted yellow lines and the corresponding molecular unit vectors by yellow arrows. (c) Zoom of image (a) with intramolecular resolution ($9 \times 9\,\mathrm{nm}^2$, $V_b = 1\,\mathrm{V}$, $I_t = 40\,\mathrm{pA}$). The moiré and molecular unit cells are indicated in the same way than in (b).

iron phthalocyanine (FePc) [56] and the azabenzene 1,3,5-triazine [60] on graphene/Pt(111). The molecular lattice is stabilized by hydrogen bonds between the neighboring molecules and the π-π^* interaction binds the molecules to the substrate. In this system the molecule-molecule interaction via the formation of the hydrogen bonds is the driving force for the final molecular arrangement in the monolayer. Contrary to the case of TCNQ grown on graphene/Ru(0001), here the moiré has no influence in the molecular ordering.

The domains extend over hundred of Ångstroms and grow with the same molecular order over all of the moiré superstructures, only disrupted by some individual defects and the wrinkles of graphene/Ir(111). Figure 4.11a shows a STM image where the TCNQ monolayer covers the most common moiré superstructures of graphene/Ir(111). We can easily identify the different areas because the moiré corrugation can be seen through the TCNQ monolayer for the (10×10) moiré (see Fig. 4.11c). Depending on the tunnel parameters this effect is

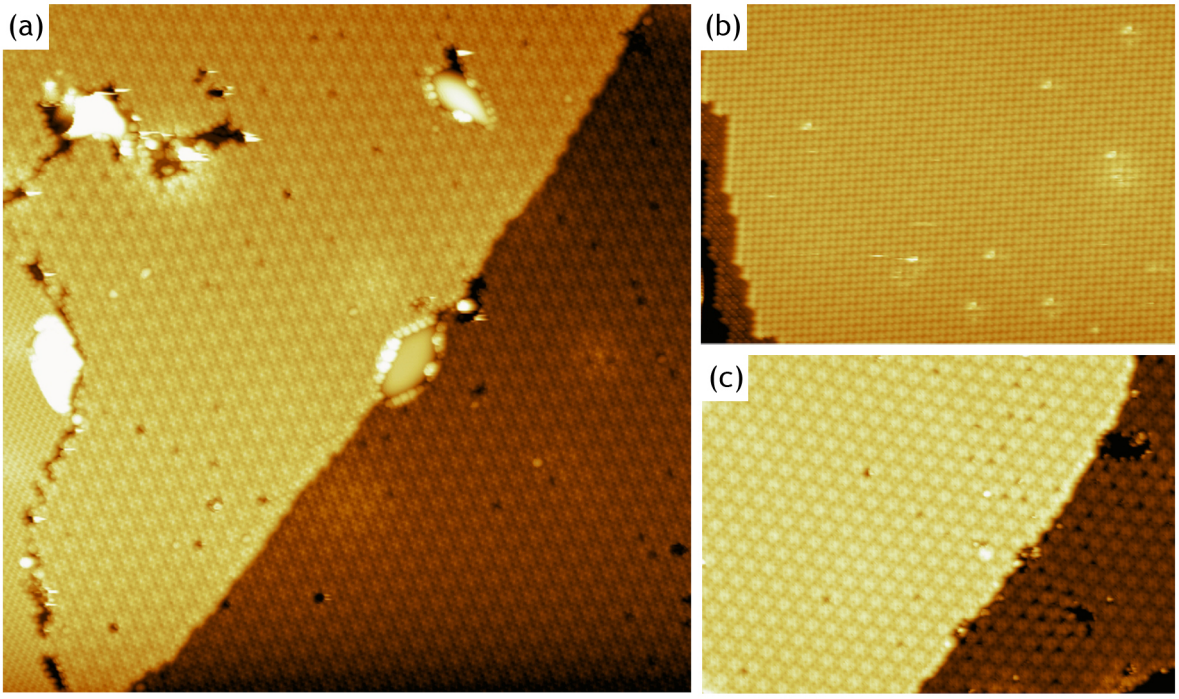

Figure 4.11: Self-assembled monolayer of TCNQ on graphene/Ir(111). (a) $75 \times 75\,\mathrm{nm}^2$, $V_b = 1\,\mathrm{V}$, $I_t = 40\,\mathrm{pA}$. The molecules growth in the same way in both moiré superstructures. (b) STM image ($60 \times 43\,\mathrm{nm}^2$, $V_b = 1\,\mathrm{V}$, $I_t = 10\,\mathrm{pA}$) of TCNQ on (2×2) moiré superstructure, (c) STM image ($60 \times 43\,\mathrm{nm}^2$, $V_b = 1\,\mathrm{V}$, $I_t = 50\,\mathrm{pA}$) of TCNQ on (10×10) moiré superstructure.

more pronounced. Meanwhile the TCNQ monolayer grown on the (2×2) domain appears flat in the STM images because the molecules are larger than the moiré unit cell, Fig. 4.11b.

To summarize, the TCNQ molecules adopt a square lattice similar than the one in bulk and in another weak interaction surfaces like Au(111) [54]. This is an indication of the minor importance in this case of the graphene surface in the molecular self-assembly process. Contrary to TCNQ on graphene/Ru(0001) where the molecular adsorption is strongly influenced by the modulation in the structure and electronic properties of the moiré pattern and the molecular arrangement in the monolayer is an oblique lattice.

4.2 F_4-TCNQ

So far, we have studied the influence of the molecule-substrate in the TCNQ self-assembly. Now, we are going to analyze how the self-assembly process is affected when the attractive intermolecular interaction of the TCNQ molecules is substituted by the repulsive interaction of a molecule of the same family, F_4-TCNQ. In this case, the central ring is bearing four fluorine atoms instead the four hydrogen in the TCNQ molecules (see Fig. 4.12a). This substitution changes the electrostatic potential of the molecule increasing its electron affinity

(5.2 eV) with respect to TCNQ (3.0 eV) [61, 62], but keeping intact the molecule geometry. Just as in the case of TCNQ molecules, F_4-TCNQ has the ability to form CTC and has been employed to enhance conductivity of various molecular charge-transport materials via doping, and to enhance hole-injection in organic electronics devices [63, 64] included graphene [65]. Figure 4.12b and 4.12b show the gas phase HOMO and LUMO for F_4-TCNQ which present more nodes that the TCNQ ones due to the participation of fluorine *p* orbitals.

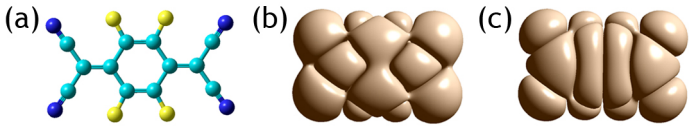

Figure 4.12: (a) Chemical structure of F_4-TCNQ molecule (dark blue = nitrogen atoms, gray = carbon atoms, yellow = nitrogen atoms). Frontier molecular orbital of F_4-TCNQ in gas-phase, (b) HOMO and (c) LUMO.

4.2.1 F_4-TCNQ on graphene/Ru(0001)

We evaporate the F_4-TCNQ molecules on graphene/Ru(0001) with the sample at room temperature and after that we cool down the sample to 4.6 K or 77 K in order to record the STM images. Similar to the case of TCNQ on graphene/Ru(0001), at low coverages (Fig. 4.13a), the molecules lie planar in the low areas of the moiré. These observations go against previous experiments of F_4-TCNQ adsorption on graphene/SiC(0001) where XPS experiments reveal that different N species exist in the deposited molecular film and the authors take this as indication that most of the molecules are standing upright [66].

In our case, the molecules present a spatial selectivity in the adsorption at low areas. As it was previously discussed (Sec. 3.2), we can distinguish four regions in the graphene/Ru(0001) moiré unit cell: the *atop*, *fcc*, *hcp* and bridge (area between *fcc* and *hcp* regions). Interestingly, at very low coverage, the molecules are adsorbed only in one half of the unit cell of the graphene/Ru(0001) (see inset of Fig. 4.13a). Comparing the STM images with the DFT calculations [33], we can identify this half of the unit cell with the *fcc* region (red triangle) because they appear brighter than *hcp* areas (blue triangle) in the STM images at certain bias voltages. This preferential adsorption in the *fcc* regions has been previously reported for the growth of Pt clusters on this surface [67]. The graphene surface provides indeed a self-organized, regular pattern of adsorption sites. In the next chapters, the subtle differences between the *fcc* and *hcp* regions will be discussed in detail.

In order to study the difference in the self-assembly of TCNQ and F_4-TCNQ molecules, we co-evaporated both molecules. Taking advantage of the high intramolecular resolution resulting from the decoupling of the molecules and the metallic substrate facilitated by graphene, we can identify both molecules. Figure 4.13b shows an STM topography at positive bias volt-

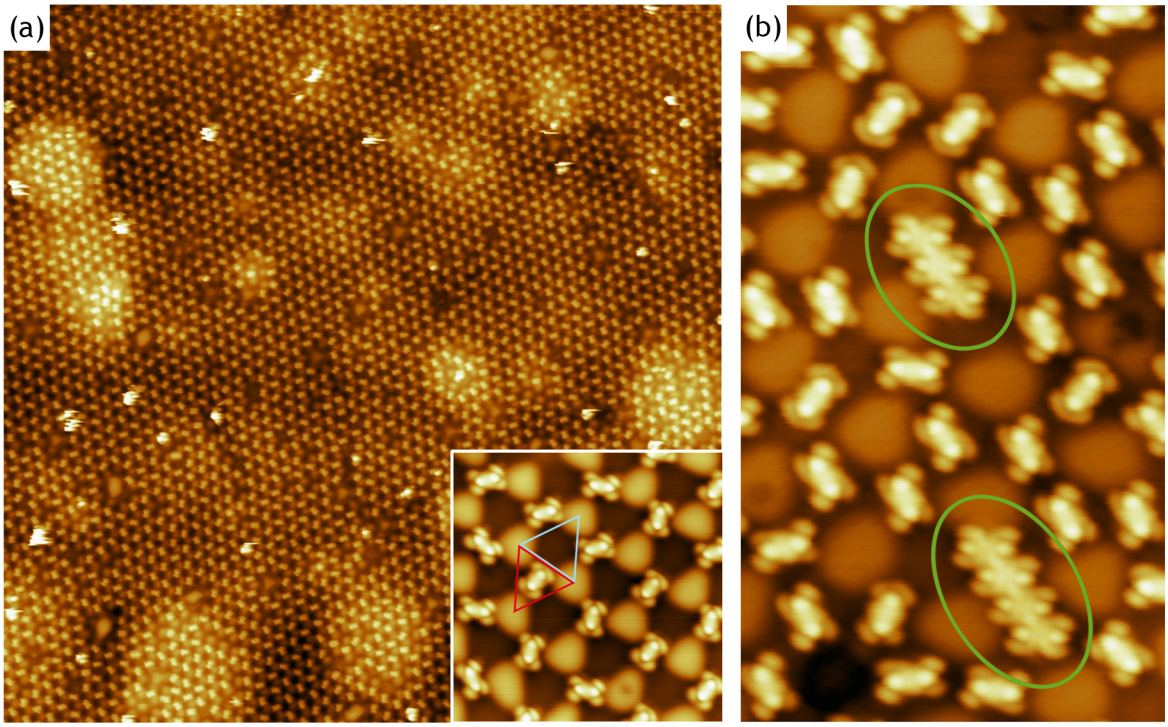

Figure 4.13: (a) Large STM images ($150 \times 150\,\mathrm{nm}^2$, $V_b = -2\,\mathrm{V}$, $I_t = 10\,\mathrm{pA}$) taken at 4.6 K after F_4-TCNQ deposition on graphene/Ru(0001). The inset shows a zoom ($12 \times 12\,\mathrm{nm}^2$, $V_b = -2\,\mathrm{V}$, $I_t = 10\,\mathrm{pA}$) where is possible to observed the spatial specific molecular adsorption. Blue and red triangles indicate the *hcp* and *fcc* regions, respectively. (b) STM image ($10 \times 17\,\mathrm{nm}^2$, $V_b = 1\,\mathrm{V}$, $I_t = 10\,\mathrm{pA}$) of the graphene/Ru(0001) surface after co-evaporation of F_4-TCNQ and TCNQ molecules. Both molecules are clearly distinguishable from each other and F_4-TCNQ molecules tend to be isolated while TCNQ molecules form molecular chains held together by the hydrogen bonds.

age with both molecules adsorbed on the graphene/Ru(0001) surface. We can easily distinguish between them exclusively on the basis of the frontier molecular orbital shape and the interaction between molecules. TCNQ molecules form small chains (greed circles Fig. 4.13b) and all the F_4-TCNQ molecules always appear alone. This result points out the importance of the intermolecular interaction in the self-assembly process. The presence of the fluorine atoms avoids the formation of hydrogen bonds, and therefore the molecules adsorbed on the low areas try to minimize the interaction between the cyano groups and the fluorine atoms of the neighboring molecules. For this reason, at low coverages, the F_4-TCNQ molecules appear always isolated (see Fig. 4.13). Further observation shows that there are F_4-TCNQ molecules adsorbed on the two halves of the moiré unit cell in Fig. 4.13b. The reason for this is that the F_4-TCNQ coverage in this image is slightly higher than the one of Fig. 4.13a. As mentioned above, the F_4-TCNQ molecules began to adsorb in the *fcc* areas of the moiré pattern. When all the *fcc* regions are occupied with F_4-TCNQ molecules, they begin to adsorb in the *hcp*

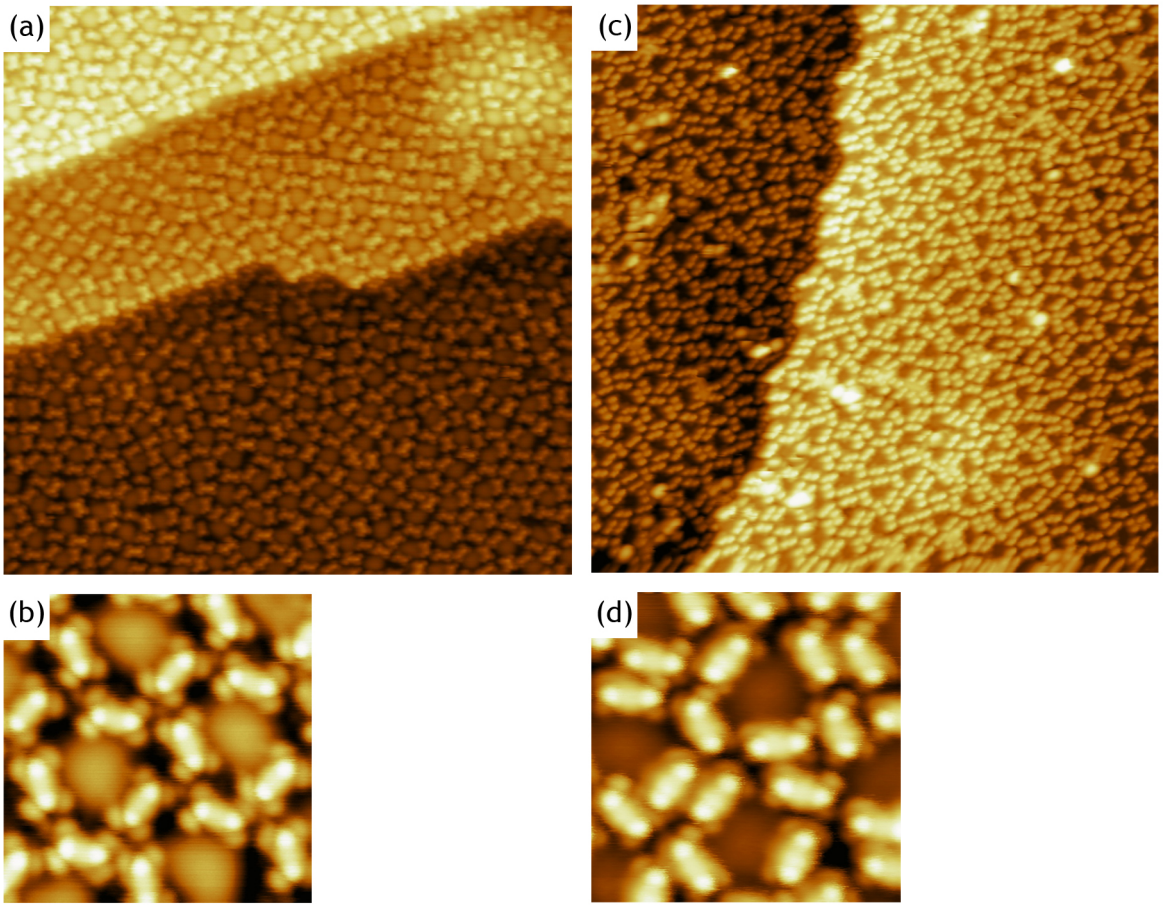

Figure 4.14: Coverage evolution of F_4-TCNQ on graphene/Ru(0001) at 4.6 K. STM images corresponding to intermediate coverage: (a) $50 \times 50\,\mathrm{nm}^2$, $V_b = -1\,\mathrm{V}$, $I_t = 5\,\mathrm{pA}$ and (b) $6.5 \times 6.5\,\mathrm{nm}^2$, $V_b = -0.5\,\mathrm{V}$, $I_t = 5\,\mathrm{pA}$. Medium coverage: (c) $50 \times 50\,\mathrm{nm}^2$, $V_b = 1\,\mathrm{V}$, $I_t = 20\,\mathrm{pA}$ and (d) $6 \times 6\,\mathrm{nm}^2$, $V_b = 1\,\mathrm{V}$, $I_t = 20\,\mathrm{pA}$.

regions as can be seen in Fig. 4.13b.

When the coverage is increased above 1/3 ML, F_4-TCNQ molecules cover the low areas of the moiré, see Fig. 4.14. Due to the electrostatic repulsion between them, the molecules are displaced from the *fcc* to bridge positions, where each molecule has two cyano groups in the *fcc* area and the other two in the *hcp* area. When the coverage reaches 3 molecules per moiré unit cell, the most stable configuration corresponds to a triangular ring structure where the cyano groups of one molecule is between the cyano groups of the other two remaining, as can be seen in 4.14b. Further increasing the coverage forces the appearance of another stable configuration where two F_4-TCNQ molecules adsorb in parallel between high areas of the moiré and short lines of molecules are visible (Fig. 4.14c and 4.14d). These lines of molecules were also observed for F_4-TCNQ adsorbed close to Cu(100) steps [68].

The spatial selectivity in the adsorption and the repulsive interaction between molecules

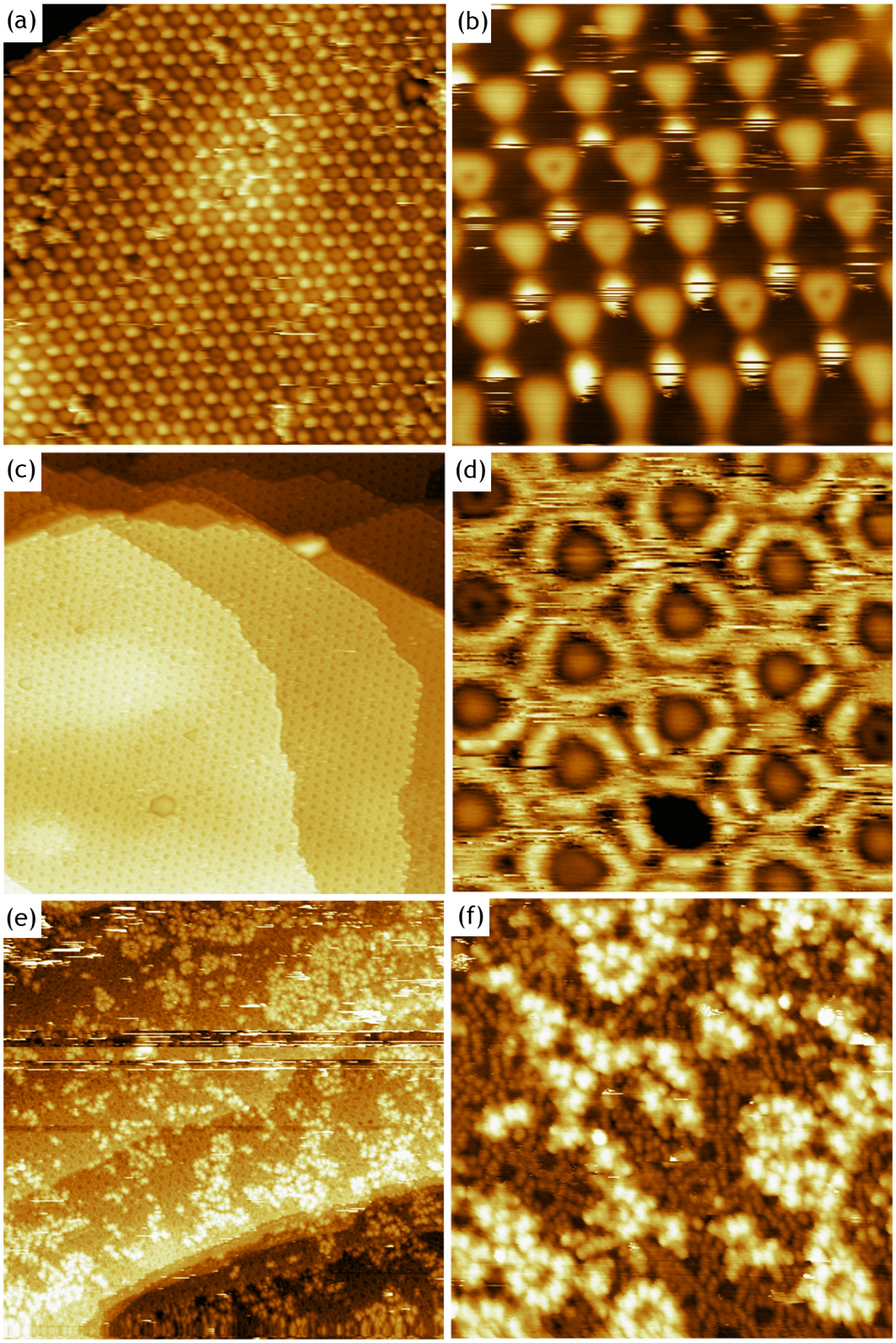

Figure 4.15: STM images of F_4-TCNQ on graphene/Ru(0001) taken at 77 K. Intramolecular resolution is lost by the effect of the temperature. At 77 K the molecules rotate onto their molecular adsorption site. Low coverage: (a) $45 \times 45\,\mathrm{nm}^2$, $V_\mathrm{b} = -1\,\mathrm{V}$, $I_\mathrm{t} = 5\,\mathrm{pA}$ and (b) $15 \times 15\,\mathrm{nm}^2$, $V_\mathrm{b} = -1.5\,\mathrm{V}$, $I_\mathrm{t} = 5\,\mathrm{pA}$. Intermediate coverage: (c) $100 \times 100\,\mathrm{nm}^2$, $V_\mathrm{b} = -1\,\mathrm{V}$, $I_\mathrm{t} = 5\,\mathrm{pA}$ and (d) $10 \times 10\,\mathrm{nm}^2$, $V_\mathrm{b} = -1.5\,\mathrm{V}$, $I_\mathrm{t} = 5\,\mathrm{pA}$. High coverage: (e) $100 \times 100\,\mathrm{nm}^2$, $V_\mathrm{b} = -2\,\mathrm{V}$, $I_\mathrm{t} = 5\,\mathrm{pA}$ and (f) $25 \times 25\,\mathrm{nm}^2$, $V_\mathrm{b} = -1.5\,\mathrm{V}$, $I_\mathrm{t} = 5\,\mathrm{pA}$.

are more evident when we increase the temperature to 77 K, see Fig. 4.15. At this temperature, the molecules are observed as round protrusions on the surface without any intramolecular resolution. We assign this change in the appearance to a temperature-induced motion of the molecule locked in its adsorption site. Upon increasing the F_4-TCNQ coverage the molecules cover completely the low areas of the moiré and this effect is more clear, Fig. 4.15c and 4.15d. At first glance, we observe a porous molecular network with a periodicity of 3 nm similar to the one of the Fig. 4.14a. However, in a close inspection, Fig. 4.15d, we observe a ring around the high areas of the moiré where it is not possible to distinguish the F_4-TCNQ molecules. The reason for this might be that at this temperature the molecule moves around the high areas of the moiré faster than the scan rate used for imaging and the time-averaged image shows a ring.

Increasing the deposition time never produces a perfect monolayer like in the case of TCNQ on graphene/Ru(0001). The repulsive interaction between molecules and the inhomogeneous properties of the moiré pattern of graphene/Ru(0001) causes that F_4-TCNQ molecules never adsorb in the high areas of the moiré filling the hole of the network, as was reported on the accommodation of iron phthalocyanine (FePc) and tert-butyl zinc phthalocyanine ((t-Bu)4-ZnPc) molecules by the porous Kagome lattice of FePc molecules on graphene/Ru(0001) [56]. As Fig. 4.15e and 4.15f show the F_4-TCNQ molecules begin to growth the second layer before the completion of the first one.

4.2.2 F_4-TCNQ on graphene/Ir(111)

In this subsection we will discuss the adsorption of F_4-TCNQ on graphene/Ir(111). Figure 4.16a shows STM images recorded at 77 K after depositing the F_4-TCNQ molecules on the graphene/Ir(111) surface held at room temperature. The terraces of the surface are covered with a fairly regular array of bumps, each one corresponding to a single F_4-TCNQ molecule. They form an hexagonal arrangement with distances dictated by the underlying moiré pattern of graphene/Ir(111) (2.45 nm). Fig. 4.16b reproduces a zoom of the large image. It shows that the F_4-TCNQ molecules adsorb exclusively in one half of the unit cell of graphene/Ir(111), marked with blue triangles. A similar preference for adsorption has been reported for clusters of Ir [18] and other metals [44] grown on graphene/Ir(111), and in the previous case of F_4-TCNQ on graphene/Ru(0001).

The observed selectivity of the adsorption at specific areas of the moiré is surprising, given that the difference between a *hcp* adsorption site and the *fcc* one is only apparent when the second metallic layer below the surface is taken into account. The electronic structure of graphene/Ir(111) does not reveal important changes when moving across the moiré unit cell, with work function, image states or density of states being essentially identical for *atop*, *hcp* or *fcc* areas (Sec. 3.3). For clean graphene/Ir(111), the direct bonding of three C atoms with atop Ir atoms at the *hpc* areas promotes some degree of $sp2$ to $sp3$ rehybridization that could act

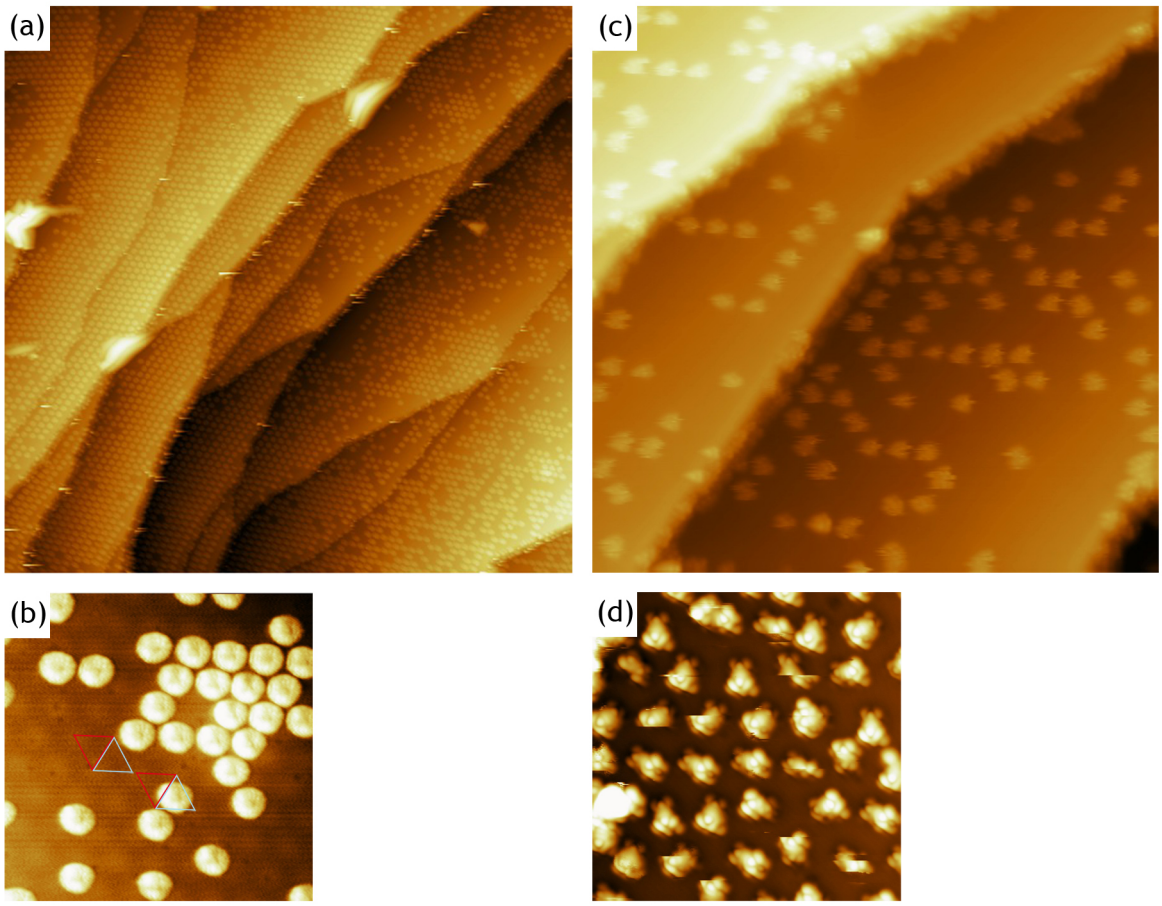

Figure 4.16: (a) Large STM images of F_4-TCNQ on graphene/Ir(111) taken at 77 K ($170 \times 170\,nm^2$, $V_b = -1\,V$, $I_t = 5\,pA$). (b) Zoom of $20 \times 20\,nm^2$ acquired at $V_b = -2\,V$, $I_t = 5\,pA$. Blue and red triangles indicate the *hcp* and *fcc* regions, respectively. (c) Large STM image of F_4-TCNQ on graphene/Ir(111) taken at 4.6 K ($50 \times 50\,nm^2$, $V_b = 1\,V$, $I_t = 20\,pA$. (d) Zoom of $15 \times 15\,nm^2$ acquired at $V_b = -1\,V$, $I_t = 3\,pA$.

on the other three C atoms of the hexagon to facilitate their binding to incoming molecules [45]. DFT calculations have reported that the C-Ir direct bond on *atop* sites is slightly shorter at the *fcc* areas (3.77 Å) than at the *hcp* regions (3.80 Å) [45]. As a result, the reactivity of the three non bonded C atoms and, thus, the local binding energy minimum for molecules could be slightly larger at the *hcp* sites than at the *fcc* ones, in agreement with the observed specificity of the adsorption.

To get an insight on the origin of the shape of the molecules we cool down the sample and perform STM images at 4.6 K, see Fig. 4.16c and 4.16d. At this temperature, the molecules present the same arrangement following the moiré pattern of graphene and avoiding molecular islands, although they are mobile on the surface. A close inspection, Fig. 4.16d, reveals that we can distinguish some intramolecular details, although during the scanning,

the movement of the molecule is enhanced by the interaction with the tip and sometimes the molecules move to the next energy minimum position. This effect is a clear indication of the small diffusion barrier of graphene on iridium.

4.3 Conclusions

In this chapter, we have explored the mutual interaction between acceptor molecules in graphene on Ru(0001) and Ir(111). The first important result is that graphene monolayer efficiently decouples the molecules from the strongly interacting metallic surface allowing us to chemically identify individual molecules using the intramolecular resolution. The electronically homogeneous and almost neutral graphene/Ir(111) surface is an ideal playground to explore the mutual interaction between molecules in two dimensions. On the other hand, graphene/Ru(0001) shows charge inhomogeneities and a surface potential corrugation which give rise to stronger long-range lateral variations in the substrate–adsorbate interaction.

In Sec. 4.1, we studied the molecular self-assembly of TCNQ on graphene/Ru(0001) and graphene/Ir(111). For these molecules, the growth behavior is dominated by intermolecular attractive interactions and results in the formation of a compact monolayer in both cases. At low coverage, the surface potential corrugation of graphene/Ru(0001) forces the molecules to adsorb in the lower areas of the moiré pattern, where the surface potential is small. When the coverage is increased the molecules continue covering the lower areas of the moire avoiding the upper areas and stabilizing the structure by means of hydrogen bonds between neighboring molecules. The combined effect of the preferential adsorption in the lower areas of the moiré and the formation of hydrogen bonds allow us to produce a highly ordered porous molecular network with a periodicity of 3 nm. Finally, for a coverage equivalent to a monolayer the molecules cover completely the surface forming an oblique lattice and resulting in the formation of six equivalent domains. Contrary to the graphene/Ru(0001), the deposition of TCNQ on graphene/Ir(111) come out in the formation of well-ordered islands from the very beginning. For this system, the moiré does not affect the adsorption structure and the molecules self-assemble in a square lattice.

In the case of F_4-TCNQ, the absence of the hydrogen atoms in the central ring prevents the molecules to condensate into islands and promotes a selective adsorption in specific areas of the moiré, in both surfaces. The charge and surface potential inhomogeneities of the graphene/Ru(0001) surface help to the formation of a triangular ring structures which lead to a peculiar second layer growth, avoiding, even at high coverages, the high areas of the moiré. In the case of graphene/Ir(111), the lateral repulsion between molecules is strong enough to lock the molecules in their adsorption sites even at 77 K. At this temperature the molecules moves around their adsorption sites and are imaged with a toroidal shape. It is

necessary to decrease the temperature at 4.6 K to get some intramolecular resolution even though the injected tunneling current is enough to induce the movement of the molecules.

In conclusion, we have shown that the moiré pattern of graphene epitaxially grown on metallic surfaces, is able to induce spatial selectivity in the adsorption of both F_4-TCNQ and TCNQ molecules, resulting in a periodic superlattice of adsorbed molecules of widely different properties. This finding paves the way to modify the properties of graphene.

5 Tunneling spectroscopy: From single molecules to monolayers

In this chapter we study the electronic properties of the TCNQ molecules adsorbed on graphene/Ru(0001) and graphene/Ir(111) by means of STS experiments. These studies allow us to identify the frontier molecular orbital of TCNQ in both cases and the charge transfer between molecules and graphene.

5.1 TCNQ on graphene/Ru(0001)

As it was discussed in the previous chapter, TCNQ molecules follow a hierarchical way of growing when deposited on graphene/Ru(0001). Starting from a random distribution of molecules adsorbed in the low areas of the moiré pattern at low coverage, finishing with the formation of a perfect monolayer at the saturated coverage. In this section, we will explore the electronic properties of this system by means of STS and the support of DFT calculations performed by the group of Prof. Fernando Martín.

5.1.1 Imaging frontier molecular orbital

Firstly, we performed spatially resolved STS in single TCNQ molecules in order to characterize their electronic structure, see Fig. 5.1a. The spectrum measured on the graphene surface (red curve) is essentially featureless when measured with this low value of tunneling current (20 pA). It only presents the already known asymmetry between the occupied and empty density of states when moving from the ripples to the low areas [23]. On the contrary, the spectrum measured on the TCNQ molecules (black curve) shows three clear features marked with black vertical lines. For negative bias voltages, there are two peaks at -2.0 V and -0.86 V and for positive bias voltages, it presents higher intensity in the differential tunneling conductance around $+1.0$ V than the spectra measured in graphene. In order to identify the origin of these features, panels of Fig. 5.1b show the topographic images taken at these particular bias voltages. It is known that the intramolecular resolution of the STM images for molecules adsorbed on insulating layers can be usually correlated to the spatial distribution of their molecular orbitals.

Notice that all the STM images were taken in the same area however, the adsorption orientation of TCNQ molecules in the different images changed due to the interaction between

molecules and tip. The negative and positive sample bias voltages correspond to the occupied states and unoccupied states, respectively. Thus, in the case of the peak at $-2.0\,\mathrm{V}$ is not surprising that the STM image taken at this voltage represents the HOMO spatial distribution of the molecules (Fig. 4.1b). Meanwhile the STM images at $-0.86\,\mathrm{eV}$ and $+1.0\,\mathrm{eV}$ show the same intramolecular resolution that remains to the LUMO of the neutral TCNQ in gas phase (Fig. 4.1c) with a node in the middle of the molecule. Therefore, we are visualizing the LUMO of the neutral molecule below (occupied states) and above (empty states) the Fermi level. This is a clear indication of a charge transfer between the graphene and the molecules.

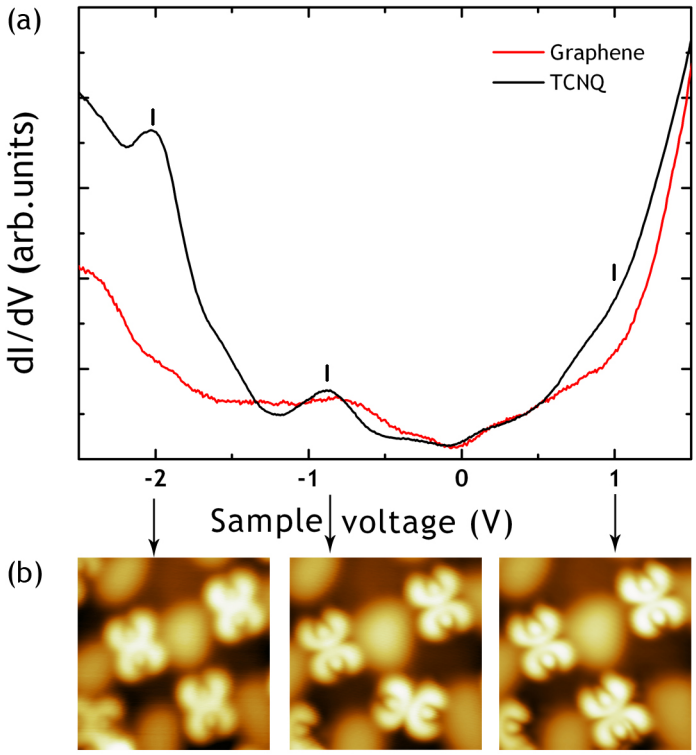

Figure 5.1: (a) STS data measured on graphene (red curve) and on a TCNQ molecule (black curve). Two peaks, marked with black vertical lines, at negative bias voltages (occupied states) and one at positive bias voltage (empty state) can be observed. (b) STM images ($4.5 \times 4.5\,\mathrm{nm}^2$, $I_t = 20\,\mathrm{pA}$) of TCNQ molecules deposited on graphene/Ru(0001) at different bias voltage indicated by arrows. The intramolecular resolution of the images allows us to identify the molecular orbitals.

To get some insight on the experimental data and the electronic structure, the group of F. Martín [36] have performed DFT calculations including vdW interactions using the empirical correction scheme proposed by Grimme (DFT+D2) [69]. Accounting for vdW interactions is essential to obtain adsorption energies and geometries of aromatic molecules in good agreement with experiments [70–72]. Besides, it is also essential for a correct description of the moiré pattern present in graphene/Ru(0001) [33]. To study the adsorption of the TCNQ

molecule on this system, the atomic positions of the relaxed graphene/Ru(0001) unit cell have been frozen and only the molecule has then been allowed to relax. This is a reasonable approximation due to the relatively high stiffness of the graphene/Ru(0001) substrate in comparison with, e.g., metal surfaces.

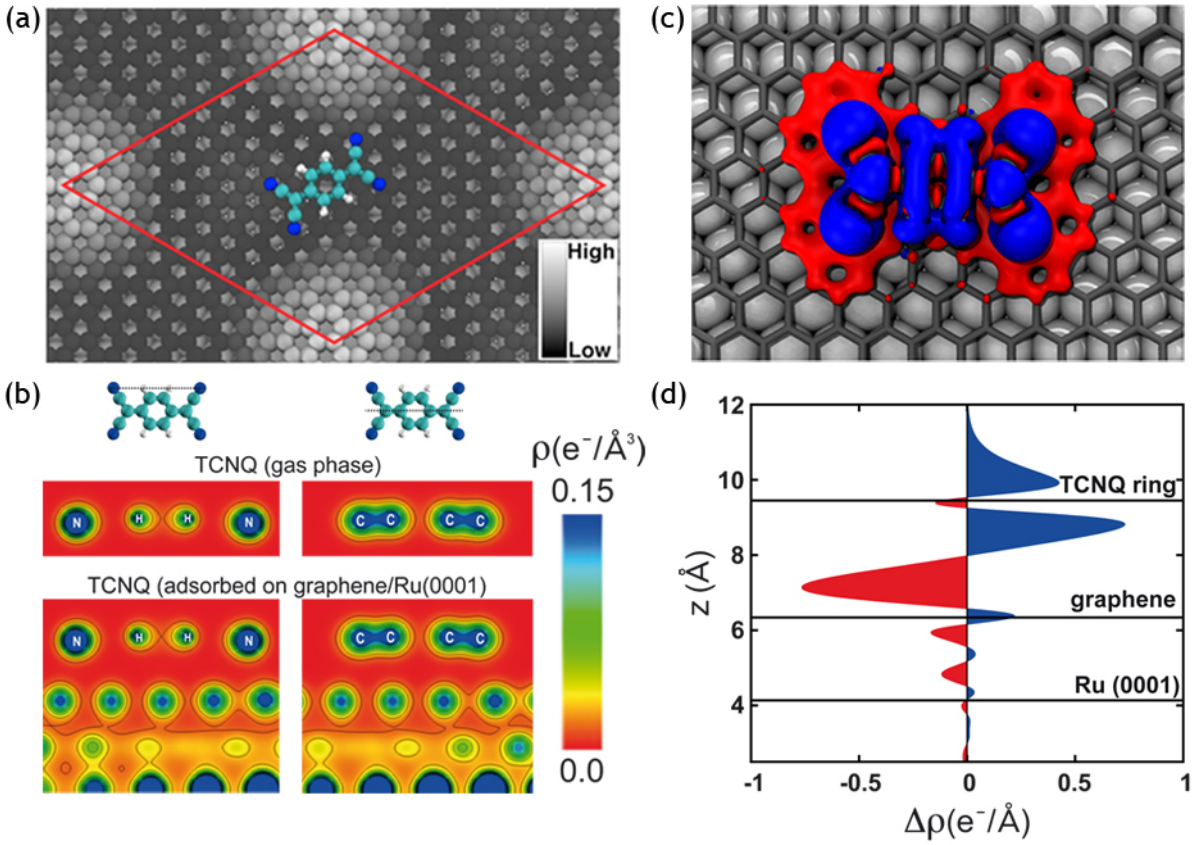

Figure 5.2: (a) Adsorption geometry corresponding to the maximum adsorption energy ($E_b = -2.62$ eV). The color code of the substrate indicates the different heights of the graphene atoms with respect to the Ru substrate underneath, with white corresponding to the higher parts of the ripples. (b) Charge transfer maps of TCNQ on graphene/Ru(0001). The lower panels show two-dimensional cuts of the *xy*-plane for the adsorption configuration of TCNQ. The two cuts are indicated by dotted lines in the upper part of the panel. The central part shows the charge distribution for a free standing, charged TCNQ molecule. Notice that the charge distribution is identical for the adsorbed and the freestanding, but charged molecule. (c-d) Electronic density redistribution upon adsorption of TCNQ on graphene/Ru(0001): (c) top-view isocountour surface and (d) integrated in *xy*-plane. Blue color indicates an excess in the electron density while red color indicates a charge depletion.

Although no clear preferential adsorption site in the low area of the moiré is observed in the STM images, the highest fraction of molecules is found to lie at the bridge site, between *fcc* and *hcp* areas, as it can be seen in the Fig. 5.1b. Among all the explored configurations at this site, our DFT+D2 calculations show that the most stable adsorption configuration corre-

sponds to molecules oriented along the *fcc* to *hcp* direction of the graphene layer, Fig. 5.2a. Contrary to the case of TCNQ on Cu(100) [53] where the TCNQ is chemisorbed and its molecular geometry is strongly bent, on graphene/Ru(0001), the molecule lies flat at about 3 Å above the surface. The calculated adsorption energy is 2.62 eV/molecule, in line with DFT+D2 adsorption energies obtained for similar organic molecules on graphene [73]. However, the energy difference between this configuration and any other in the lower area of the moiré pattern is less than 50 meV. These small variations in energy suggest that the molecular adsorption is equally likely in any low area, in good agreement with the experimental observations.

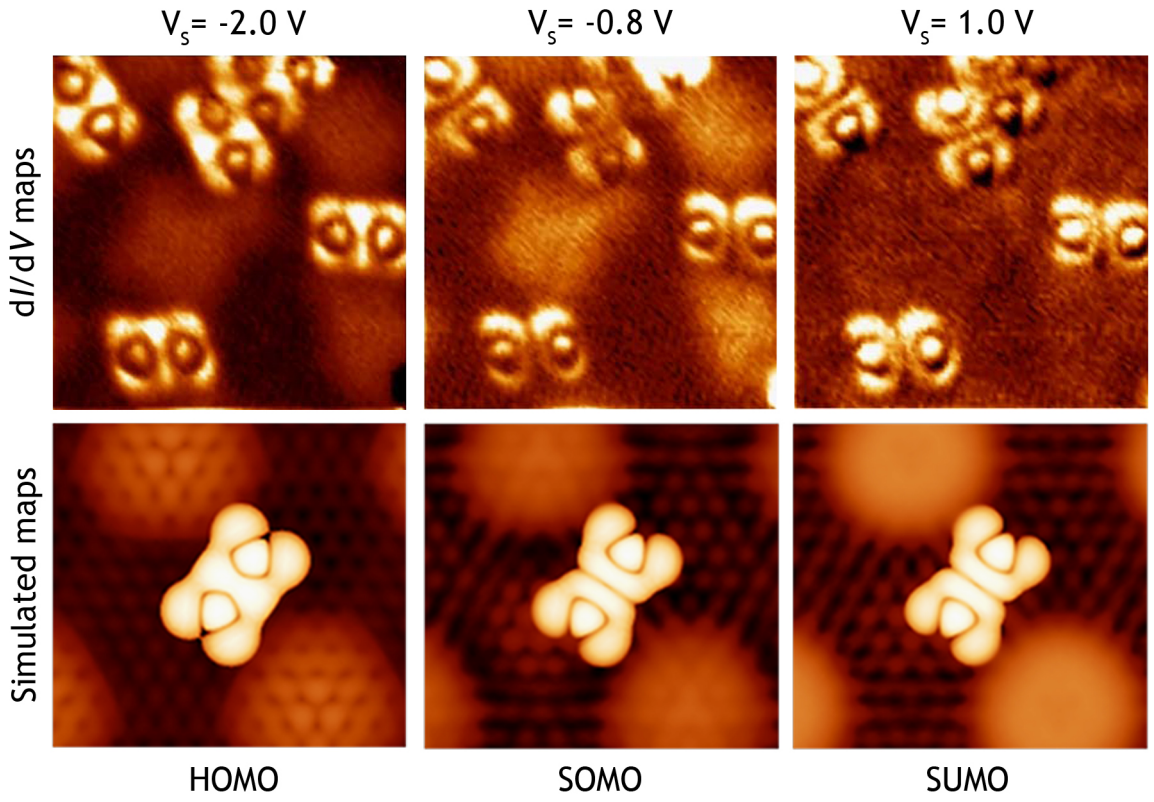

Figure 5.3: The upper row shows spatially resolved dI/dV maps of individual TCNQ molecules adsorbed on graphene/Ru(0001) recorded at three different bias voltages associated to the HOMO, SOMO and SUMO. The lower row shows the corresponding simulated dI/dV maps in complete agreement.

The calculations also reveal that the TCNQ molecule is negatively charged upon adsorption. About one electron is transferred to the molecule as it is shown by the electronic density redistribution integrated over the xy-plane(Fig. 5.2d). In this plot the blue color indicates an accumulation of charge and the red one a depletion, while the black horizontal lines correspond to the position of the Ru(0001) surface, graphene layer and the TCNQ central ring. It

can be seen that the charge transferred from graphene is located above and below the TCNQ plane causing a p-doping of the graphene layer, while the Ru substrate is essentially unaffected. Figure 5.2c represents a top-view isocountour of the charge density distributed across the molecule and it shows that the additional charge density mainly goes into the LUMO of the neutral molecule. The charge transfer per molecule is 0.99 electrons as is evaluated using Barder topological analysis of the charge density [74]. Figure 5.2b shows two vertical cuts of the charge density for TCNQ adsorbed on graphene/Ru(0001) (lower panels) compared to the charge density for a gas-phase, singly-charged TCNQ molecule (upper panels). As an evidence of the weak interaction between graphene/Ru(0001) and TCNQ molecules, this plot shows that the electronic charge distribution at the TCNQ molecule is identical in both cases and there is no charge density accumulation in the region between the molecule and the surface. Thus, the effect of the interaction with the substrate is essentially charging the molecule and the p-doping of the graphene layer.

Figure 5.3 shows the comparison between the experimental $\mathrm{d}I/\mathrm{d}V$ maps and the simulated ones. Upper panels show the experimental $\mathrm{d}I/\mathrm{d}V$ maps measured at the energy of the three features indicated in the STS spectrum of Fig. 5.1a. The simulated maps of the low panels are calculated in the corresponding range of energy and are in good agreement with the experimental data. This agreement is striking for all HOMO, SOMO and SUMO levels. The spatial distribution of these peaks confirms the partial occupation of the LUMO of the neutral molecule which now is splited in two different orbitals Single Occupied Molecular Orbital (SOMO) and Single Unoccupied Molecular Orbital (SUMO). The accurate simulations confirm then the localization of an unpaired electron transferred from graphene to the LUMO of TCNQ. In the next chapter, we will analyze in detail the effect of this unpaired electron on the magnetic properties of the system.

5.1.2 Formation of a spatially extended intermolecular band

After studying the electronic properties for single TCNQ molecules on graphene/Ru(0001) the next step is to understand the evolution of the electronic properties when the coverage is increased. As it was discussed in Sec. 4.1.1, increasing the TCNQ coverage the molecules start to interact to each other making chains of molecules and finally, a perfect monolayer.

Theoretical simulations of TCNQ monolayer on graphene/Ru(0001) predicts an adsorption energy of 1.88 eV/molecule, which is slightly smaller than the one for isolated molecules, because TCNQ molecules residing on the upper part of the ripples receive a reduced charge transfer from graphene and are, therefore, less strongly bounded than those adsorbed at the lower areas. The average charge transfer is of the order of $0.4 - 0.6$ electrons/molecule and the average TCNQ-graphene distance is the same as in the case of single TCNQ molecule adsorbed in graphene/Ru(0001). The system has been simulated by using C(11×11)/Ru(10×10) supercell [33] containing eight TCNQ molecules.

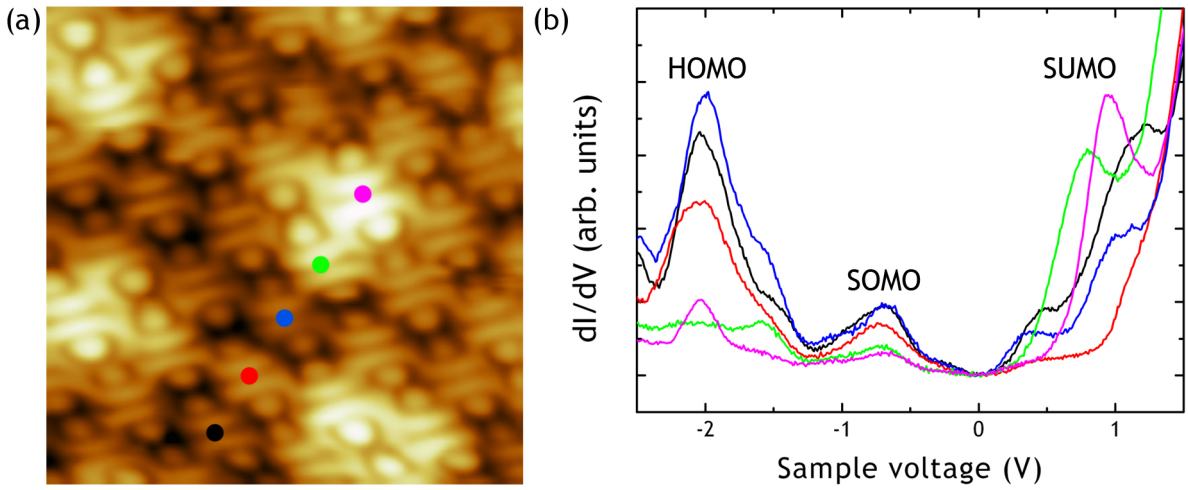

Figure 5.4: (a) STM topography ($4.7 \times 4.7\,\mathrm{nm}^2$) of a TCNQ monolayer grown on graphene/Ru(0001) recorded at 4.6 K with the tunneling gap stabilized at $V_b = +1.5\,\mathrm{V}$ and $I_t = 100\,\mathrm{pA}$. The white rhombus indicates the moiré unit cell. (b) Individual $\mathrm{d}I/\mathrm{d}V$ curves measured on molecules located in different areas of the moiré unit cell. The color code corresponds to the dots shown in (a). The peaks are the HOMO, SOMO and SUMO levels.

Figure 5.4 shows the $\mathrm{d}I/\mathrm{d}V$ spectroscopy for a TCNQ monolayer on graphene/Ru(0001). The colored circles indicate the molecules where the $\mathrm{d}I/\mathrm{d}V$ spectra were recorded. At first glance, when the monolayer is formed, no remarkable changes are observed with respect to the spectra of single molecules. All of them show the same three features that we identify with the HOMO, SOMO and SUMO. However, depending on the adsorption site of the TCNQ molecule, the intensity of the peaks is different. This fact can be understood taking into account the influence of the graphene electronic structure. As it was shown in Sec. 3.2, the graphene/Ru(0001) surface is electronically modulated leading to a modulated TCNQ-graphene interaction. Besides these changes in intensity, there is a small shift in the the energy position of the SUMO. The energy position of the SUMO for the molecules adsorbed in the high areas of the moiré is higher than the molecules adsorbed in the low areas. The origin of the shift in energy may be traced back to the electric field between the tip and sample. It is known that the electric field between the tip and the sample surface produces a Stark shift in the energy position of field emission resonance in the STS spectra [37]. In addition, even in tunneling regime, the electronic states of the molecules not strongly coupled with the substrate can be shifted in energy due to a Stark effect [75, 76]. In our case, for the molecules in the high areas of the moiré the interaction is weaker and the tip is closer to the surface. Hence, the electric field is stronger than for molecules in the low areas, a shift up in energy for their orbitals.

Striking differences as a function of the bias voltages are revealed in the topographic STM

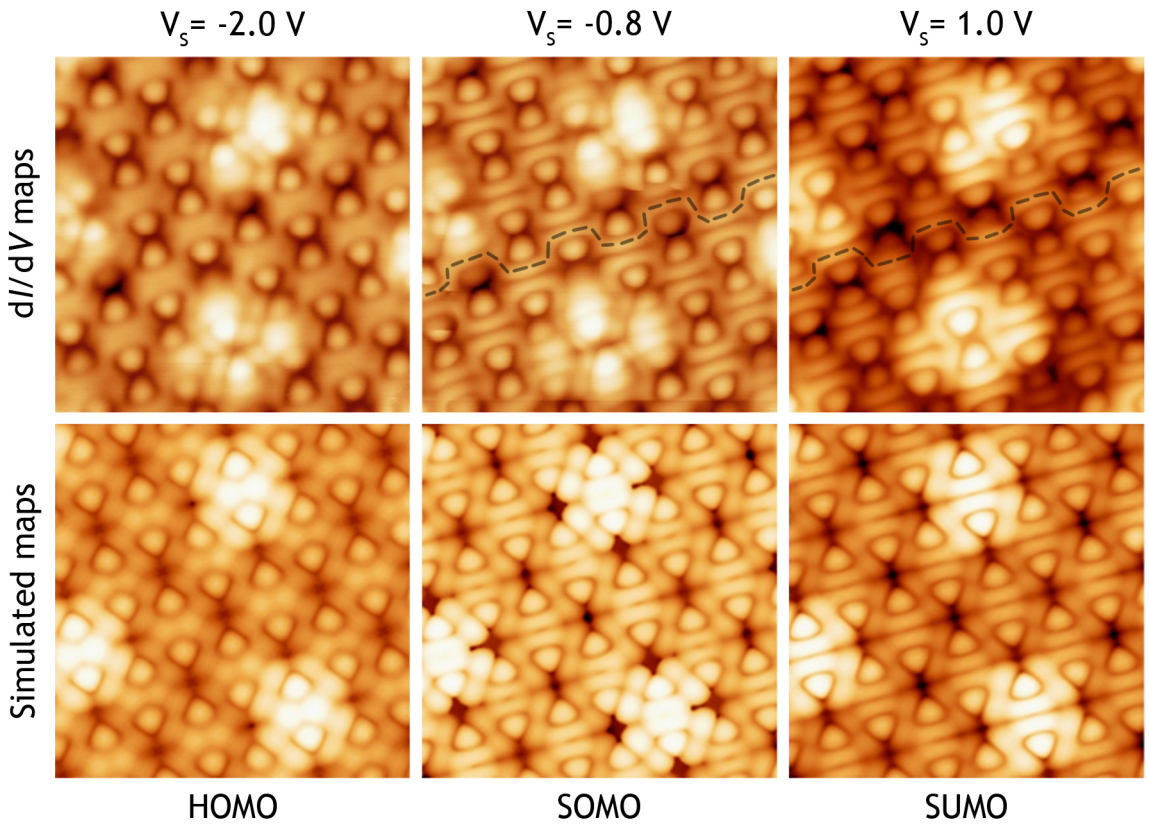

Figure 5.5: The upper row shows topographic STM images of a TCNQ monolayer on graphene/Ru(0001) recorded at three different bias voltages. The lower row shows the correspondent simulated topographic images. The black dashed lines indicate the intramolecular bands that appear at the SOMO and SUMO energies.

images of the TCNQ monolayer. The upper row in Fig. 5.5 shows the experimental STM images while the lower row shows, for comparation, the simulated images at the HOMO (-2.0 V), SOMO (-0.8 V) and SUMO ($+1.0$ V) energies. The intramolecular resolution in the STM images confirms the split of the LUMO of the neutral molecules due to the charge transfer from the graphene as in the case of single TCNQ molecules. The simulated constant current images reproduce almost exactly the experimental data for the HOMO, SOMO and SUMO, including the higher resolution of the orbital nodes observed for TCNQ molecules on the lower part of the ripples compared with the ones at the higher parts, as can be seen in the lower panels of Fig. 5.5.

Notice that the SOMO and SUMO experimental images show that the neighboring molecules are connected to each other forming tube-like structures (black dashed lines of Fig. 5.5) separated by clear nodes. These structures are the evolution of the extended orbital formed in the case of the TCNQ dimers and chains, described in the Sec. 3.2. At first glance, the hy-

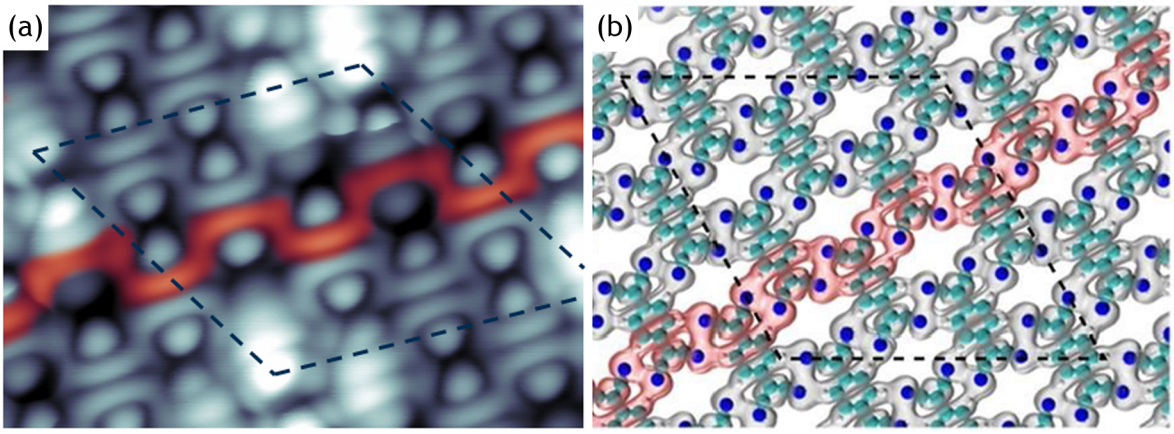

Figure 5.6: Intermolecular bands results from the hybridization of the TCNQ frontier orbitals. (a) STM topographic image of the SOMO taken at $-0.7\,\mathrm{eV}$. The dashed black lines indicate the graphene/Ru(0001) unit cell and an intermolecular band is marked in red color. (b) The electronic density distribution at the $\Gamma-$point for the first empty band of an isolated, free-standing TCNQ monolayer with the same corrugated geometry as the adsorbed monolayer reproduces the corresponding band.

drogen bond seems to be the reason for the formation of these molecular chains. However, we have shown before that the molecules are negatively charged and the attractive nature of the $\mathrm{C{\equiv}N\cdots H{-}C}$ bonds is not enough to overcome the electrostatic repulsion between the negatively charged molecules. Thus, it should be the combined effect of this attractive interaction and the partial occupation of the LUMO which give rise to the formation of spatially extended intermolecular bands that allows the molecules to delocalize the charge acquired by the graphene.

Fig. 5.6 illustrates in more detail the intermolecular band results from the hybridization of the TCNQ frontier molecular orbital. The tube-like structure marked over the STM image in Fig. 5.6a reflects the real space imaging of the occupied intermolecular band below the Fermi level, derived from the SOMO. The same occurs above the Fermi level for the SUMO. Figure 5.6b shows the electronic density distribution at the $\Gamma-$point for the band. The calculations are done for an isolated, free-standing TCNQ monolayer with the same corrugated geometry as the adsorbed monolayer and addition of 0.5 electrons/molecule. The calculations reproduce the flat bands found in the experiment and trace back the origin of these band to an anti-symmetric combination of the TCNQ LUMO. These TCNQ intermolecular states extend over whole surface.

5.2 TCNQ on graphene/Ir(111)

Deposition of a TCNQ monolayer on graphene/Ir(111) results in topographic and spectroscopic STM images different from those in TCNQ/graphene/Ru(0001). In the previous chapter, we showed how the molecules deposited on the graphene/Ir(111) surface arrange in well-ordered, compact islands and finally in a monolayer. In this section, we show the STS measurements performed to characterize the electronic structure of the TCNQ monolayer.

5.2.1 Monolayer spectroscopy

Figure 5.7 shows the $\mathrm{d}I/\mathrm{d}V$ spectra acquired on different TCNQ molecules on graphene/Ir(111). The spectra present two clear resonances and a broad region of low conductance between them. The energy position of the peaks is fairly similar for all the molecules, regardless of the relative adsorption site. We can identify the peak above the Fermi level centered at $+0.75\,\mathrm{eV}$ with the LUMO and the one below the Fermi level around $-2.75\,\mathrm{eV}$ with the HOMO. Contrary to the case of TCNQ on graphene/Ru(0001), the presence of only two peaks and the LUMO above the Fermi level suggest that there is a negligible or very small charge transfer between the molecules and graphene. Upon adsorption on a metallic surface, the molecular levels broaden and the value of the molecular gap is usually reduced due to the hybridization with the conduction electrons [77]. In this case, the graphene acts as a decoupling layer preserving the HOMO and LUMO almost intact separated by 3.5 eV.

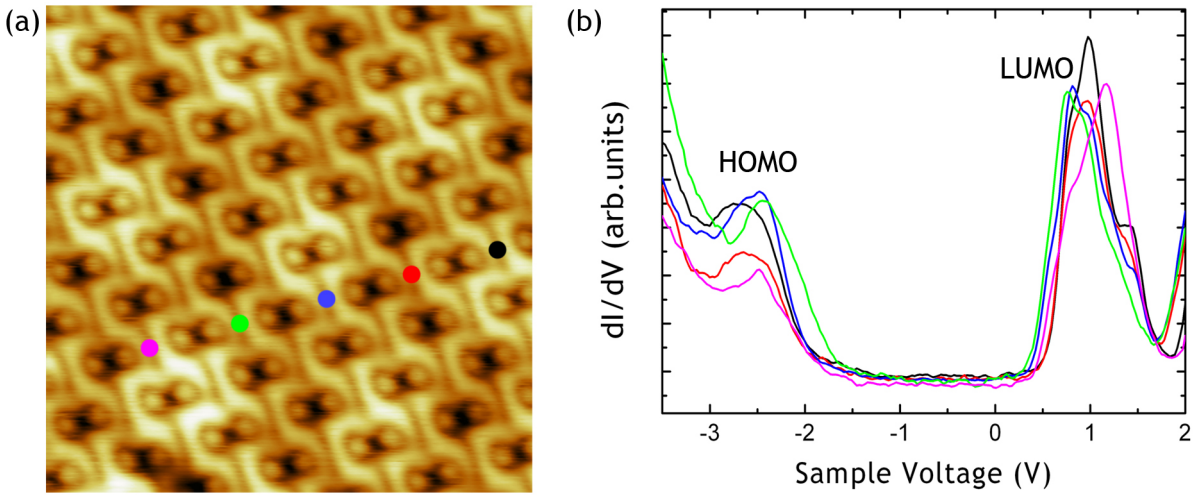

Figure 5.7: (a) STM topography ($6.5 \times 6.5\,\mathrm{nm}^2$) of a TCNQ monolayer grown on graphene/Ir(111) recorded at 4.6 K with the tunneling gap stabilized at $V_\mathrm{b} = +2\,\mathrm{V}$ and $I_\mathrm{t} = 40\,\mathrm{pA}$. (b) Individual $\mathrm{d}I/\mathrm{d}V$ curves measured on molecules located in different areas of the moiré unit cell. The color code corresponds to the dots shown in (a). The peaks correspond to the HOMO and the LUMO levels.

Taking topographic images at different bias voltages allows us to obtain intramolecular

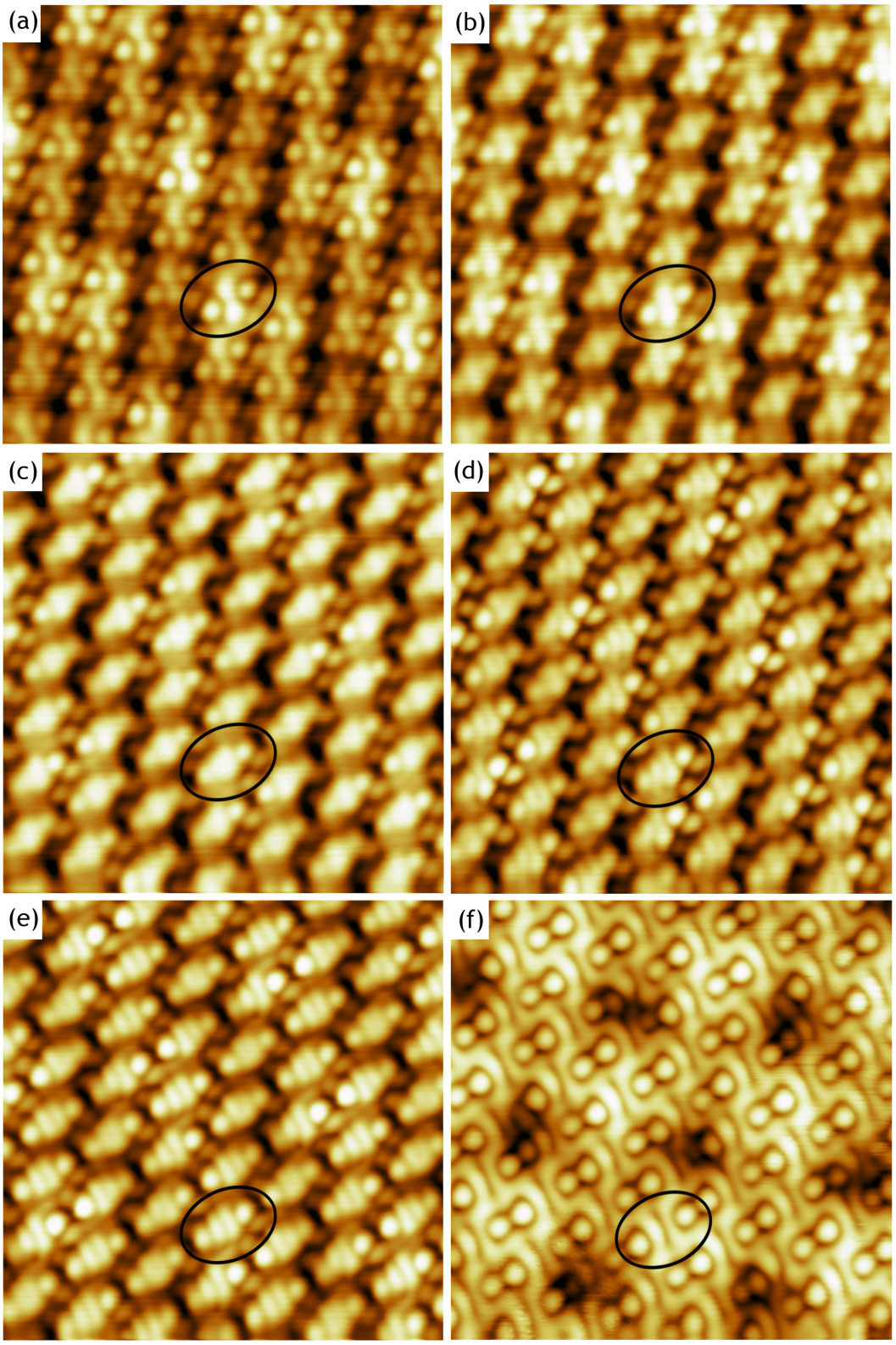

Figure 5.8: $7 \times 7\,\mathrm{nm}^2$ STM images of a TCNQ monolayer grown on graphene/Ir(111) recorded at 4.6 K with different bias voltage and $I_t = 50\,\mathrm{pA}$: (a) $V_b = -3.1\,\mathrm{V}$, (b) $V_b = -2.5\,\mathrm{V}$, (c) $V_b = -1.5\,\mathrm{V}$, (d) $V_b = -0.7\,\mathrm{V}$, (e) $V_b = +0.7\,\mathrm{V}$ and (f) $V_b = +1.5\,\mathrm{V}$. As a reference, a TCNQ molecule is encircled in each image.

resolution and identify the frontier molecular orbitals of TCNQ (see Fig. 5.8). For negative sample bias voltages, which correspond to occupied molecular orbitals, the TCNQ molecules are imaged as the HOMO calculated for a free TCNQ molecule. For positives voltages, corresponding to unoccupied molecular orbitals, the STM images resembles the calculated LUMO for isolated TCNQ with a clear node at the center of the molecule but strongly delocalized over the graphene layer. Contrary to the case of TCNQ/graphene/Ru(0001), we never image the LUMO spatial distribution in the molecules below the Fermi level. This fact confirms that the filling of the LUMO derived bands is rather small and molecules self-organize via H-bonds and no intermolecular bands.

5.3 Conclusions

In this chapter, we used spatially-resolved $\mathrm{d}I/\mathrm{d}V$ measurements in combination with DFT+D2 calculations to obtain information about the influence of graphene/Ru(0001) and graphene/Ir(111) on the TCNQ molecular electronic states.

In the case of TCNQ adsorbed in graphene/Ru(0001), it was found a considerable charge transfer from the graphene to single TCNQ molecules leading to the partial occupation of the LUMO of the neutral molecule. As result of this fact, the orbital splits in two different orbital, SOMO and SUMO. The experimental identification of the molecular orbitals was directly imaged recording spatially-resolved $\mathrm{d}I/\mathrm{d}V$ maps and confirmed by simulated $\mathrm{d}I/\mathrm{d}V$ maps. A complete analysis of the TCNQ monolayer shows still a considerable charge transfer between molecules and graphene. The formation of a complete monolayer is now understood by a combination of hydrogen bonds and a delocalization of charge across a new spatially extended intermolecular band. In this system, the role of the graphene is twofold because it isolates the TCNQ molecules from the reactive Ru(0001) surface and simultaneously allows an efficient charge transfer from the metallic substrate to the molecules. The efficient charge transfer is due to the strong interaction between the graphene and the Ru(0001) surface.

On the other hand, in the case of TCNQ on graphene/Ir(111), the weak interaction between the graphene and the Ir(111) does not allow a efficient charge transfer to the TCNQ molecules and they remain practically neutral and the electronic properties of TCNQ layer almost unaltered. In addition, we can directly image the unperturbed molecular orbitals of TCNQ and confirm that the filling of the LUMO derived bands is rather small and the intermolecular bands present in TCNQ/graphene/Ru(0001) system do not develop.

In summary, these results demonstrate the substantial influence of the interaction between graphene and the metallic substrate in the electronic properties of the TCNQ molecules adsorbed on graphene on metallic substrates. The acquired charge and the formation of intermolecular bands in the case of TCNQ molecules on graphene/Ru(0001) unlike graphene/Ir(111) will add new properties to the organic layer that will be discussed in the next chapter.

6 Magnetic structure: From Kondo effect to long-range magnetic order

The existence of unpaired electrons in organic molecules is a prerequisite to molecular magnetism, however their mutual interactions are required to develop long-range magnetic order. In this chapter, we will see that TCNQ molecules on graphene/Ru(0001) develop a magnetic moment which is revealed by a prominent Kondo resonance, and is preserved upon dimer and monolayer formation. The Kondo effect is also observed in F_4-TCNQ on graphene/Ru(0001). However, the presence of molecular bands in the TCNQ monolayer give rise to a long-magnetic order that is not developed for F_4-TCNQ case due to the repulsion between the molecules. The existence of the corresponding long-range magnetic order is detected by SP-STM at 4.6 K.

6.1 Development of a magnetic moment

As we have seen in the previous chapter, STS measurements and theoretical simulations showed that isolated TCNQ molecules deposited on graphene/Ru(0001) acquire charge from the substrate. In this section, we will demonstrate the development of a magnetic moment for organic molecules when deposited on graphene/Ru(0001). This fact will be verified by measuring the corresponding Kondo resonance with STS at low temperature.

6.1.1 Introduction to Kondo effect

Although the Kondo effect was discovered in the 1930s [78], and later explained in the 1960s [79], it has still been the subject of numerous studies. In particular, the development of LT-STM opened up the possibility to study the Kondo effect at atomic scale in single atoms [80, 81] and single molecules [82–87]. In this subsection, we describe the main features of the Kondo problem in metals and the particular case of a single magnetic impurity on a surface.

The Kondo effect in metals

The resistivity, ρ, of bulk metals should decrease when $T \rightarrow 0$ due to the scattering of electrons by phonons and others electrons until it reaches a saturated value determined by the density of defects in the metal. Far from this expected behavior, the $\rho(T)$ curves measured

in some materials present a minimum at low temperatures [78]. In 1964, J. Kondo gave the explanation for this anomalous increase of the resistivity [79]. His explanation is based on a spin-flip scattering process due to the presence of magnetic impurities in the metallic samples, and is known as the Kondo effect. In other words, the Kondo effect arises when the local spin of an impurity is screened by electrons of the metallic host. Below a characteristic temperature, the conduction electrons that surround the spin impurity electron are aligned antiferromagnetically with the impurity forming a spin screening cloud, see Fig. 6.1, and leading to an increase of the resistance.

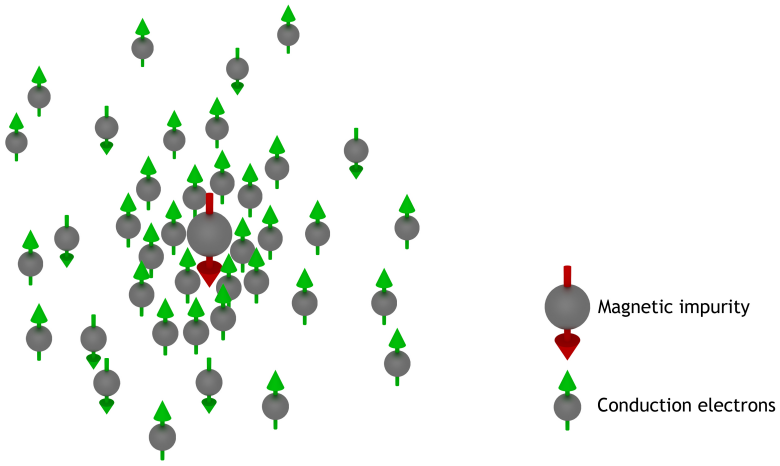

Figure 6.1: Kondo effect. Spin screening cloud surrounded the local impurity.

To explain the behavior of these systems, P. W. Anderson proposed a model in 1961 for a single magnetic impurity diluted in a metal [88]. The model considers the hybridization between the conduction electrons of the metal and the unpaired electron state with $s = \frac{1}{2}$ of the impurity, dismissing all the others electronic states of the impurity. The Hamiltonian that describes the behavior of this single magnetic impurity coupled to a conduction band of electrons is given by [88]:

$$H = \sum_{\sigma} \varepsilon_d d_\sigma^\dagger d_\sigma + \sum_{k\sigma} \varepsilon(k) c_{k\sigma}^\dagger c_{k\sigma} + U d_\uparrow^\dagger d_\uparrow d_\downarrow^\dagger d_\downarrow + \sum_{k\sigma} \left(V_{k\sigma} d_\sigma^\dagger c_{k\sigma} + V_{k\sigma}^* c_{k\sigma}^\dagger d_\sigma \right). \tag{6.1}$$

The terms, from left to right, describe: the impurity state with energy ε_d, the conduction electrons $\varepsilon(k)$, the on-site Coulomb repulsion U, and the hybridization between the local spin and the conduction electrons. The operator $d_\sigma^\dagger$ (d_σ) creates (annihilates) an electron of spin σ ($\uparrow$ *or* $\downarrow$) on the localized impurity, while $c_{k\sigma}^\dagger$ ($c_{k\sigma}$) creates (annihilates) and electron of spin σ and momentum k in the conduction band. The impurity is described in the most simple way as a non-degenerate orbital which has, at most, double occupancy with spin $\uparrow$ and a spin $\downarrow$ electron separated by the Coulomb repulsion energy U [88], see Fig. 6.2. The

last term of the Hamiltonian takes into account the interactions between the impurity level and the conduction electrons, where $V_{k\sigma}$ are the tunneling matrix elements. Excluding thermal excitations, a simple description of the Anderson impurity model allows two possible excitations:

- A conduction electron with energy $\varepsilon(k)$ and spin $\downarrow$ can jump to the unoccupied impurity state forming a virtual excitation. The impurity is now doubly occupied. Then, the original electron of the impurity of spin $\uparrow$ tunnels out and the other electron decays into this state with the spin $\downarrow$.
- Another possible virtual state corresponds to the excitation of the electron of the impurity with spin $\uparrow$ into a state of momentum k while another electron with opposite spin decays into the now unoccupied localized state.

While classically these spin flip processes are forbidden due to the cost in energy giving by $\varepsilon_d - \varepsilon_k + U$ and $\varepsilon_d - \varepsilon_k$. In quantum mechanics, exists a short time, around $h/|\varepsilon_d|$ given by the uncertainty principle, in which these excitations can take place. Thus, the conduction electrons spend some time in the region of the impurity, but it cannot be considered a bound state. These intermediate virtual states induce a narrow resonance in the conduction band density of states at the Fermi level where the process occurs. The width Δ of this resonance is defined by $\Delta = \pi|V_{kd}|^2\rho(\varepsilon)$ where $\rho(\varepsilon)$ is the density of states of the metal [89, 90].

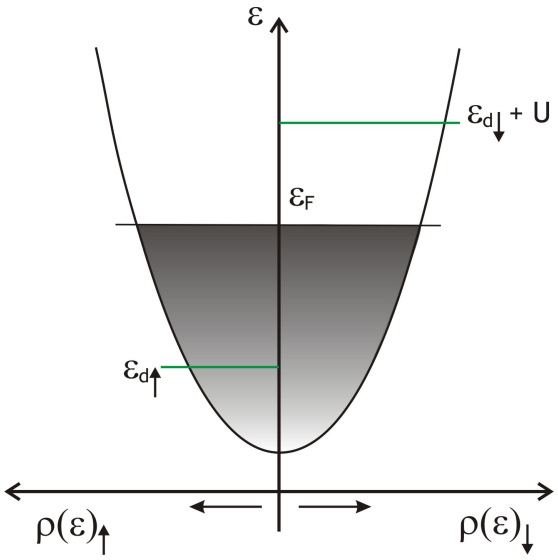

Figure 6.2: Energy levels, $\varepsilon_{d\uparrow}$ and $\varepsilon_{d\downarrow} + U$, for a magnetic impurity embedded in a conduction band of a metal in the Anderson impurity model. Image adapted from [88].

In summary, the Anderson impurity model gives a simple explanation for the bounded mechanism of the impurity with the conduction band of the host metal. The Kondo Hamil-

tonian is an approximation of the Anderson Hamiltonian and can be obtained from it performing a Schrieffer-Wolff transformation [90, 91]:

$$H \simeq \sum_{k\sigma} \varepsilon(k) c^{\dagger}_{k\sigma} c_{k\sigma} + \sum_{kk'} J_{kk'} \mathbf{s}_{kk'} \cdot \mathbf{S}_d \,, \tag{6.2}$$

where the spin of the impurity is $\mathbf{S}_d$ and $\mathbf{s}_{kk'}$ represents the spin of the conduction electrons and $J_{kk'}$ the coupling streght between the impurity states and the conduction electrons. Taking into account that the process occurs at Fermi level, for k and $k' \simeq k_F$, the coupling $J_{kk'}$ is given by:

$$J_{kk_F} \equiv J = \frac{2\Delta}{\pi} \left(\frac{1}{\varepsilon_d} - \frac{1}{\varepsilon_d + U} \right) < 0. \tag{6.3}$$

As expected, the coupling is antiferromagnetic. Therefore, the spin exchange interaction between the impurity and the conduction electron is given by the so called Kondo term:

$$H_K = J \mathbf{s}(r) \mathbf{S}. \tag{6.4}$$

The resistivity and the impurity susceptibility of the system can be derived from this Hamiltonian using second order perturbation theory. Although, the Kondo model describes the behavior of the anomalous resistivity in these systems above certain temperature, known as Kondo temperature T_K, below T_K there is a divergence due to the presence of a logarithmic term. The characteristic energy scale in which this divergence becomes important is [89]:

$$k_B T_K \sim D e^{-1/2J\rho_0}, \tag{6.5}$$

where ρ_0 the density of states and D is the width of the conduction band. Substituting the exchange coupling J calculated by Schrieffer and Wolff [91] the Kondo temperature can be calculated as follow [90]:

$$T_k = \frac{1}{2\pi} \left(\frac{2\Delta U}{\pi} \right)^{1/2} exp \left[\frac{\varepsilon_d(\varepsilon_d + U)}{2\Delta U} \right]. \tag{6.6}$$

To obtain a complete description of the resistivity in these systems for $T \ll T_k$ a renormalization group approach is necessary [89].

The Kondo effect and the STM

Taking advantage of the atomic-scale spatial resolution and high-resolution spectroscopy measurements, the LT-STM seems to be the perfect tool to study the Kondo impurities at surfaces. In late 1990s, several groups performed the firsts experiments where single magnetic

adatoms were deposited on non magnetic surfaces, e.g., Ce on Ag(111) [80] or Co on Au(111) [81]. A simple explanation for the tunneling process of a single magnetic adatom on a metal surface is given by the Anderson impurity model. In this situation, the electrons from the STM tip have two possible channels to tunnel into the sample. They can tunnel directly into the empty states of the sample or indirectly via a spin-flip process into the localized impurity state. Figure 6.3a shows the latter case, where the electron in the single occupied impurity state located below the Fermi level at ε_d with spin $\uparrow$ can be excited into an unoccupied state, forming a virtual state. Then, an electron from the tip with energy ε_F and spin $\downarrow$ can tunnel into the impurity state. This spin exchange produces a resonance in the energy spectrum due to the interference of the localized state and the conduction electrons of the metal, known as Kondo resonance Fig. 6.3b.

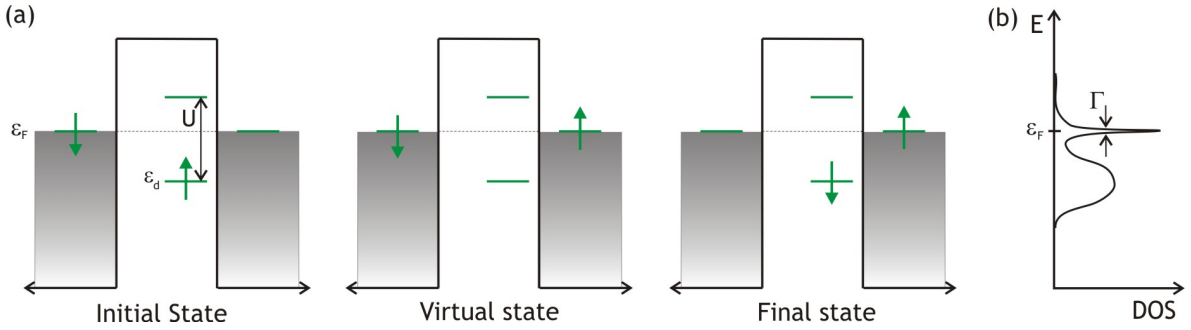

Figure 6.3: Anderson impurity model and the Kondo effect. (a) The impurity level is located at ε_d below the Fermi level ε_F of the continuum states of the metal. Adding an electron to the impurity costs an extra energy giving by the Coulomb repulsion U. In a time scale given by the Heisenberg uncertainly principle, a virtual state can be created when the spin up electron of the impurity tunnel out to the continuum states of the metal. It will be replaced by another electron from the tip with spin down. (b) This spin flip process leads to the appearance of a resonance at Fermi level, called Kondo resonance. Image adapted from [92].

Therefore, when Kondo screening exists, the STS spectra present a resonance at ε_F spatially localized at the magnetic impurity. This resonance is the result of the quantum interference of the discrete state of the impurity and the continuum of the conduction electrons in the metal and can be described by the Fano equation [93], as was demonstrated by V. Madhavan *et al.* [81]. In this context, the tunneling conductance is given by:

$$\frac{\mathrm{d}I}{\mathrm{d}V} \propto \frac{(\varepsilon + q)}{1 + \varepsilon}, \qquad \varepsilon = \frac{eV - \varepsilon_0}{\Gamma}, \tag{6.7}$$

where Γ is the half-width at half-maximum of the resonance, q is a parameter known as the form factor, and ε_0 is the energy shift of the resonance from the Fermi level. The form factor gives the ratio between the indirect and direct tunneling processes at the resonance energy. A set of values for q are represented in Fig.6.4. For $q = 0$ the curve results in a Lorentzian

dip and for large q value the curve results in a Loretzian peak. The intermediate value of q leads to asymmetric curves. Physically, large values of q mean that the indirect tunneling through the impurity dominates. This is usually the case for organic molecules interacting weakly with the substrate or magnetic adatoms on insulating layers. Some examples are Mn adatoms deposited on aluminum oxide islands [94], CoPc on Au(111) [82], TCNQ-TFF mix on Au(111) [86], V-TCNE complexes on Ag(111) [95] or MnPc on Pb(111) islands [96]. Contrary, low values of q imply that the tip is more strongly coupled to the conduction electrons of the metallic host and the direct tunneling channel to the substrate dominates. This is the case for impurities interacting strongly with the substrate, such as transition or rare earth atoms [80, 81], TBrPP-Co molecules on Cu(111) [83, 97], oxygen molecules on Au(111) [98] or on-top FePc on Au(111) [84].

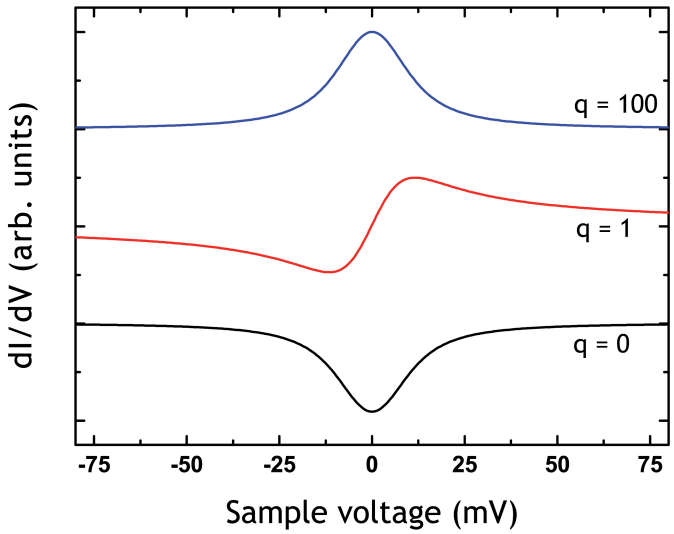

Figure 6.4: Set of simulated Fano resonances at E_F with $\Gamma = 5\,\text{meV}$ for different q parameters. At $q = 0$ the coupling between the tip and the discrete atomic orbital is weak and leads to a Lorentzian dip. An intermediate coupling is representing for $q = 1$ resulting in a asymmetric curve. Finally, the case $q = 100$ represent a strong coupling and a Lorentzian peak is detected.

In general, due to the reduced coupling strength between the impurity and the conduction electrons on a metallic surface, T_k is usually lower for a surface impurity than that in the bulk system. T_k in bulk materials is given by the expression 6.6. In the tunneling spectroscopy experiments, the T_K can be extract from the full width at half maximum (FWHM) 2Γ of the Kondo resonance given by [99, 100]:

$$2\Gamma = \sqrt{(\alpha k_B T)^2 + (2k_B T_k)^2}. \tag{6.8}$$

System	T_K	Reference
Co impurities on bulk Cu	500 K	[101]
d-CoPc/Au(111)	208 K	[82]
TBrPP-Co/Cu(111)	105 – 170 K	[83]
Co/Cu(100)	88 K	[102]
Co/Au(111)	70 K	[81]
Co/Cu(111)	53 K	[102]
Co on epitaxial graphene	15 – 17 K	[103, 104]
$Co/Cu_2N/Cu(100)$	2.6 K	[105]

Table 6.1: Kondo temperature for Co impurities in different systems.

Following this expression, we can see that for a Kondo effect, the width of the resonance grows linearly with the temperature ($\Gamma \sim T$) for $T \gg T_K$ and saturates ($\Gamma = k_B T_K$) for $T \ll T_K$. Then, T_k can be calculated fitting the experimental width of the Kondo resonance at different temperatures to the expression 6.8, where α is a constant which depends on the system. As an illustration, the Table 6.1 shows a collection of Kondo temperatures for Co impurities in different systems. The highest T_K is for the case of Co impurities on bulk Cu. As expected, in the case of Co adatoms on metallic surfaces the Kondo temperatures are lower because the number of metallic neighbors is reduced and the hybridization between the impurity and the host metal decreases. In the particular cases of Co on Cu(100), Au(111) and Cu(111) the Kondo temperatures are 88 K, 70 K and 53 K respectively. The small differences can be understood considering that the hybridization between the *d*-orbital of the Co atoms and the substrate decreases in the following order Cu(100) > Au(111) > Cu(111) and, consequently, increasing T_K in the series. A peculiar case is the dehydrogenated cobalt phthalocyanine (d-CoPc) molecule adsorbed on an Au(111) surface. It presents a quite high T_K in comparison with Co adatom on Au(111). These results reveal the importance of the chemical environment on the Kondo effect. When the CoPc molecule is deposited on Au(111), the magnetic moment of the molecule is completely quenched by the the interaction with the substrate and no Kondo resonance appears. However, inducing a dehydrogenation by the STM tip, the Co atoms of the molecule shifts upwards with respect to the substrate and a Kondo effect is resorted. The effect of the organic ligands on the Kondo temperature is also clear in the case of molecular self-assembly TBrPP-Co on Cu(111). This system presents also a high T_k which decreases when the number of TBrPP-Co molecules is reduced. The Kondo effect has also been demonstrated in the particular case of a Co impurity in graphene epitaxially growth on SiC substrate. In this system the graphene layer is n-doped and leads to an exotic Kondo ground state that depends on the Co adsorption site. The last example corresponds to Co adatoms decoupled from a Cu(100) surface by a monolayer of copper nitride

(Cu_2N). This decoupling produces a small hybridization with the conduction electrons and therefore a small T_K of 2.6 K. An evidence of this small interaction is the observation in the STS of a sharp Kondo peak on the Co atoms, as expected, for a system where the indirect tunneling dominates.

6.1.2 Kondo effect in TCNQ on graphene/Ru(0001)

In the preceding chapter we showed the localization of an electron into the TCNQ orbital derived from the LUMO. Here, we aim to understand how the presence of this electron determines the magnetic properties of the system.

Single molecules

As discussed previously, single TCNQ molecules on graphene/Ru(0001) present two spectral features close to the Fermi level in the STS, one below (SOMO) and another one above it (SUMO). The origin of these features is the splitting of the LUMO of the neutral molecule due to the transfer of one electron to the TCNQ molecule from the graphene/Ru(0001) surface. To shed some light on the character of these orbitals, spin polarized calculations were performed by D. Stradi [36]. Firstly, spin polarized gas-phase calculations for isolated TCNQ was done and revealed, as expected, that neutral TCNQ has not a magnetic moment. Nevertheless, the spin polarized Projected Density of States (PDOS) for a single TCNQ molecule on its optimized adsorption geometry on graphene/Ru(0001) shows that the LUMO of the neutral molecule is now partially occupied and splits into a more than half filled spin-up SOMO and a more than half empty spin-down SUMO, see Fig. 6.5b. The width and filling ratios of the orbitals depend on the molecule-substrate interaction. A proof of this fact is that the width of the orbitals is reduced and the spin asymmetry is increased when the TCNQ is separated from the substrate in the calculations or, in other words, when the interaction is weaker [106]. These results are in agreement with the non spin polarized experimental data of Sec. 5.1.

The different electron occupancy of SOMO and SUMO is the necessary condition to have a non-zero magnetic moment in the molecule. The calculated magnetic moment is 0.4 μ_B, and the spin density distribution across the TCNQ molecule is showed in Fig. 6.5a. The yellow (green) color indicates a positive (negative) spin density which is exactly distributed across the LUMO orbital.

As mentioned in the introduction of this section, an experimental proof of the presence of unpaired electron in a single molecule or adatom adsorbed in a non-magnetic surface is the appearance of the Kondo effect. Figure 6.6 shows the STS experiments performed on a single TCNQ molecule adsorbed on graphene/Ru(0001) close to the Fermi level. The $\mathrm{d}I/\mathrm{d}V$ signal was acquired by means of lock-in techniques by adding AC component to the bias voltage ($V_{\mathrm{mod}} = 8.5\,\mathrm{mV}$ RMS and $\nu = 703\,\mathrm{Hz}$) while DC component of the bias voltage was ramped linearly and the feedback was switched off. The $\mathrm{d}I/\mathrm{d}V$ spectra measured with the STM tip

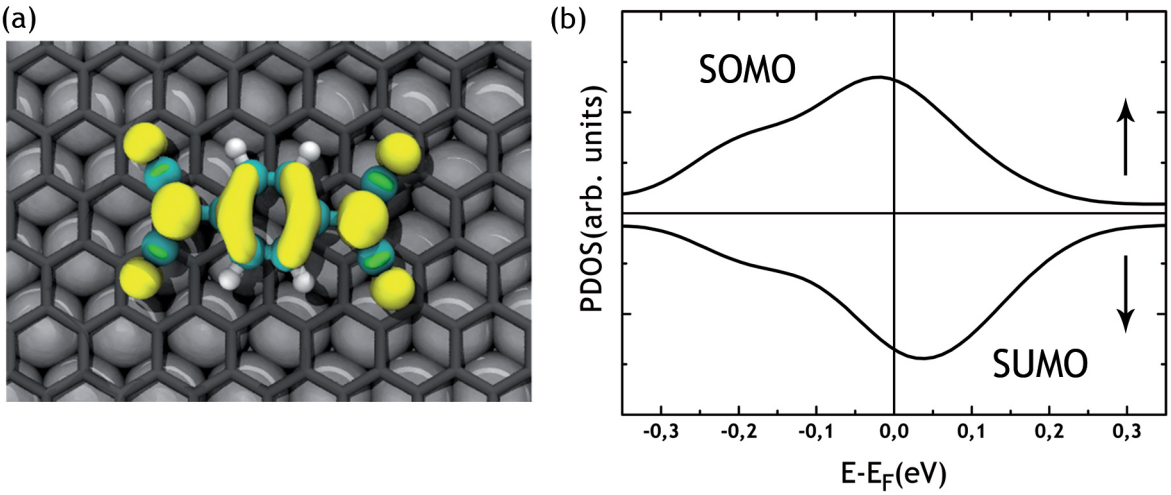

Figure 6.5: (a) Calculated spin-density distribution for a single TCNQ molecule adsorbed on graphene/Ru(0001). Yellow and green indicate positive and negative spin densities, respectively. (b) Calculated spin-polarized PDOS over s and p orbitals for the same molecule [36, 106].

held on different locations in the TCNQ molecule show a prominent peak which is absent in the graphene surface (Fig. 6.6d). We identify it as a Kondo resonance due to the interplay between the conduction electrons of graphene/Ru(0001) and the magnetic moment associated with the TCNQ molecules. According to the calculations, the Kondo scenario raises because the transfer of a second electron from the graphene/Ru(0001) substrate to the magnetic TCNQ radical anion is forbidden by coulomb repulsion that makes the corresponding electron affinity for the second electron being well above the Fermi level of graphene/Ru(0001) [106].

The intensity of the Kondo peak exhibits a strong dependence on the STM tip location within the TCNQ molecules. As an illustration, the blue and red spectra were fitted to the Fano expression given by eq. 6.7. The signal that we measured with the lock-in is broadened by the temperature and the modulation voltage. Then, the curves have to be convoluted with the first derivative of the Fermi-Dirac distribution and the lock-in modulation. The resulting fitting parameters are $\Gamma = 5 \pm 1\,\mathrm{mV}$, $\varepsilon_0 = 1.2\,\mathrm{meV}$ and $q = 40$ for the blue curve and $\Gamma = 5 \pm 1\,\mathrm{mV}$, $\varepsilon_0 = 1.2\,\mathrm{meV}$ and $q = 10$ for the red one. These large values of q are not surprising taking into account the weak interaction between the TCNQ and the substrate. The experiments have been performed at 4.6 K and therefore, we expect to be in the $T \ll T_K$ regime. In this situation an estimation of the Kondo temperature from the width of the peak ($T_K = \Gamma/k_B$) can be done. The estimated Kondo temperature is 58 K which is on the range expected for a weak interacting molecule. Nevertheless, a complete analysis of the temperature dependence of the resonance is necessary for a demonstration of a Kondo effect and to obtain an accurate value of T_K. For single molecules, these experiments cannot be performed

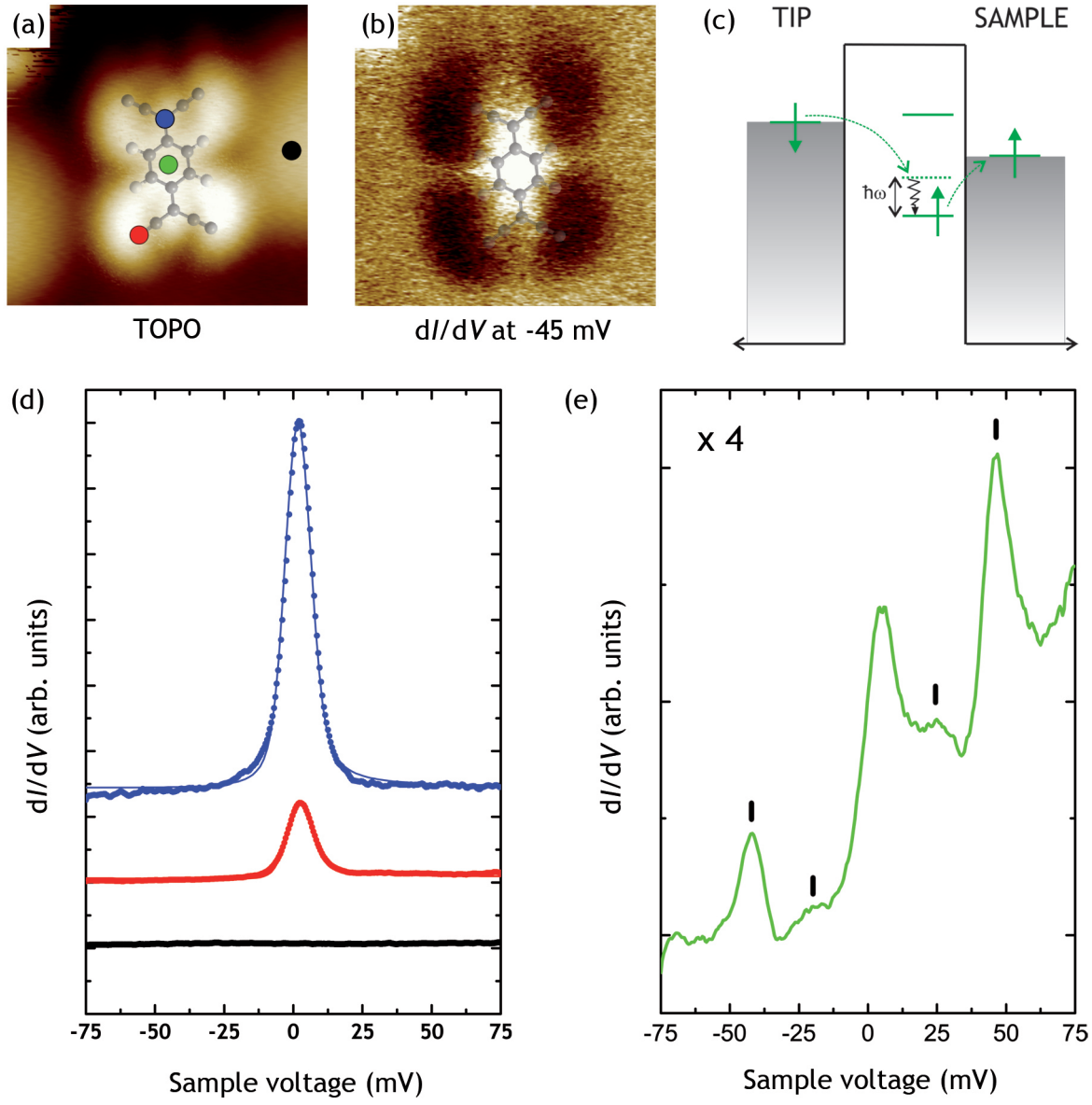

Figure 6.6: Inelastic Kondo effect. (a) Topographic STM image ($2.4 \times 2.4\,\mathrm{nm}$, $V_\mathrm{b} = -0.1\,\mathrm{V}$, $I_\mathrm{t} = 30\,\mathrm{pA}$) of a TCNQ molecule on graphene/Ru(0001) with a TCNQ model superimposed. The color circles indicate the spatial location where the spectra shown in (c) and (d) have been recorded. (b) $\mathrm{d}I/\mathrm{d}V$ map at $V_\mathrm{b} = -50\,\mathrm{mV}$ of the image (a) with a TCNQ model superimposed. (c) Sketch of the inelastic Kondo effect where the spin-flip process is mediated by the excitation of a vibrational mode of the TCNQ. (d) $\mathrm{d}I/\mathrm{d}V$ spectra measured with the STM tip held on graphene and on different locations in the TCNQ molecule where Kondo resonance is observed. (e) $\mathrm{d}I/\mathrm{d}V$ spectrum measured with the STM tip held on the central ring of the TCNQ molecule.

due to the mobility of the molecules when the temperature increases. This analysis will be done later for higher TCNQ coverages.

Besides, inelastic Kondo features are observed in the spectrum measured with the STM tip held on the center of the molecule (Fig. 6.6e). At this position, the Kondo resonance almost disappears and two side bands around $\pm 45\,\mathrm{mV}$ and $\pm 17\,\mathrm{mV}$ come up. The origin of these peaks is an interplane molecular vibration in the central ring and a C-C≡N bending of the TCNQ molecule [107, 108] respectively, which are strongly coupled to the TCNQ SOMO. The $\mathrm{d}I/\mathrm{d}V$ map of Fig. 6.6b shows the spatial distribution of the peak at $-45\,\mathrm{mV}$. The maximum of the signal corresponds exactly to the central area of the TCNQ molecule where the excitation is produced. The observation of the C-C≡N bending at $\pm 17\,\mathrm{meV}$ is more complicated because it implies to acquire a $\mathrm{d}I/\mathrm{d}V$ map at low energy and in location within the TCNQ molecule where the Kondo resonance begins to appear.

The inelastic Kondo effect was predicted in quantum dots coupled to vibrational modes [109] and has also been observed in electron transport studies through C_{60} molecule in the Kondo regime, using a mechanically controllable break junction [110]. A schematic representation of the process is shown in Fig. 6.6c. For a bias voltage higher than a quantum vibrational mode of the molecule, a new channel is opened. Similar to the case at zero bias, the electron of the impurity can tunnel into the sample states. Then, an electron with opposite spin can tunnel through the molecule, exciting its internal states and decaying in the impurity ground state. The result is the excitation of the vibrational mode of the molecule in addition to a spin-flip process. The effect in the DOS is the appearance of two symmetric peaks at the vibrational mode energies superimposed to the classic steps of the ordinary inelastic tunneling processes (Fig. 2.2). Similar results were reported for TCNQ-TFF layers on Au(111) [86]. In this case, one electron is donated from TTF to TCNQ giving rise to a Kondo effect due to the interaction between the unpaired electron from TCNQ and the conduction electrons of the gold substrate with a Kondo temperature of 26 K. The intensity of the Kondo peak also exhibits a dependence on the STM tip location within the TCNQ molecules being maximum at the ending cyano groups and minimum in the middle of the TCNQ molecule, where extra side peaks at $\pm 41\,\mathrm{mV}$ appears.

It has been discussed at the beginning of this chapter thath the Kondo effect strongly depends on the hybridization between the impurity state and the host electrons. It might be expected, then, a different width and intensity of the Kondo resonance depending on the TCNQ adsorption location and maybe, no Kondo resonance for some of them. Figure 6.7 shows the $\mathrm{d}I/\mathrm{d}V$ spectra for two TCNQ molecules adsorbed on different configurations within the moiré unit cell. It has been shown in preceding chapters that the electronic modulation of the graphene/Ru(0001) surface forces the TCNQ molecules to adsorb in the low areas of the moiré pattern. In particular, at low coverages, we can distinguish among three different TCNQ adsorption sites within the moiré unit cell: *fcc*, *hcp* and bridge (the region between the *fcc* and *hcp* areas). Experimentally, we can identify the *fcc* areas because this

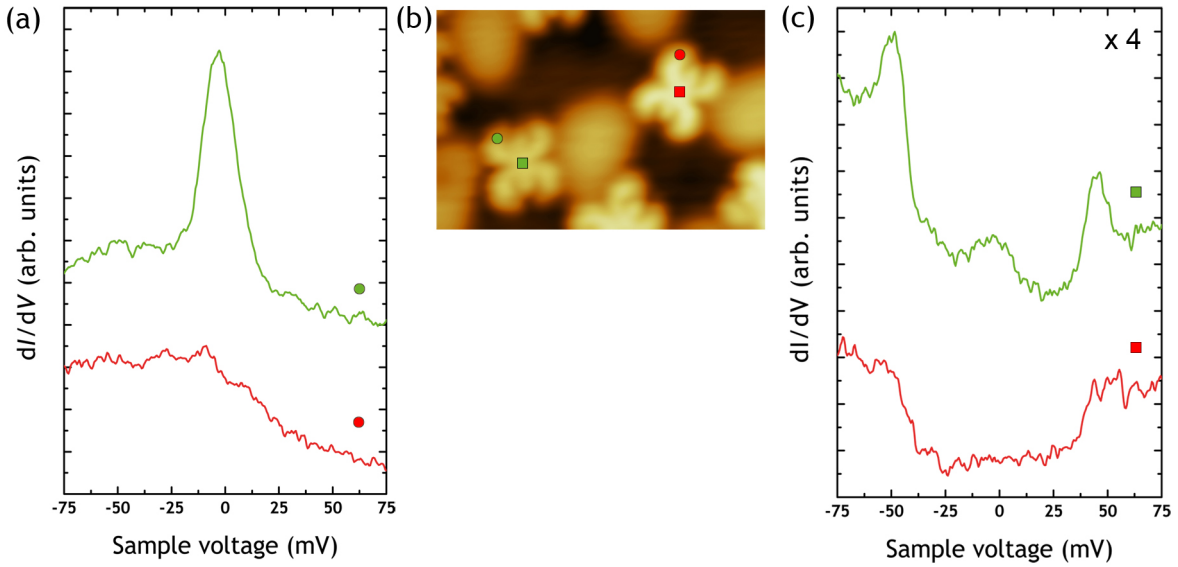

Figure 6.7: (a) $\mathrm{d}I/\mathrm{d}V$ spectra measured on the cyano group of the TCNQ molecules marked with a red and green circles on (b). (b) Topographic STM image ($6 \times 4\,\mathrm{nm}^2$,$V_\mathrm{b} = -0.1\,\mathrm{V}$, $I_\mathrm{t} = 30\,\mathrm{pA}$). (c) $\mathrm{d}I/\mathrm{d}V$ spectra measured on the center of the TCNQ molecules marked with a red and green squares on (b).

half of the unit cell is a little bit brighter in the STM images at negative bias voltages than *hcp* areas, as it was discussed previously. In the STM image of Fig. 6.7b, one molecule is adsorbed on a *fcc* position (red) and another on a bridge position (green). The green spectrum presents a sharp Kondo resonance and the characteristic features of an inelastic Kondo described before. However in the case of the red spectrum, the Kondo resonance is absented and instead of the Kondo vibrational peaks, two symmetric steps appear at $\pm 45\,\mathrm{meV}$. These results are an unequivocal proof that the origin of the features at $\pm 45\,\mathrm{meV}$, in both molecules, is the excitation of a vibrational mode of TCNQ. For the peaks at $\pm 17\,\mathrm{meV}$ it is necessary to acquire the more sensitive $\mathrm{d}^2I/\mathrm{d}V^2$ spectra to further confirm their existence in the red spectra.

In order to get some insight on these results, a compilation of calculated data of a single TCNQ molecule adsorbed on the different configurations is shown in Table 6.2 [36]. Although, the charge transfer is practically the same in all configurations, the calculated magnetic moment varies between $0.09 - 0.86\,\mu_B$. These important changes in μ, in relatively small distances, leads to a variations of the Kondo intensity and width at different locations of the molecule. Figure 6.8 shows the $\mathrm{d}I/\mathrm{d}V$ measurements performed on different TCNQ molecules on graphene/Ru(0001). The conductance $\mathrm{d}I/\mathrm{d}V$ spectra of Fig. 6.8c were measured on graphene (black curve) and on the cyano groups of the numerated TCNQ molecules of Fig. 6.8a. As it can be seen, not all the molecules present a Kondo resonance. The dependence of the Kondo peak intensity with the adsorption site is clearly seen in the

	Adsorption Energy (eV)	μ (μ_B)	Charge state (n°e$^-$)
fcc	−2.53	0.09	−1.02
bridge	−2.47	0.36	−0.98
hcp	−2.37	0.86	−0.98

Table 6.2: Data for a single TCNQ molecule on different adsorption site within graphene/Ru(0001) moiré unit cell. The adsorption energy was calculated with DFT including dispersion correction (DFT+D2) and the charge state with Bader analysis of the electronic density [36]

Kondo map of Fig. 6.8b. The Kondo map corresponds to a $\mathrm{d}I/\mathrm{d}V$ map at 1 mV simultaneously acquired with the topographic image. In this area, there are four TCNQ molecules adsorbed in different adsorption sites within the moiré unit cell. The molecule 1 is adsorbed in the *fcc* area of the moiré marked in the topographic image with a red triangle. Molecule 4 is adsorbed in an equivalent position. Accordingly, the molecule 3 is adsorbed in the *hcp* area (blue triangle) and the molecule 2 in a bridge position (between *fcc* and *hcp* area). The Kondo map clearly reveals that only molecules 2 and 3 present a Kondo signal being more intense in molecule 3. On the other hand, the molecules 1 and 4 appear dark because no Kondo resonance appear on these molecules. It is worth noting that the Kondo signal is spatially distributed on SOMO of the molecule, where the unpaired electron is located. We fitted the $\mathrm{d}I/\mathrm{d}V$ spectra for the molecules 2 and 3 to a Fano line shape obtaining a resonance width of $\Gamma = 26 \pm 1$ mV and $\Gamma = 7 \pm 1$ mV, respectively. As expected, the molecule 3 presents the most intense Kondo resonance which correspond to the largest magnetic moment in the calculations. On the other hand, the TCNQ molecules adsorbed on *fcc* areas present a negligible magnetic moment, in agreement with our experimental results, in which no Kondo resonance is observed. The molecules in bridge position exhibit an intermediate value of the magnetic moment and they always present a resonance on the $\mathrm{d}I/\mathrm{d}V$ spectra, as it can be seen in Fig. 6.8.

The above mentioned results can be understood as consequence of the difference in electronic structure of the graphene-Ru interlayer depending on the position in the moiré unit cell. First-principle calculations reveal that the graphene layer induces the confinement of an electron resonance of the Ru(0001) surface [37]. The different graphene-Ru stacking between the *fcc* and *hcp* areas produce a different extension of the resonance into the ruthenium bulk. The role of the graphene layer on the Kondo effect is henceforth to provide one electron to the TCNQ molecule and modulate the hybridization between this electron and the Ru conduction electron [36].

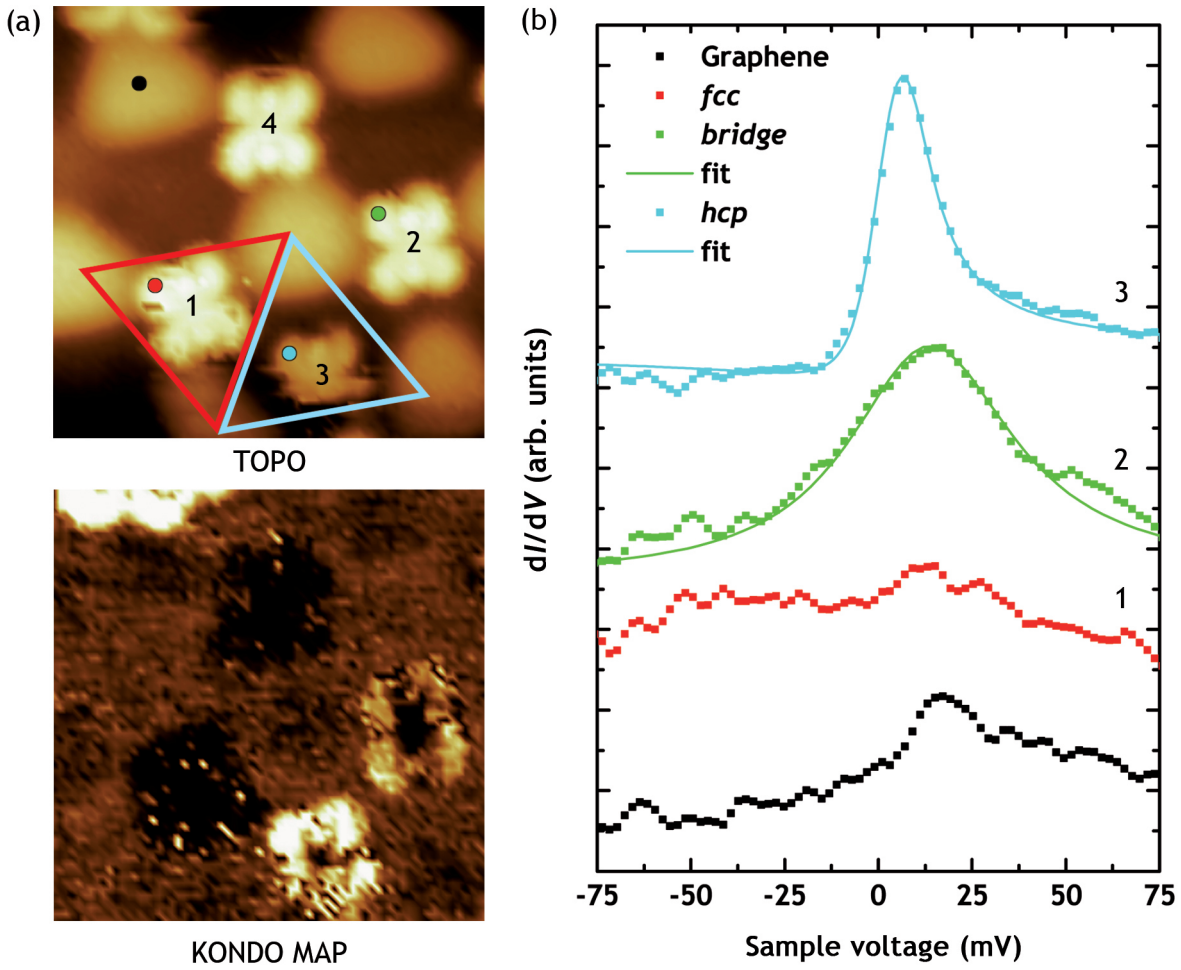

Figure 6.8: (a) Topographic STM image ($5.5 \times 5.5\,\mathrm{nm}$) of TCNQ molecules on graphene/Ru(0001) acquired at 4.6 K and tunneling parameters $V_\mathrm{b} = -0.1\,\mathrm{V}$, $I_\mathrm{t} = 30\,\mathrm{pA}$. Blue and red triangles indicate the *hcp* and *fcc* regions, respectively. The Kondo map corresponds to a $\mathrm{d}I/\mathrm{d}V$ map at 1 mV ($V_\mathrm{mod} = 8.5\,\mathrm{mV}$ RMS and $\nu = 703\,\mathrm{Hz}$) taken simultaneously with the topographic image. (b) $\mathrm{d}I/\mathrm{d}V$ spectra measured on graphene (black curve) and on the cyano groups of the numerated TCNQ molecules of (a). The solid lines represent the Fano fitting to the experimental data (Blue: $q = 4$, $\varepsilon_0 = 4\,\mathrm{mV}$ and $\Gamma = 7 \pm 1\,\mathrm{mV}$. Green: $q = 30$, $\varepsilon_0 = 13\,\mathrm{mV}$ and $\Gamma = 26 \pm 1\,\mathrm{mV}$).

Molecular chains

The next question is what happens when the TCNQ coverage is increased. In order to clarify this issue, similar experiments and calculations than for a single TCNQ molecule were performed on the dimer and molecular chains. Experimentally, we see that the Kondo resonance is preserved in the dimer and short molecular chains. In the STM image of Fig. 6.9a a monomer, a dimer and a trimer were measured simultaneously. The Kondo map of Fig. 6.9b shows that the Kondo signal decreases from the monomer to the trimer. Notice that at least

one of the molecules in the dimer and trimer is adsorbed on a bridge position.

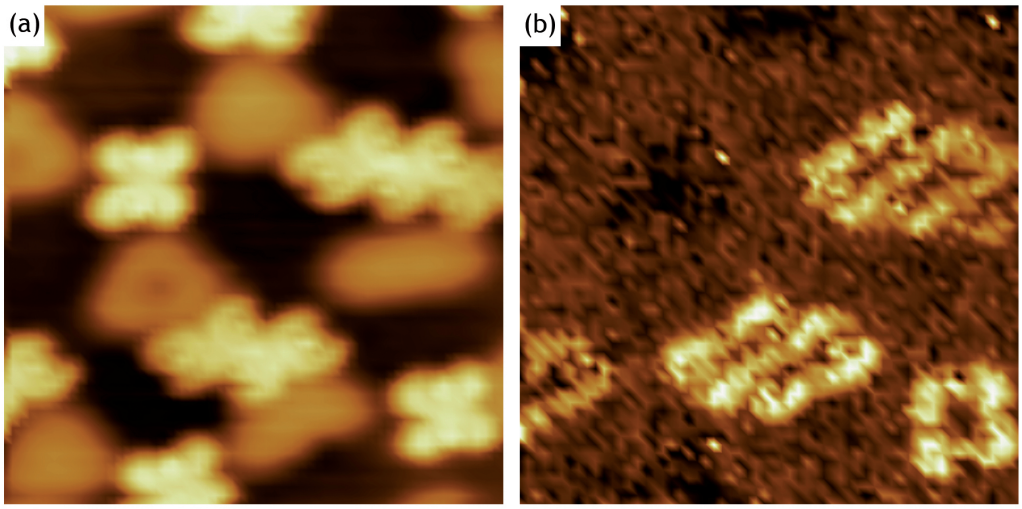

Figure 6.9: (a) Topographic STM image (6.2×6.2 nm) of TCNQ molecules on graphene/Ru(0001) acquired at 4.6 K and tunneling parameters $V_b = -0.1$ V, $I_t = 30$ pA, where a monomer, a dimer and a trimer are visible. (b) Kondo map (dI/dV map at 1 mV) measured simultaneously with the topographic image.

The calculations show that in the case of the TCNQ dimer, it takes two electron from graphene/Ru(0001), one per molecule, and leads to the electronic density distribution shown in Fig. 6.10c. The extra electrons delocalized across the new intermolecular orbital visualized in the STM images and in the simulated image of the TCNQ dimer, see Fig. 6.10a and 6.10b respectively.

The most stable configuration for the doubly charge dimer in the gas phase corresponds to the spin of the two electrons aligned parallel to each other, as can be concluded from the calculated energies of the close-shell singlet and the open-shell triplet. The open-shell triplet is energetically more stable than close-shell singlet by 160 meV [106]. Hence, the spin polarized PDOS of Fig. 6.10d shows a splitting of the LUMO in a spin-up/spin-down components and that is why the dimer develops a net magnetic moment of 1.0 μ_B that is almost doubles that of the isolated molecules. In summary, the delocalization of the added electrons along the intermolecular orbital allows the spin electron to be as separated as possible, and in virtue of a sort of giant intermolecular Hund's rule, rendering the parallel alignment energetically favorable.

As we discuss in previous subsection 6.1.1, The Kondo temperature is related to the density of the conducting electrons, ρ_0, and the exchange coupling, J (eq. 6.5). Therefore, the differences on T_K are caused by a different spin-electron coupling between the molecules and the substrate. The subtle balance between the intermolecular interaction, the coupling to the substrate, and the inhomogeneities in the density of the states of the substrate will

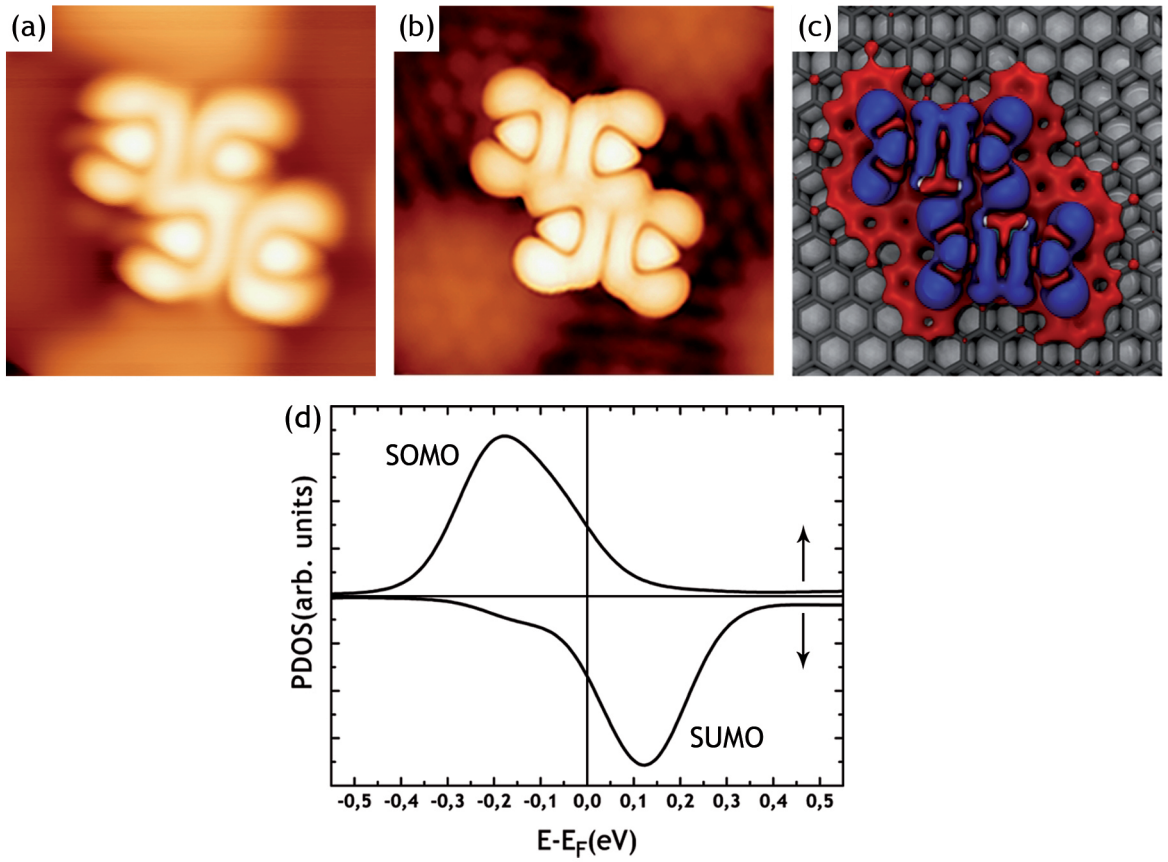

Figure 6.10: (a) $3 \times 3\,\mathrm{nm}^2$ STM image acquired at 4.6 K with $V_b = -2\,\mathrm{V}$ and $I_t = 20\,\mathrm{pA}$. (b) Simulated STM image of the TCNQ dimer obtained integrating the density of states at energies around the SOMO energy. (d) Isocountour surfaces (isocountour value = 0.001 eV/Å) of electronic density redistribution upon adsorption of TCNQ dimer on graphene/Ru(0001). Blue (red) areas indicate electron density accumulation (depletion). (e) Spin-polarized PDOS over *s* and *p* orbitals for the adsorbed TCNQ dimer.

be decisive in a Kondo system. The chains of TCNQ molecules seem to be a perfect system to study the dependence of T_K along the graphene/Ru(0001) surface, or in other words, the spin-electron coupling between the molecules and substrate.

Figure 6.11a shows how the Kondo intensity is modulated along molecular chains covering several unit cells of the moiré pattern, being more intense for the molecules adsorbed on the bridge and *hcp* areas, in good agreement with the results obtained for the individual TCNQ molecules. As expected, the Kondo map also reveals that the spatial distribution of the Kondo signal is exactly distributed across the SOMO of the TCNQ molecules. Taking advantage of the stability of the molecular chains, we performed measurements at different temperatures in order to obtain a value for T_K and confirm that the resonance at zero bias is actually a Kondo resonance. Due to experimental constrains, we can only perform

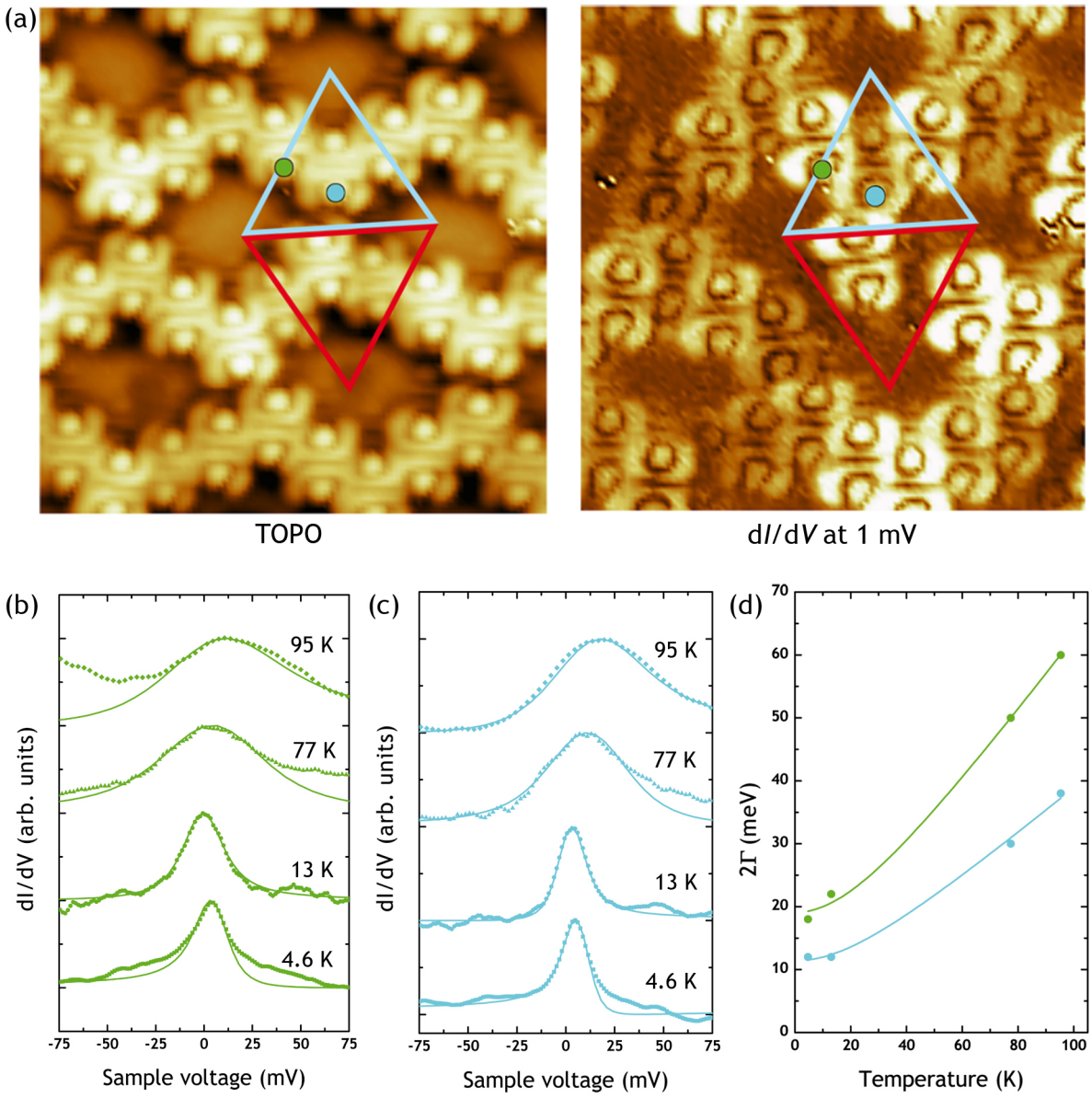

Figure 6.11: (a) Left panel: Topographic STM image ($7 \times 7\,\mathrm{nm}^2$,$V_\mathrm{b} = -0.1\,\mathrm{V}$, $I_\mathrm{t} = 30\,\mathrm{pA}$). Right panel: Its corresponding Kondo map ($V_\mathrm{mod} = 11.3\,\mathrm{mV}$ RMS and $\nu = 703\,\mathrm{Hz}$) taken at 4.6 K. Blue and red triangles indicate the *hcp* and *fcc* regions, respectively. (b-c) $\mathrm{d}I/\mathrm{d}V$ spectra measured on the position marked with a green and blue circles on (a) at different temperatures. The solid lines represents the Fano line shape fit to the experimental data. (d) The values of 2Γ versus the temperature. The fitting results in a $T_K = 66.3\,\mathrm{K}$ for the blue molecule and $T_K = 110.9\,\mathrm{K}$ for the green one.

experiments at four temperatures: 4.6 K, 13 K, 77 K and 95 K. As an illustration, we chose one molecule adsorbed in the *hcp* area (blue) and another one in a bridge position (green). The solid curves of Fig. 6.11b and 6.11c represent the Fano fitting of the experimental data at different temperatures. The values of 2Γ are then represented versus the temperature and fitted

to the eq. 6.8, obtaining the two lines of the Fig. 6.11d. The resultant Kondo temperatures are 66.3 K for the blue molecule and 110.9 K for the green one.

The analysis of the molecular chains provides a clear indication of the complexity of this system. As we saw for low coverage, the differences on the local density of states of graphene/Ru(0001) play an important role in the modulation of the Kondo effect. Depending on the adsorption configuration, the magnetic moment value of the TCNQ molecule and the consequent Kondo resonance changes. However, there is a equivalence between the adsorption sites and the intensity of the Kondo peak as can be seen in the Kondo map shown in the right panel of Fig. 6.11a. The TCNQ molecules adsorbed on the *hcp* and bridge positions present a Kondo resonance which disappears in the case of molecules adsorbed on *fcc* areas. Notice that is complicated to find a TCNQ molecule in which one of its cyano groups is not located on a bridge position. For this reason, almost all the molecules present a Kondo signal.

Monolayer

To complete our study, local spectroscopy measurements were done on the TCNQ monolayer on graphene/Ru(0001). At this coverage, we can also find molecules adsorbed on *atop* regions of the moiré unit cell. Figure 6.12 shows that the Kondo resonance is preserved at this coverage for the molecules adsorbed on the low areas of the moiré. The black curve on Fig. 6.12b is the dI/dV spectrum measured on a molecule adsorbed on an *atop* region. This spectrum is relatively featureless just as the one acquired on a molecule adsorbed on a *fcc* position (red curve). Contrary, a Kondo resonance and the characteristic peaks of an inelastic Kondo effect clearly appear on the spectra measured on TCNQ molecules adsorbed on *hcp* areas. The Kondo map helps us to distinguish between the molecules that present a Kondo resonance and the ones that do not. Again, at this coverage, we can find the correspondence between the adsorption site and the intensity of the Kondo peak. To quantify the width of the Kondo resonance, the spectrum for a TCNQ adsorbed on *hcp* region was fitted by a Fano line shape. The resulting fitting parameters are $q = -6$, $\varepsilon_0 = 10\,\text{meV}$ and $\Gamma = 12 \pm 1\,\text{meV}$ which correspond to a $T_K = 139.2\,\text{K}$. This T_K is higher than the T_K for a molecule on the same adsorption configuration in the molecular chain of Fig. 6.11. Previous experiments of molecules adsorbed on homogeneous substrate showed the importance of the number of the molecular neighbors on the T_K. For instance, in the particular case of TBrPP-Co molecules and a Cu(111) [83], the value of T_K decreases when the number of molecular neighbors increase. The authors explained this behavior as a reduction of the spin-electron coupling strength due to the scattering of surface electrons by the molecules located at edges of the molecular layer. The same behavior was observed on CuPc clusters on Ag(111) [111]. In this case, the dependence of T_K with the number of neighbors is induced by a strong shift of the electronic levels of the molecules due to the intermolecular interaction. On the other hand,

the averaged T_K increases with increasing chain length of Co atoms linked by basic molecular building blocks on a Au(111) surface [112]. Moreover, T_K is also dependent on the even or odd number of molecular units within the chains suggesting an antiferromagnetic (AFM) coupling. In our case, the strongly dependence of the T_K with the adsorption configuration makes very difficult to extract conclusions about this issue and work is in progress to solve it.

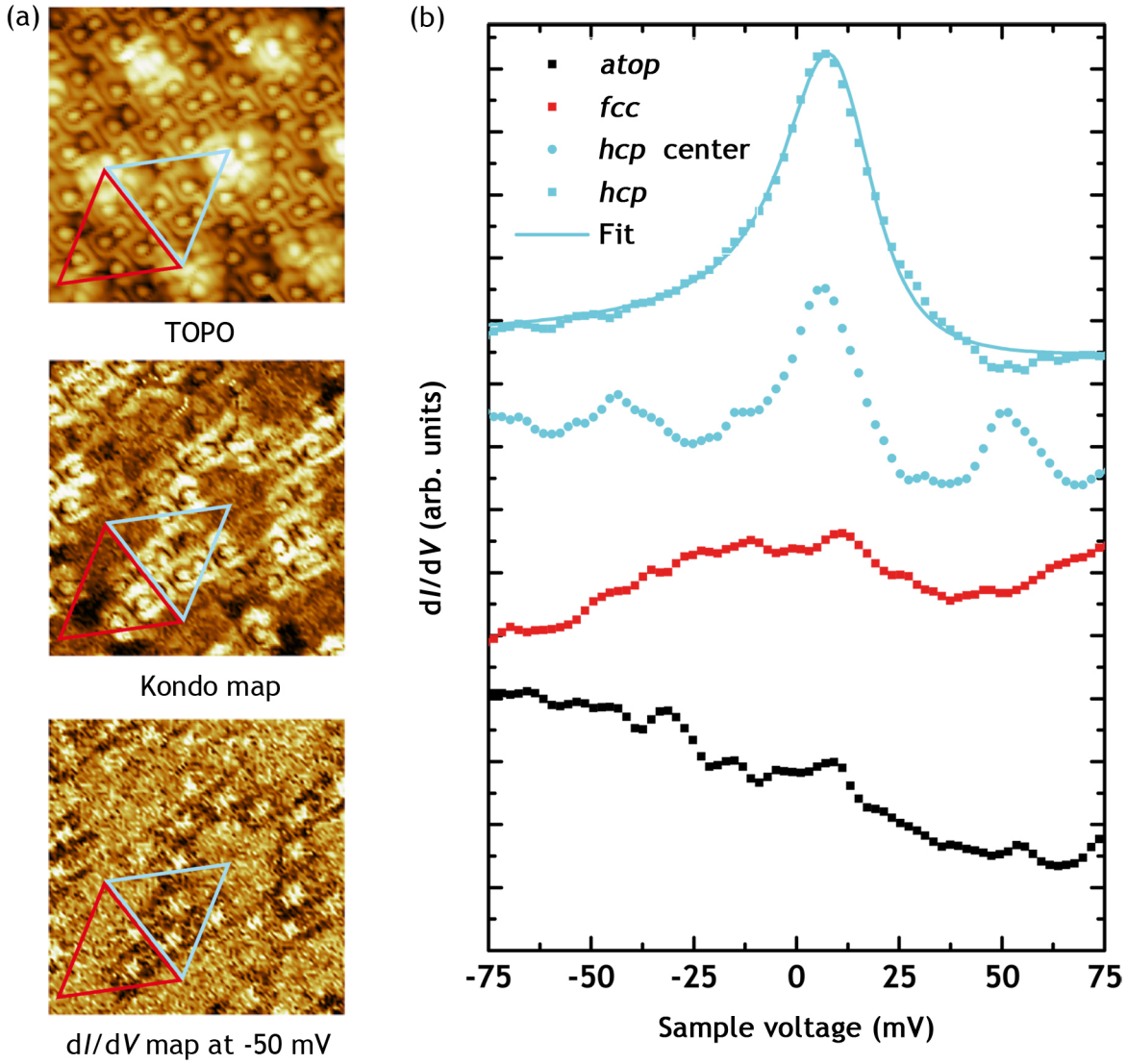

Figure 6.12: (a) STM image of a TCNQ monolayer on graphene/Ru(0001) ($7 \times 7\,\mathrm{nm}^2$, $V_\mathrm{b} = -0.1\,\mathrm{V}$, $I_\mathrm{t} = 20\,\mathrm{pA}$) and the corresponding Kondo map and $\mathrm{d}I/\mathrm{d}V$ map at $-50\,\mathrm{mV}$ acquired simultaneously with a lock-in technique ($V_\mathrm{mod} = 8.5\,\mathrm{mV}$ RMS and $\nu = 703\,\mathrm{Hz}$). Blue and red triangles indicate the *hcp* and *fcc* regions, respectively. (b) $\mathrm{d}I/\mathrm{d}V$ spectra on a TCNQ molecule adsorbed on a *atop* (black curve), *fcc* (red curve) and *hcp* (blue curve) position.

The dI/dV map at $-50\,mV$ shows that there is a maximum of the signal at this energy only in the molecules which present a Kondo resonance, as can be seen in the dI/dV spectra measured at the center of the TCNQ molecules adsorbed on *hcp* position. These molecules exhibit two symmetric side peaks due to the convolution of the step like features typically of an inelastic tunneling process with the Kondo resonance. This behavior is identical to the case of the isolated TCNQ molecules discussed before. For the rest of the TCNQ molecules, we do not observe the characteristic step like inelastic features in the dI/dV curves due to the low energy resolution in the spectra.

In summary, we have systematically studied Kondo effect from individual TCNQ molecules up to the monolayer. The main conclusion is that there is a spatial dependence of the Kondo effect within the moiré unit cell of graphene/Ru(0001). The molecules adsorbed on a *hcp* and bridge configurations present a Kondo resonance which is absent in molecules adsorbed on either a *fcc* or *atop* positions. Besides, the resulting T_K for the TCNQ on *hcp* sites is always lower than the corresponding for TCNQ on bridge sites. This behavior is preserved upon the coverage is increased. The role plays by the graphene is twofold. Firstly, the graphene acts as a decoupling layer allowing exclusively a charge transfer between the Ru and the molecules, creating an unpaired electron ground state on the TCNQ molecules [106]. On the other hand, the graphene layer confines the surface resonance of the Ru(0001) surface. The confinement depends strongly on the graphene-Ru distance, producing a spatial modulation of the density of states of the graphene/Ru(0001) surface close to the Fermi level [36, 37]. In conclusion, the combination of these two process leads to a site dependent Kondo effect. If we substitute the ruthenium substrate by iridium, where the interaction between graphene and metal is much weaker, the situation changes completely and TCNQ molecules do not develop any magnetic moment and consequently, no Kondo effect is observed.

6.1.3 Kondo effect in F_4-TCNQ on graphene/Ru(0001)

To further confirm that the dependence of the Kondo resonance with the adsorption site is due to the role of the graphene layer, we have performed the same experiments on F_4-TCNQ adsorbed on graphene/Ru(0001).

Figure 6.13 shows the STS experiments close to the Fermi level for this system at low coverage. As expected, the Kondo peak shape strongly depends on the location of the molecule within the unit cell of the graphene/Ru(0001). The dI/dV spectra shown in Fig. 6.13b are completely different depending on the molecular adsorption site. In particular, a sharp resonance arises at the Fermi level in the dicyanomethylene ($C(CN_2)$) terminations of the molecules on the *hcp* areas. These peaks fit perfectly to a Fano line shape ($q = -8$, $\varepsilon = 2$ and $\Gamma = 6 \pm 1\,mV$) leading to a $T_K = 69.6\,K$. This Kondo temperature is similar to T_K for individual TCNQ on graphene/Ru(0001) indicating a similar coupling between the molecules and graphene in both cases. However, the Kondo map of Fig. 6.13a shows that in this case the

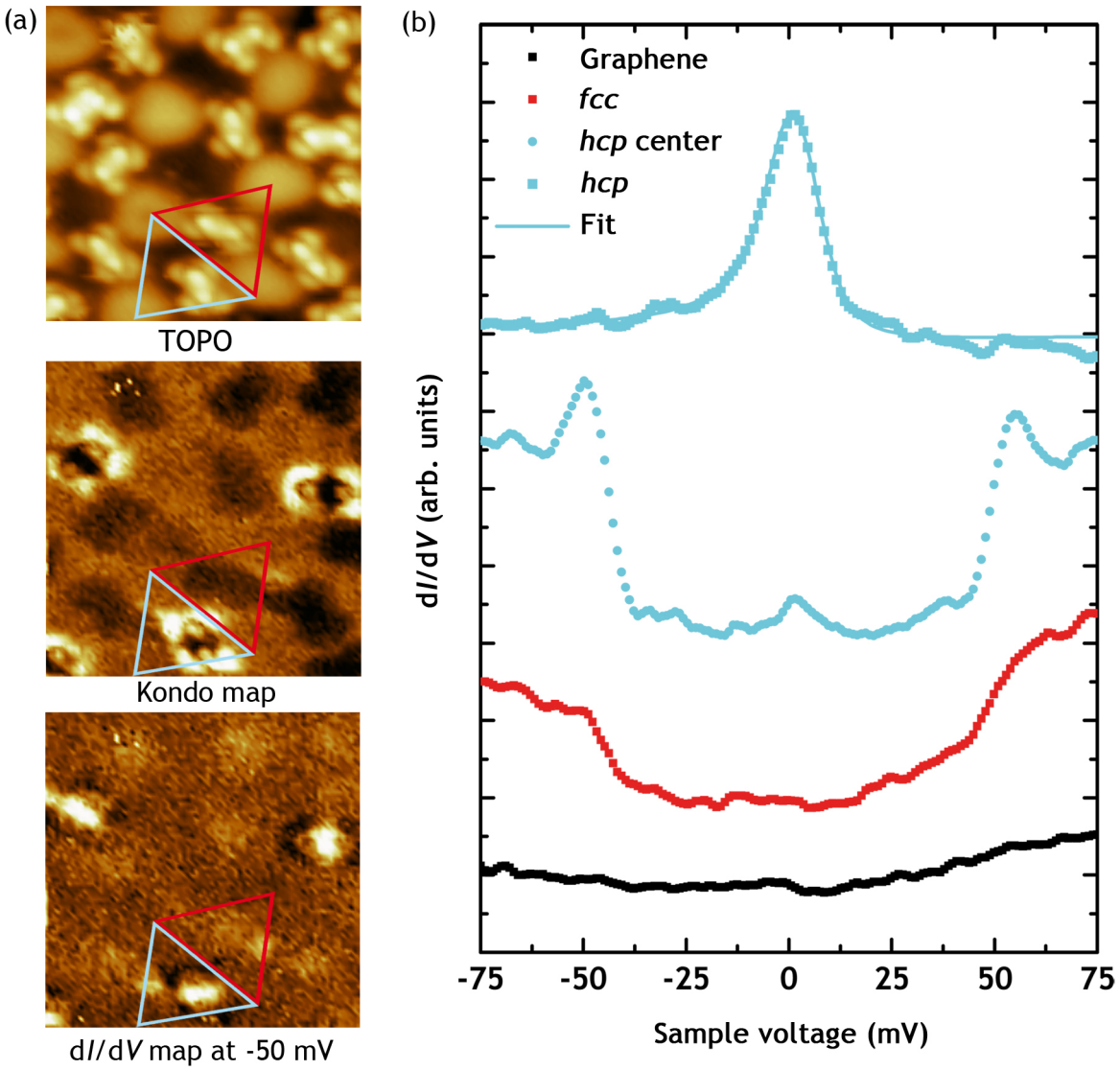

Figure 6.13: (a) Topographic image ($7 \times 7\,\mathrm{nm}^2$) of F_4-TCNQ adsorbed on graphene/Ru(0001) taken at $V_b = -0.1\,\mathrm{V}$ and $I_t = 30\,\mathrm{pA}$, and the corresponding Kondo map and $\mathrm{d}I/\mathrm{d}V$ map at $-50\,\mathrm{mV}$ acquired simultaneously with a lock-in technique ($V_{mod} = 8.5\,\mathrm{mV}$ RMS and $\nu = 703\,\mathrm{Hz}$). Blue and red triangles indicate the *hcp* and *fcc* regions, respectively. (b) $\mathrm{d}I/\mathrm{d}V$ spectra measured on bare graphene (black) and on the molecules adsorb in the *fcc* (yellow) and *hcp* (green) areas. The solid line corresponds to a Fano line shape fit ($q = -8$, $\varepsilon = 2$ and $\Gamma = 6 \pm 1\,\mathrm{mV}$). The measurements were performed at 4.6 K.

Kondo resonance is only located on the $C(CN_2)$ termination group of F_4-TCNQ molecule. This difference of the spatial distribution of the Kondo resonance across the molecule between the TCNQ and F_4-TCNQ give us information about the localization of the extra charge on the molecule. While for TCNQ the electron distributes across the molecule and the Kondo signal is located on the SOMO, for F_4-TCNQ the extra charge is localized on the cyano groups of the molecule and the Kondo signal is more intense in these areas even though the LUMO

is extended all over the molecule (Fig. 4.12c).

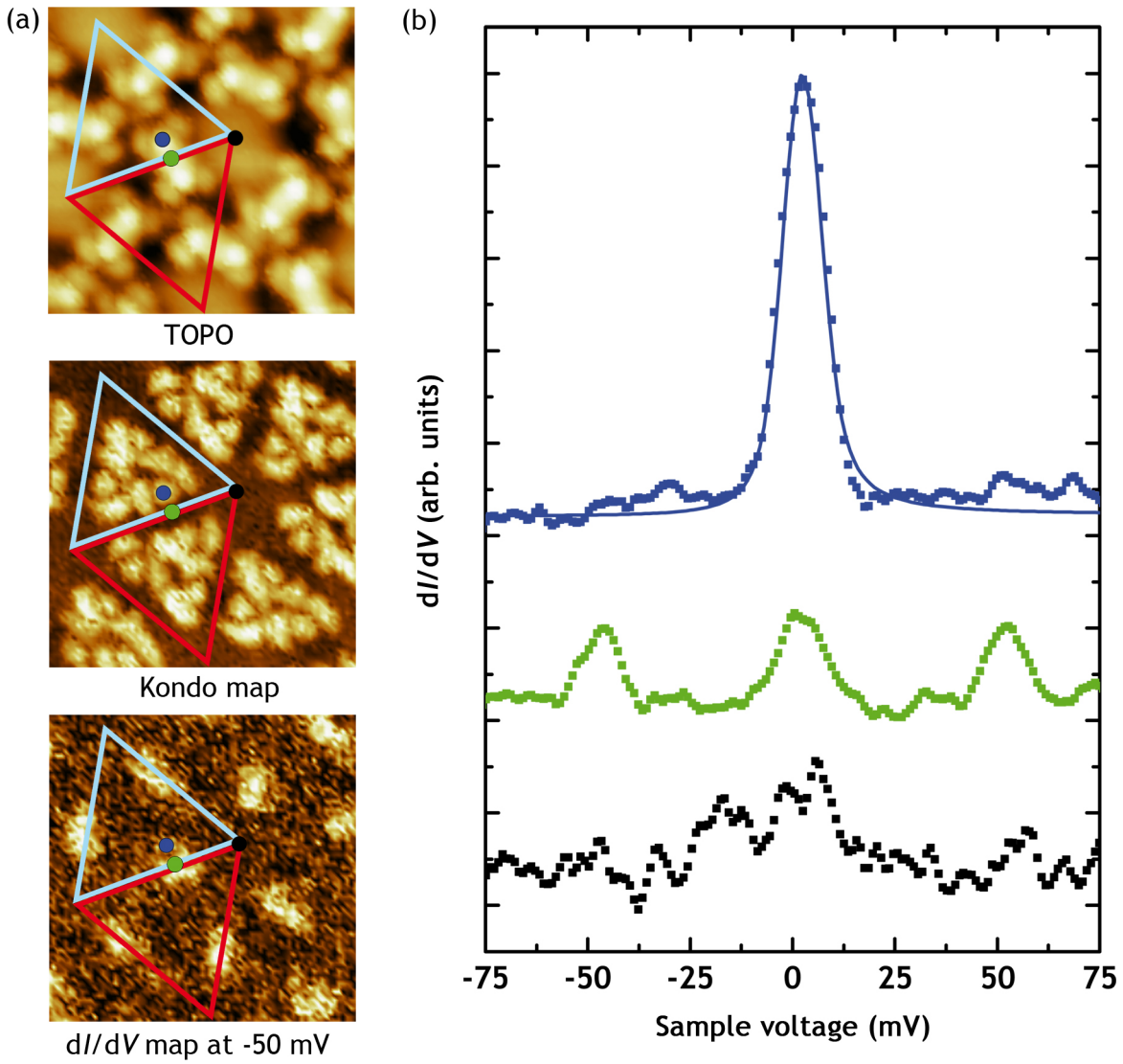

Figure 6.14: (a) Topographic image ($5 \times 5\,\mathrm{nm}^2$) of F_4-TCNQ adsorbed on graphene/Ru(0001) taken at $V_b = -0.2\,\mathrm{V}$ and $I_t = 50\,\mathrm{pA}$, and the corresponding Kondo map and $\mathrm{d}I/\mathrm{d}V$ map at $-50\,\mathrm{mV}$ acquired simultaneously with a lock-in technique ($V_{mod} = 14.1\,\mathrm{mV}$ RMS and $\nu = 703\,\mathrm{Hz}$). Blue and red triangles indicate the *hcp* and *fcc* regions, respectively. (b) $\mathrm{d}I/\mathrm{d}V$ spectra measured on bare graphene (black) and on the center and on a dicyanomethylene termination group of F_4-TCNQ molecule. The solid line corresponds to a Fano line shape fit ($q = 40$, $\varepsilon = 2$ and $\Gamma = 7 \pm 1\,\mathrm{mV}$). The measurements were performed at 4.6 K.

As in the case of TCNQ, when the tip is located on the center of the molecules, two symmetric bands appear at $\pm 50\,\mathrm{mV}$. We attribute these peaks to an inelastic Kondo effect due to an interplane molecular vibration of the central ring of the molecule. The energy associated to these inelastic peaks is slightly higher than in the case of TCNQ molecules

on graphene/Ru(0001), as expected, due to the substitution of hydrogen atoms by heavier fluorine atoms. On the other hand, the dI/dV spectra close to the Fermi level in molecules adsorbed on *fcc* areas show the typically step like features characteristic of an inelastic excitation without Kondo. The spatial localization of these vibrational features are visualized on the dI/dV map taken at $-50\,mV$. In Fig. 6.13a, the vibrational features are localized on the center of the F_4-TCNQ molecules being more intense on the molecules adsorbed on *hcp* positions, where the vibrational steps are convoluted with the Kondo resonance.

Increasing the coverage, the repulsive interaction between molecules an the spatial adsorption selectivity gives rise to a triangular ring structures where the cyano group of one molecule is between the cyano groups of the other two. In this configuration, all the F_4-TCNQ molecules are placed on bridge position and present a sharp Kondo peak, see Fig. 6.14. Figure 6.14b shows the spectra obtained in bare graphene and in two different positions within the molecule. The Fano fitting of the Kondo resonance yields a $T_K = 81.2\,K$. It is worthy to mention that all the molecules present the same intensity for all the $C(CN_2)$ terminations in the Kondo map. This fact suggests that all the molecules present the same spin-electron coupling strength, as expected, for molecules adsorbed on the same position. These results confirm the importance of the molecule-substrate interactions on the development of a Kondo effect.

6.2 Long-range magnetic order in TCNQ monolayer

The evolution from isolated magnetic moments to magnetically ordered monolayer is not been well understood yet. For metallic systems, there are experimental evidences concerning mostly the extreme cases of isolated impurities or complete monolayers. For instance, an isolated Co atom adsorbed on Cu(100) displays Kondo effect with a T_K of 88 ± 4 K [113], while a thin film of Co on Cu(100) shows long-range ferromagnetic order detected by SP-STM [114]. For organic molecules, previous experiments reported the coexistence of Kondo with antiferromagnetism (AFM) in two-dimensional islands of FePc on Au(111) where the molecular spins are coupled through a long-range surface mediated RKKY interaction [115].

In the previous section, we explored the modulation of the Kondo peak along a TCNQ monolayer on graphene/Ru(0001). In this section, we are interested in unveiling the appearance of a magnetic order in this TCNQ monolayer. Firstly, we will briefly discuss the conditions for obtaining a fully spin polarized ground state in a purely organic material. Later, we will investigate the TCNQ monolayer on graphene/Ru(0001) system by means of spin polarized calculations and SP-STS experiments in order to check the existence of a long-rage magnetic order. Finally, we will discuss the possible sources of artifacts in the SP-STM experiments.

6.2.1 Band ferromagnetism in organic materials

Organic magnets have attracted sustained interest for both their fundamental properties and their potential technological applications [116]. $V(TCNE)_2$ was the first example of an organic magnet with a Curie temperature,T_C, above room temperature ($T_C = 400\,K$) [117]. The mechanism to achieve long-range magnetic order in these systems was the introduction of metal ions in the organic matrix, which induce antiferromagnetic coupling between the localized spins of the metal ion and the radical organic anions. Other advances rely in charge transfer processes that generate organic anions with magnetic properties, like the case of high-temperature selected metal–cyanide-based organometallic magnets [118]. Another example is TDAE-C_{60}, where unpaired electrons localized on C_{60} molecules become ferromagnetic below $T_C = 16\,K$ [119]. All the previous examples contain a mixture of metallic atoms and organic molecules, however, no examples are known, so far, of purely organic molecules with a magnetic moment originated from delocalized bands, as e.g. in Co, Ni or Fe, the classic ferromagnetic metals.

Recently, a theoretical proposal was made for a novel possibility of a band ferromagnetism in a purely organic polymer [120]. They found a chain of five-membered rings (polyaminotriazole) which presents a flat band that doped appropriately with a gate voltage can be half-filled and develops a ferromagnetic ground state. These results are based on theoretical studies on the ferromagnetism using the Hubbard model. The Hubbard model was proposed in 1963 by J. Hubbard who introduced a Hamiltonian in order to model electronic correlations in narrow energy bands and gave a number of different approaches to the associated many-body problem [121]. In its simplest version, it describes tight-binding electrons where the interaction among them is modeled with an on-site Coulomb interaction U, a parameter of the model. Since the number of electrons per atoms is fixed, the Coulomb interaction U can favor the formation of a magnetic moment. The first rigorous example of ferromagnetism in the Hubbard model was suggested by Y. Nagaoka 50 years ago [122]. Nagaoka's ferromagnetism establishes that certain Hubbard models have a ferromagnetic ground state in a narrow, almost half-filled s band with a strong Coulomb interaction U. Later, E. H. Lieb [123], A. Mielke [124] and independently H. Tasaki [125], extended Nagaoka's results and proved that for different classes of half-filled flat band models with a Coulomb interaction $U > 0$, a fully spin polarized ground state is guarantee. These effects are now known collectively as *flat band ferromagnetism*. However, experimentally no organic materials which such flat band have been synthesized yet.

6.2.2 Spin polarized organic bands in TCNQ monolayer

As anticipated in the previous chapter, the graphene layer transfers charge to the TCNQ monolayer on graphene/Ru(0001). The transferred charge is delocalized along an intermolecular band that results from the hybridization of the TCNQ frontier molecular orbitals.

Configuration	$\mu(\mu_B)$ **/molecule**	$\Delta \mathbf{E} = \mathbf{E_{Configuration}} - \mathbf{E_{BS}}(\mathbf{meV})$
NM	0.0 (0.0)	0.0 (0.0)
HS	0.5 (0.5)	105.1 (106.6)
Free	0.24 (0.24)	−53.90 (−52.40)

Table 6.3: Magnetic moments per molecule and relative energies per unit cell, ΔE, of different magnetic configurations for a free standing TCNQ monolayer charged with 0.5 electrons per molecule. LS: Low spin configuration; HS: high-spin configuration; Free: configuration in which the magnetic moments have been allowed to relax without constraints. Data in parentheses are referred to the calculations performed using the non-collinear DFT framework, including spin-orbit coupling [36, 106].

Spin polarized calculations reveal that the most stable configuration for TCNQ monolayer adsorbed on graphene/Ru(0001) corresponds to the spin of the electrons that occupy the SOMO-derived band aligned parallel, following the behavior for the dimer (Fig. 6.10) where this delocalization allows, by virtue of a sort of giant intermolecular Hund's rule, that the electron spins remain parallel to each other. For a unit cell containing eight TCNQ molecules, the corresponding calculated magnetic moment is 1.3 μ_B (0.18 μ_B/molecule).

To confirm the robustness of these results, Table 6.3 shows the magnetic moment per molecule and relative energies per unit cell, ΔE, of different magnetic configurations for a free-standing TCNQ monolayer charged with 0.5 electrons/molecule and with the same corrugated geometry as the adsorbed one. This simpler model allows us to understand the physics of the system in a realistic way because, as we conclude from our experiments, the role of the graphene/Ru(0001) substrate is just to provide the appropriated charge to the TCNQ molecules and, simultaneously, decoupled them from the ruthenium substrate. In the Table 6.3, three different electronic configurations are shown; non magnetic configuration (NM) where the difference between the spin-up and spin-down electron of the supercell has been forced to be 0, high-spin configuration (HS) in which this difference has been forced to be 4 and free configurations (Free) in which the difference between spin-up and spin-down electrons is allowed to vary without constrains. Accordingly, the magnetic order is favorable in the TCNQ monolayer by 50 meV, with a magnetic moment of 0.24 μ_B/molecule. This result does not vary significantly after the inclusion of the spin-orbit effects (data in parentheses in Table. 6.3) or employing the larger $5 \times 5 \times 1$ grid of k-points, instead of the $3 \times 3 \times 1$ one [36, 106]. In conclusion, a charged, free-standing TCNQ monolayer with the geometry found experimentally develops a complex, probably non-collinear, long-range magnetic order.

Furthermore, the calculations also reveal that the corresponding bands in the reciprocal space are almost flat and have a magnetic character. Figure 6.15a shows the calculated electronic density distribution of the Γ-point of the first empty band for a free-standing TCNQ monolayer with the same corrugated geometry as the real TCNQ monolayer on

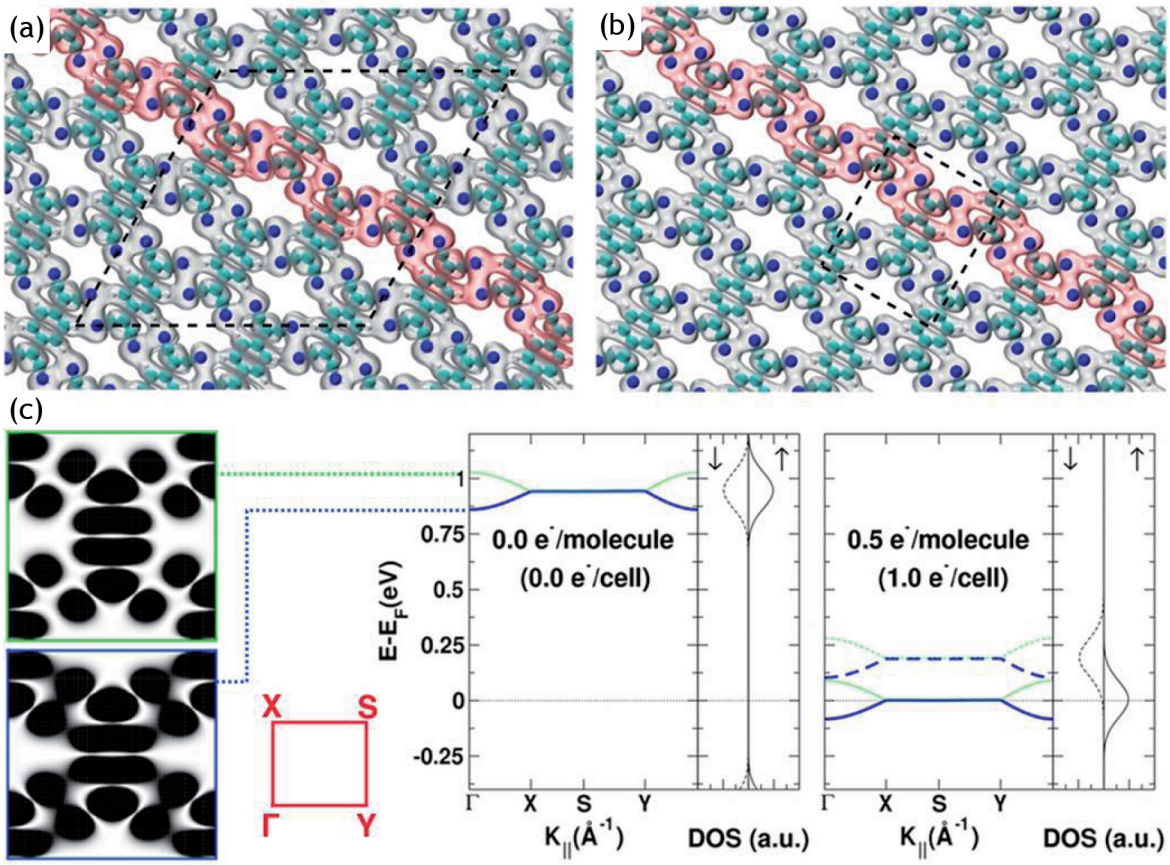

Figure 6.15: (a) Electronic density distribution at the Γ-point of the first empty band for an isolated TCNQ monolayer, calculated using the same unit cell (black dashed line) and geometry of the actual TCNQ monolayer on graphene/Ru(0001). Carbon, nitrogen and hydrogen atoms are shown on cyan, blue and white respectively. (b) Same as (a) but for a planar TCNQ monolayer. (c) Band structure and density of states of planar TCNQ monolayer, for increasing amounts of extra charge (from left to right). Leftmost panel shows the electronic density distribution at the Γ-point (average in the z-direction) of the bands formed by the anti-symmetric (blue) and symmetric (green) combinations of TCNQ's LUMO. Solid and dashed lines refer to spin-up and spin-down components. The red inset shows the unit cell of the first Brillouin zone [106].

graphene/Ru(0001). The dashed black line represents the (11×11) moiré unit cell that contains eight TCNQ molecules. In agreement with the experimental STM images (see Fig. 5.6), the intermolecular band results for the anti-symmetric combination of the LUMO of the TCNQ molecules. In order to simplify the calculations and due to the weak interaction with the substrate, the electronic density distribution at the Γ-point of the first empty band for a planar, free-standing TCNQ monolayer was calculated, see Fig. 6.15b. The shape of these bands is indistinguishable from the ones calculated for a corrugated free-standing monolayer, but the smaller size of the unit cell with only two molecules (marked with dashed black lines in Fig. 6.15b) allows a more clear analysis of the dispersion of the bands. In

Fig. 6.15c, leftmost panel shows the electronic density distribution at the Γ-point (average in the z-direction) of the bands formed by the anti-symmetric (blue) and symmetric (green) combinations of TCNQ's LUMO. The red inset shows the unit cell of the first Brillouin zone. Center and right panels of Fig. 6.15c show the band structure and density of states of neutral and charged planar TCNQ monolayer. The solid and dashed lines refer to spin-up and spin-down components. As can be seen the LUMO-derived band, which is almost flat and completely empty for a neutral monolayer, remains flat but splits for a monolayer charged with 0.5 electrons/molecule. It splits in a spin-up almost completely filled band (SOMO-derived band) and in the spin-down counterpart empty band (SUMO-derived band), in agreement with our STS experiments (Sec. 5.1). The spin polarized calculations suggest then that the charged TCNQ monolayer develops a nearly half-filled flat band with a magnetic order ground state. Therefore, TCNQ monolayer on graphene/Ru(0001) might be the first example of an organic material exhibiting long-range magnetic order.

6.2.3 Imaging the spin contrast of the magnetic TCNQ domains

To test the predictions about the long rage magnetic order in TCNQ monolayer on graphene/Ru(0001) we perform SP-STS experiments at low temperature. The aim of our experiments is to use magnetic Fe/W tips sensitive to in-plane magnetization as a probe to extract magnetic information about our sample. For this purpose, magnetic tips were prepared following the treatment described on Sec. 2.3.3. These tips were tested on Mn films grown on Fe(001) system. The Fe covered tips reproduce the magnetic contrast between adjacent terraces due to the antiferromagnetic layered structure of the Mn films (Fig. 2.3), although the intensity in the signal changes from tip to tip due to the lack of control on the tips magnetization. For TCNQ monolayer on graphene/Ru(0001), the hierarchical way of growing of the TCNQ molecules on the substrate allows the existence of domains with the axis of the molecules rotated between domains. As a consequence, in the TCNQ monolayer is expected the existence of magnetic domains due to the difference in the angular orientation of the TCNQ molecules and, therefore, in the spin polarized intermolecular bands. The existence of these domains will allow us to get SP-STM images with contrast without an external magnetic field. In such a way, we expect different current intensities in different TCNQ domains for a given tip magnetization direction. Furthermore, spin polarized calculations revealed that SUMO-derived and SOMO-derived bands are spin splitted, therefore, the intensity of these resonances in the spin polarized $\mathrm{d}I/\mathrm{d}V$ spectra for different domains should be opposite. If the peak that corresponds to the SOMO-derived band is more intense in domain A, the counterpart SUMO-derived peak should be more intense in domain B, because the frontier resonances present opposite spin polarization. Simultaneously, the intensity of the peaks corresponding to the double occupied HOMO-derived band should not change between domains.

Figure 6.16 shows the STS experiments on a TCNQ monolayer with two domains per-

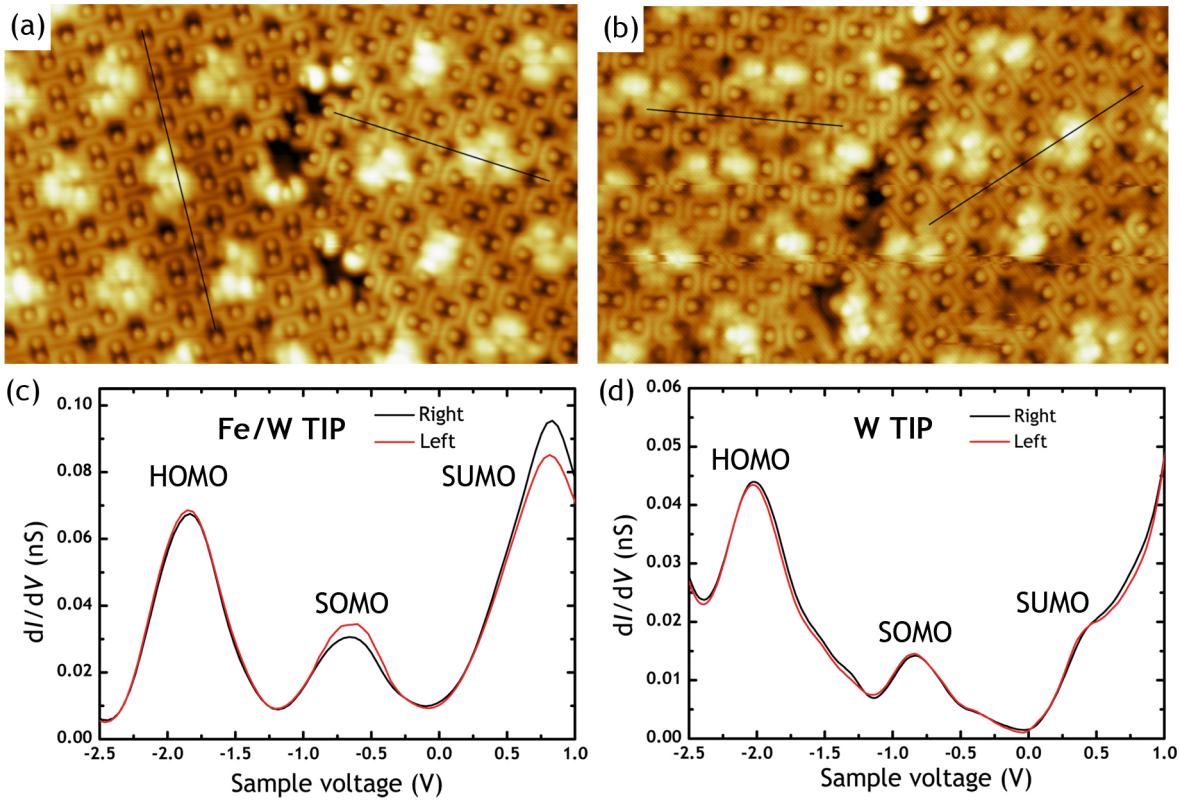

Figure 6.16: (a) STM topographic image ($16 \times 10\,\mathrm{nm}^2$) of two TCNQ domains on graphene/Ru(0001) measured with a Fe coated tip at 4.6 K with the tunneling gap stabilized at $V_\mathrm{b} = -1\,\mathrm{V}$ and $I_\mathrm{t} = 40\,\mathrm{pA}$. (b) Similar STM topographic image ($16 \times 10\,\mathrm{nm}^2$) than (a) measured with W tip at 4.6 K with the tunneling gap stabilized at $V_\mathrm{b} = -1\,\mathrm{V}$ and $I_\mathrm{t} = 20\,\mathrm{pA}$. The black lines in (a) and (b) indicate the long axis of the TCNQ molecules in the molecular domains. (c) Spin polarized $\mathrm{d}I/\mathrm{d}V$ curves averaged over three unit cells of the moiré superstructure for the left (red) and right (black) domains of (a). The individual curves have been taken at 4.6 K using a Fe/W tip with the tunneling gap stabilized at $V_\mathrm{b} = +1.5\,\mathrm{V}$ and $I_\mathrm{t} = 40\,\mathrm{pA}$. The three peaks correspond to the HOMO (at -1.8V), SOMO (at $-0.7\,\mathrm{V}$) and SUMO (at $+0.7\,\mathrm{V}$) bands. (d) Spin integrated $\mathrm{d}I/\mathrm{d}V$ curves averaged over three unit cells of the moiré superstructure for the left (red) and right (black) domains of (b). The individual curves have been taken at 4.6 K using a W tip with the tunneling gap stabilized at $V_\mathrm{b} = +1.5\,\mathrm{V}$ and $I_\mathrm{t} = 20\,\mathrm{pA}$. [106].

formed with a W tip and Fe/W tip. In both cases, the $\mathrm{d}I/\mathrm{d}V$ signal was acquired by means of lock-in techniques by adding an AC component to the gap voltage ($V_\mathrm{mod} = 50\,\mathrm{mV}$ RMS and $\nu = 703\,\mathrm{Hz}$) while the DC component of the gap voltage was ramped linearly and the feedback circuit was switched off. Figure 6.16c and Fig. 6.16d compare the $\mathrm{d}I/\mathrm{d}V$ in the two domains of the constant-current topographic image of Fig. 6.16a and Fig. 6.16b measured with a magnetic tip and non magnetic tips, respectively. The analysis of the $\mathrm{d}I/\mathrm{d}V$ spectroscopy for a TCNQ monolayer on graphene/Ru(0001) is not an easy task as we saw

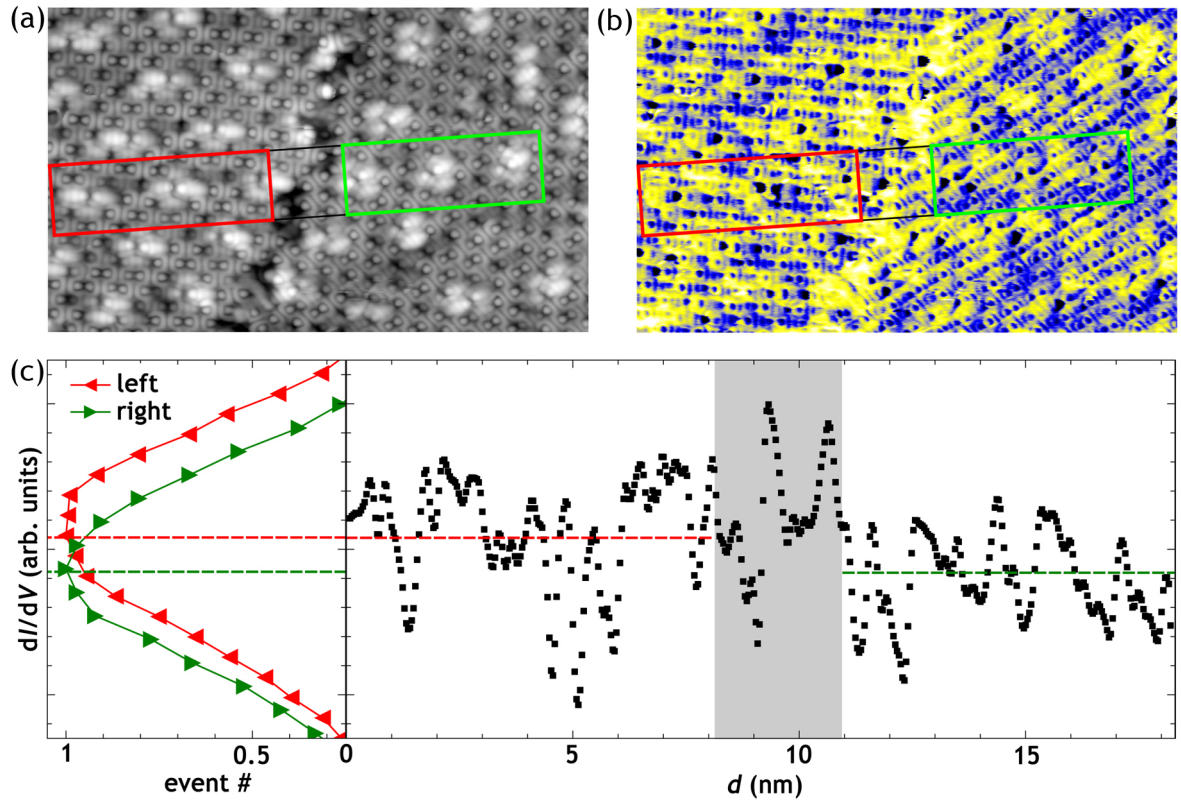

Figure 6.17: (a) STM topography ($20 \times 12\,\mathrm{nm}^2$, $V_b = -0.7\,\mathrm{V}$, $I_t = 20\,\mathrm{pA}$) of a TCNQ monolayer on graphene/Ru(0001) measured at 4.6 K where two TCNQ domains are shown. (b) Spin polarized $\mathrm{d}I/\mathrm{d}V$ map recorded simultaneously with the topography of (a) at $-0.7\,\mathrm{V}$ (energy of the SOMO-derived band). (c) Left panel: normalized $\mathrm{d}I/\mathrm{d}V$ histograms corresponding to each domain in the $\mathrm{d}I/\mathrm{d}V$ map of (b). It shows a clear shift in the average intensity of the SOMO band. Right panel: average of 70 profiles acquired on the $\mathrm{d}I/\mathrm{d}V$ map of (b) corresponding to the rectangular region. The average intensity of each domain is indicated by the red (left domain) and green (right domain) dashed lines.

in Sec. 5.1. Although, the same three features that we identify with the HOMO, SOMO and SUMO bands appear for all the molecules, depending on the adsorption site, the molecule-substrate interaction change and, in turn, the intensity and energy position of the peaks may be modified. For this reason, we compare the spin-resolved differential tunneling conductance averaged over three moiré unit cells which contains around 30 molecules. Notice that the individual curves of Fig. 6.16c and Fig. 6.16d have been taken at 4.6 K with the same tunneling gap stabilized at $V_b = +1.5\,\mathrm{V}$, in order to avoid artifacts (see next subsection for more information). The spin polarized $\mathrm{d}I/\mathrm{d}V$ curves exhibit, as expected, different intensity for the SOMO peaks in both domains and a reversal in the intensity signal for the SUMO peaks. On the other hand, the intensity of the HOMO peak is the same in both domains, as expected, for a spin unpolarized band. These differences are no visible in the spin integrated

$\mathrm{d}I/\mathrm{d}V$ curves of Fig. 6.16d.

Taking advantage of the spatial resolution provided by STM, we can also obtain a magnetic contrast map of the surface. Figure 6.17 shows the analysis of the magnetic intensity of a magnetic contrast map of the SOMO-derived band in two TCNQ domains. The spin polarized $\mathrm{d}I/\mathrm{d}V$ map for the spin polarized SOMO level at -0.7 eV (Fig. 6.17b) was obtained with a Fe-coated tip at 4.6 K and measured simultaneously with the topographic image shown in Fig. 6.17a. Although, it reveals a magnetic contrast between the two TCNQ domains, inside each domain, there are periodic differences in the intensity of the SOMO level for molecules located on high and low areas of the moiré as discussed previously. In order to compare both domains, we choose the area indicated by a rectangle in Fig. 6.17a and 6.17b where each domain is highlighted by red (left domain) and green (right domain) color. The average intensity of the SOMO-derived band measured in one domain is larger than in the other, as demonstrated the histogram and the average profile of Fig. 6.17c. The histograms are measured on the colored areas of the spin-resolved $\mathrm{d}I/\mathrm{d}V$ map of Fig. 6.17b while the profile corresponds to an average of 70 profiles acquired on the rectangular area of the same $\mathrm{d}I/\mathrm{d}V$ map. The different average intensity values in each domains are in good agreement with the spin polarized data shown in Fig. 6.16. Similar images recorded with a non magnetic tip only show the periodic differences in the intensity of the SOMO-derived band inside each domain without any measurable difference from domain to domain. These observations indicate the existence of long-range magnetic order in the TCNQ adlayer at 4.6 K.

6.2.4 Data reproducibility and possible sources of artifacts

There are a number of issues that may produce artifacts in the SP-STS spectra. The most relevant ones are the shape and composition of the apex of the tip, the stray field produced by the ferromagnetic coating of the W tip and the influence of the tunneling parameter used to stabilize the distance between tip and sample during the measurements. Special care has been taken to reproduce the experimental results and to avoid all the mentioned artifacts in our measurements as explained below.

Data reproducibility

The issue of reproducibility in SP-STM measurements is always delicate and we have carefully addressed it. An additional example of the spin contrast is now shown Fig. 6.18. Figure 6.18b shows individual spin-resolved differential tunneling conductance spectra for TCNQ on graphene/Ru(0001) recorded on equivalent molecules of two different domains. The data was measured simultaneously with the topographic image in Fig. 6.18a using a Fe coated tip at 4.6 K. The spin polarized tunneling spectra show a different intensity for the spin polarized SOMO level at -0.7 eV and SUMO level at $+0.75$ eV in the two domains. The intensity is lower for the SOMO in the left domain while it is higher for the SUMO. On the

contrary, the intensity of the double occupied, and, therefore, spin unpolarized HOMO level at $-2.1\,\mathrm{eV}$ is identical in both domains. The change in intensity of the SOMO and SUMO in the spin polarized $\mathrm{d}I/\mathrm{d}V$ curves in this figure is 17 %, i.e., comparable in magnitude to those measured in magnetic metallic substrates (see Fig. 2.3). The signal change is also comparable with the values obtained for $TbPc_2$ molecules deposited on a ferromagnetic surface, as recently reported by J. Schwöbel *et al.* [8].

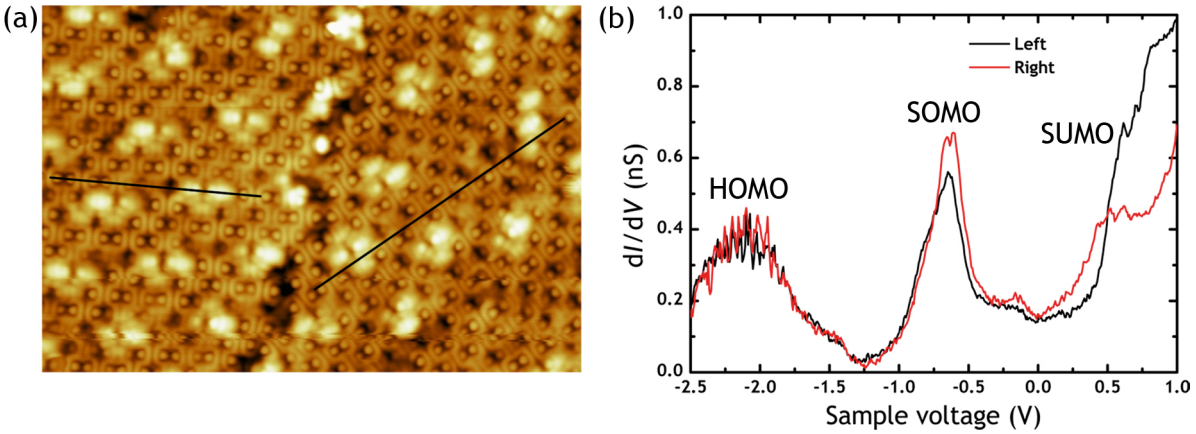

Figure 6.18: (a) STM topography ($19.7 \times 12.2\,\mathrm{nm}^2$) of TCNQ monolayer grown on graphene/Ru(0001) recorded at 4.6 K with the tunneling gap stabilized at $V_\mathrm{b} = -1.0\,\mathrm{V}$ and $I_\mathrm{t} = 20\,\mathrm{pA}$. The black lines mark the long axis of the TCNQ molecules on the domains aligned in different directions. (b) Individual $\mathrm{d}I/\mathrm{d}V$ curves measured with a Fe coated tip on equivalent molecules in the lower areas of both domains of (a). The three peaks correspond to the HOMO (broad peak at $-2.1\,\mathrm{V}$), SOMO (at $-0.7\,\mathrm{V}$) and SUMO (shoulder at $+0.75\,\mathrm{V}$) molecular bands [106].

Influence of the tunneling parameters

During the acquisition of SP-STS data in different magnetic domains is important to be sure that the tip sample distance does not change when the tip is moved from one domain to the next. In our case, special care has been taken to avoid the energy of any of the molecular bands when choosing the bias voltage used to stabilize the feedback loop. In this way, we are minimizing changes in the tip-sample distance when moving from one domain to the next that may produce artificial changes in the peak intensity. In addition, measurements taken using negative or positive bias voltages to stabilized the feedback show that the magnetic contrast are independent of the sign of the bias voltage.

Influence of the tip structure

The shape of the magnetic tip has also a direct influence on the spin polarized experiments. The asymmetries and contamination of the tip apex may reduce the spin polarization or

produce a magnetic stray field (see below) [6]. In order to avoid the contamination of the tip, a clean environment has to be guarantee. Regarding this issue, we prepared our Fe coated tips *in-situ*, besides, during the Fe evaporation the pressure was kept below 2×10^{-9} mbar. A critical moment after tip preparation is the approach to the surface, a control approach is fundamental to avoid drops of material from the tip or a crash between the tip and the sample. On the other hand, we pay special attention to the spatial resolution of the spin polarized images during the data acquisition, excluding the topographic images that present strange resolution which can probably be produced by an asymmetric tip.

Comparing the averaged $\mathrm{d}I/\mathrm{d}V$ curves shown in Fig. 6.16 and the individual ones in Fig. 6.18 also illustrates the reproducibility of the observations using different Fe coated tips and TCNQ domains. Similar observations have been made with dozens of tips with only 10 % of them yielding non-reproducible results. The shape and energy positions of the HOMO, SOMO and SUMO levels change slightly from tip to tip due to the influence of the tip apex electronic structure, but the simultaneous appearance of the three peaks in the same spectrum allows us to discard a major influence of the tip electronic structure in the change in intensity of the SOMO and SUMO levels for a given experimental run. The small shift in the energy position of the peaks observed with different Fe coated tips is ascribed to the electric field produced by the tip that has a minor effect on the energy position of the molecular orbitals when the molecules are sufficiently decoupled from the substrate, as occurs it in this case.

Influence of the tip stray field

The influence of the stray field of the tip on the domain structure of the sample is another crucial parameter which has to be considered. A sizable stray field can modify or destroy the intrinsic domain structure of the sample. The tips used for our spin polarized measurements are clean W tips coated in-situ with 20 ML of Fe. It was reported, for Fe coating higher than 100 ML, magnetic modifications induces by the tip. For instance, M. Bode *et al.* found asymmetry images of Gd(0001) islands grown on a W(110) substrate for tip coated by an Fe film of approximately 150 ML thickness [126]. In this case, the magnetic switching of the tip can be ruled out since other Gd islands are imaged unchanged in subsequent scan lines. It has been shown also that the stray field produce by ultrathin ferromagnetic film tips (3 ML of Fe/W tip) is enough to erase the magnetic domains in soft ferromagnetic materials and, therefore, to reduce the contrast in the spin polarized $\mathrm{d}I/\mathrm{d}V$ maps [6]. However, there are no examples of the tip stray field inducing the appearance of domains in a paramagnetic system. Concerning the influence of the magnetic stray field in our spin polarized measurements, we thus conclude that the magnetic domains imaged here are not due to the stray field. It is worth to recall that in order to take topographic images or measure the $\mathrm{d}I/\mathrm{d}V$ curves (spin polarized or not) a very small tunneling current (always below 100 pA) is used to reduce

the interaction between the tip and the molecules, otherwise the tip moves the molecules during the measurements. The correspondingly large tip-surface distance will also decrease substantially the effective stray field.

6.3 Conclusions

In this chapter, we focused on the study of the magnetic properties of molecules on graphene/Ru(0001). In the first section, we explored the rich physics of the Kondo effect on purely organic materials on graphene/Ru(0001). We showed that the graphene layer provided the appropriate extra charge to the TCNQ molecules which develop a magnetic moment. These results were verified by measuring the corresponding Kondo resonance with local STS at low temperature. As the calculations predicted, the Kondo resonance depends strongly on the adsorption site of the molecule within the moiré unit cell. This dependence was further confirmed for higher TCNQ coverages and for F_4-TCNQ molecules on the same surface. Besides, the characteristic inelastic Kondo features associated to some TCNq vibrational modes were observed and spatially identified in the $\mathrm{d}I/\mathrm{d}V$ maps. The Kondo temperature for each system were obtained fitting the $\mathrm{d}I/\mathrm{d}V$ to a Fano line shape.

The study of this Kondo effect at single molecule level on graphene/Ru(0001) provides us the important information about the molecule-substrate interaction. Graphene/Ru(0001) offers the possibility of get different molecule-substrate interaction leading to different spin-electron coupling between the molecules and the conduction electrons of the substrate. The role of the graphene layer is just to modulate the interaction between the conduction electron of the Ru and molecules.

In the second section, the appearance of long-rage magnetic order on TCNQ monolayer on graphene/Ru(0001) was discussed and probed by SP-STM. The molecular self-organization of TCNQ spontaneously leads to the formation of intermolecular, flat electronic bands extending all over the monolayer. The bands are spin split, with only the majority spin band being occupied. The existence of the corresponding long-range magnetic order is detected by spin polarized STM at 4.6 K.

The existence of fully spin polarized electronic bands in a single organic monolayer can be used to produce an efficient spin filter out of graphene, because an electron current of both spins injected into TCNQ/graphene will become spin polarized due to the preferential transport of minority spins in the empty band. This would allow one to add magnetic functionalities to graphene, a topic of the utmost interest these days.

7 Conclusions

The investigation of the fundamental electronic and magnetic properties of molecular organic materials and their interaction with solid surfaces constitutes a valuable source of knowledge for potential technological applications. As an initial step in this field, this thesis presents a study of electron acceptor molecules on epitaxial graphene. First, the graphene/Ru(0001) and the graphene/Ir(111) surfaces were grown and well characterized (Chap. 3), thereupon we moved to explore the molecular adsorption behavior of TCNQ and F_4-TCNQ molecules on these surfaces. The structural, electronic and magnetic properties of these systems were unveiled by means of scanning tunneling microscopy and spectroscopy and the main conclusions of each aspect are described following.

Concerning the **structural properties** (Chap. 4), we concluded that the self-assembly process of TCNQ and F_4-TCNQ molecules are governed by the properties of the graphene surface. For graphene/Ir(111), the weak interaction between the graphene layer and the underneath metallic substrate gives rise to an electronically homogeneous surface where the intermolecular interaction dictates the molecular order. Contrariwise, the geometric and electronic corrugations of the graphene/Ru(0001) surface lead, at early stages of coverage, to a preferential adsorption of the molecules ending in a supramolecular structure stabilized by the mutual interaction between them.

Furthermore, the decoupling of the adsorbed molecules from the highly reactive metallic substrate by the graphene allows us a direct imaging of their detailed **electronic structure** (Chap. 5). In the case of TCNQ adsorbed on graphene/Ru(0001), it was found a sizable charge transfer from the graphene to the single TCNQ molecules leading to the partial occupation of the LUMO of the neutral molecules. This charge transfer process does not occur for the same molecule on graphene/Ir(111) surface. The formation of a TCNQ monolayer can be understood then as a combination of hydrogen bonds and the delocalization of charge across a new spatially extended intermolecular band in the case of the TCNQ monolayer on graphene/Ru(0001). This intermolecular band is not developed for TCNQ monolayer on graphene/Ir(111) where the filling of the LUMO derived bands is rather small.

Finally, we focused on the study of the **magnetic properties** (Chap. 6) of TCNQ molecules on graphene/Ru(0001). We showed that isolated TCNQ molecules developed a magnetic moment due to the localization of an unpaired electron into its LUMO. The appearance of this magnetic moment was verified by measuring the corresponding Kondo resonance with local tunneling spectroscopy at low temperature. The role of the graphene layer in this process is

to transfer the precise charge to the molecules and modulate the coupling strength between the TCNQ and the underlying ruthenium substrate leading to a site dependent Kondo effect. This dependence was further confirmed for higher TCNQ coverages and for F_4-TCNQ molecules on the same surface. Upon completion of the TCNQ monolayer, the delocalization on the spatially extended bands preserves the parallel orientation of the electron spins. The existence of the corresponding long-range magnetic order on the TCNQ monolayer on graphene/Ru(0001) was detected by SP-STM experiments.

In summary, the results presented in this thesis provides a good insight into the control and the understanding of the growth of thin films of organic molecules on epitaxial graphene. These investigations illustrate also the power of LT-STM in the characterization at atomic scale of the electronic and magnetic properties of these organic systems. Remarkably, the manuscript presents the first experimental and theoretical evidence for the existence of long-range magnetic order in delocalized bands at temperatures above 4 K in a purely organic molecular monolayer deposited on epitaxial graphene. These findings paves the way to add new functionalities of graphene, a topic of the utmost interest these days.

8 Conclusiones

La exploración a nivel fundamental de las propiedades electrónicas y magnéticas de materiales orgánicos y su interacción con superficies, constituye una valiosa fuente de conocimiento para sus potenciales aplicaciones tecnológicas. Como primer paso en este campo, esta tesis presenta el estudio de moléculas aceptoras de electrones en grafeno epitaxial. En primer lugar, se creció y caracterizó las superficies de grafeno/Ru(0001) y grafeno/Ir(111) (Cap. 3) donde posteriormente se estudió la adsorción de las moléculas de TCNQ and F_4-TCNQ. Las propiedades estructurales, electrónicas y magnéticas de estos sistemas se investigaron mediante microscopía y espectroscopia túnel de vacío. Las principales conclusiones de cada uno de estos aspectos se describen a continuación.

En lo que respecta a las **propiedades estructurales** (Cap. 4), concluimos que el proceso de autoensamblado de las moléculas de TCNQ y F_4-TCNQ está gobernado por las propiedades de la capa de grafeno. En el caso de grafeno/Ir(111), la débil interacción entre la película de grafeno y el metal de debajo da lugar a una superficie electrónicamente homogénea donde la interacción intermolecular determina el orden. Por otro lado, las corrugaciones geométricas y electrónicas de la superficie de grafeno/Ru(0001) conduce, en las primeras etapas de crecimiento, a una adsorción preferencial de las moléculas en la superficie acabando en una estructura supramolecular estabilizada por la mutua interacción entre las moléculas.

Además, el desacoplo de las moléculas adsorbidas, de la superficie altamente reactiva del metal por parte del grafeno permite obtener una imagen detallada de su **estructura electrónica** (Cap. 5). Para las moléculas adsorbidas en grafeno/Ru(0001) se encontró una transferencia de carga considerable por parte del grafeno que da lugar a la ocupación parcial del LUMO de las moléculas neutras. Este proceso de transferencia de carga no sucede para la misma molécula en grafeno/Ir(111). Tras estos estudios, la formación de una monocapa de TCNQ en grafeno/Ru(0001) se puede entender como la combinación entre enlaces de hidrógeno y la deslocalización de carga a lo largo de una nueva banda intermolecular. Esta banda intermolecular no se forma en el caso de la monocapa de TCNQ en grafeno/Ir(111) donde el llenado de las bandas derivadas del LUMO es casi despreciable.

Por último, nos centramos en el estudio de las **propiedades magnéticas** (Cap. 6) de las TCNQ en grafeno/Ru(0001). Se demostró que las moléculas aisladas de TCNQ desarrollan un momento magnético a causa de la localización de un electrón desapareado en su LUMO. La aparición de este momento magnético se verificó mediante la medición por espectroscopia túnel local a baja temperatura de la resonancia Kondo correspondiente. El papel de

la capa de grafeno en este efecto es la transferencia de la carga adecuada y la modulación de la fuerza de acoplamiento entre la molécula y el sustrato de rutenio de debajo dando lugar a un efecto Kondo dependiente de la posición de adsorción. Esta dependencia fue confirmada para recubrimientos mayores de TCNQ y para moléculas de F_4-TCNQ en la misma superficie. Además, una vez completada la monocapa de TCNQ en grafeno/Ru(0001), la deslocalización en las bandas extendidas preserva el ordenamiento paralelo de los espines de los electrones. La existencia del correspondiente orden a largo alcance en la monocapa de TCNQ en grafeno/Ru(0001) es detectado mediante experimentos de STM polarizado en espín.

En resumen, los resultados presentados en esta tesis proporcionan una nueva perspectiva en el conocimiento sobre el control y crecimiento de películas delgadas de moléculas orgánicas sobre grafeno epitaxial. Estas investigaciones ilustran también el poder del LT-STM en la caracterización a nivel atómico de las propiedades electrónicas y magnéticas de estos sistemas orgánicos. En particular, este manuscrito presenta las primeras evidencias experimentales y teóricas de la existencia de un orden magnético de largo alcance en bandas deslocalizadas por encima de 4 K en una capa molecular puramente orgánica crecida en grafeno epitaxial. Estos descubrimientos abren las puertas a añadir nuevas funcionalidades al grafeno, un tema de gran interés en los últimos años.

Bibliography

[1] G. Binnig and H. Rohrer. Scanning Tunneling Microscopy. Helvetica Physica Acta **55**, 726 (1982). (cited on pages 1 and 5)

[2] J. Bardeen. Tunnelling from a many-particle point of view. Physical Review Letters **6**, 57 (1961). (cited on p. 6)

[3] J. Tersoff and D. R. Hamann. Theory of the scanning tunneling microscope. Physical Review B **31**, 805 (1985). (cited on p. 7)

[4] N. Lang. Spectroscopy of single atoms in the scanning tunneling microscope. Physical Review B **34**, 5947 (1986). (cited on p. 8)

[5] P. Gtütter, W. Hofer, and F. Rosei (editors) *Properties of Single Organic Molecules on Crystal Surfaces* (2006), imperial edition. (cited on p. 11)

[6] R. Wiesendanger. Spin mapping at the nanoscale and atomic scale. Reviews of Modern Physics **81**, 1495 (2009). (cited on pages 12, 17, and 102)

[7] D. Wortmann, S. Heinze, P. Kurz, G. Bihlmayer, and S. Blügel. Resolving Complex Atomic-Scale Spin Structures by Spin-Polarized Scanning Tunneling Microscopy. Physical Review Letters **86**, 4132 (2001). (cited on p. 12)

[8] J. Schwöbel, Y. Fu, J. Brede, A. Dilullo, G. Hoffmann, S. Klyatskaya, M. Ruben, and R. Wiesendanger. Real-space observation of spin-split molecular orbitals of adsorbed single-molecule magnets. Nature Communications **3**, 953 (2012). (cited on pages 14 and 101)

[9] C. Iacovita, M. Rastei, B. Heinrich, T. Brumme, J. Kortus, L. Limot, and J. Bucher. Visualizing the Spin of Individual Cobalt-Phthalocyanine Molecules. Physical Review Letters **101**, 116602 (2008). (cited on p. 14)

[10] F. Calleja. *Influencia de la estructura electrónica local en las propiedades de las superficies y su estudio mediante microscopía de efecto túnel*. Ph.D. thesis, Universidad Autónoma de Madrid (2007). (cited on pages 14 and 24)

[11] S. Barja. *Grafeno epitaxial en metales de transición: Estudio mediante microscopía y espectroscopia de efecto túnel.* Ph.D. thesis, Universidad Autónoma de Madrid (2012). (cited on pages 14, 29, 31, and 46)

[12] F. Himpsel, K. Christmann, P. Heimann, and D. E. Eastman. Adsorbate band dispersions for C on Ru(0001). Surface Science **115**, 59 (1982). (cited on p. 21)

[13] T. A. Land, T. Michely, R. J. Behm, J. C. Hemminger, and G. Comsa. Direct observation of surface reactions by scanning tunneling microscopy: Ethylene - ethylidyne - carbon particles - graphite on Pt (111). Journal of Chemical Physics **97**, 6775 (1992). (cited on p. 21)

[14] C. Oshima and A. Nagashima. Ultra-thin epitaxial films of graphite and hexagonal boron nitride on solid surfaces. Journal of Physics: Condensed Matter **9**, 1 (1997). (cited on p. 21)

[15] S. Hagstrom, H. Lyon, and G. A. Somorjai. Surface structures on the clean platinum (100) surface. Physical Review Letters **15**, 491 (1965). (cited on p. 21)

[16] J. T. Grant and T. W. Haas. A study of Ru(0001) and Rh(111) surfaces using LEED and AUGER electron spectroscopy. Surface Science **21**, 76 (1970). (cited on p. 21)

[17] A. E. Karu. Pyrolytic Formation of Highly Crystalline Graphite Films. Journal of Applied Physics **37**, 2179 (1966). (cited on p. 21)

[18] A. N'Diaye, S. Bleikamp, P. Feibelman, and T. Michely. Two-Dimensional Ir Cluster Lattice on a Graphene Moiré on Ir(111). Physical Review Letters **97**, 215501 (2006). (cited on pages 22, 25, 32, 33, 46, and 54)

[19] S. Marchini, S. Günther, and J. Wintterlin. Scanning tunneling microscopy of graphene on Ru(0001). Physical Review B **76**, 075429 (2007). (cited on pages 22, 23, 25, and 29)

[20] Y. S. Dedkov, M. Fonin, and C. Laubschat. A possible source of spin-polarized electrons: The inert graphene/Ni(111) system. Applied Physics Letters **92**, 052506 (2008). (cited on p. 22)

[21] K. S. Novoselov, A. K. Geim, S. V. Morozov, D. Jiang, Y. Zhang, S. V. Dubonos, I. V. Grigorieva, and A. A. Firsov. Electric field effect in atomically thin carbon films. Science **306**, 666 (2004). (cited on p. 22)

[22] A. Preobrajenski, M. L. Ng, A. S. Vinogradov, and N. Må rtensson. Controlling graphene corrugation on lattice-mismatched substrates. Physical Review B **78**, 073401 (2008). (cited on pages 22, 23, and 25)

[23] A. L. Vázquez de Parga, F. Calleja, B. Borca, M. C. G. Passeggi, J. J. Hinarejos, F. Guinea, and R. Miranda. Periodically Rippled Graphene: Growth and Spatially Resolved Electronic Structure. Physical Review Letters **100**, 056807 (2008). (cited on pages 23, 25, 27, 29, and 59)

[24] E. Sutter, D. P. Acharya, J. T. Sadowski, and P. Sutter. Scanning tunneling microscopy on epitaxial bilayer graphene on ruthenium (0001). Applied Physics Letters **94**, 133101 (2009). (cited on pages 23 and 29)

[25] B. Borca, S. Barja, M. Garnica, J. J. Hinarejos, A. L. Vázquez de Parga, R. Miranda, and F. Guinea. Periodically modulated geometric and electronic structure of graphene on Ru(0001). Semiconductor Science and Technology **25**, 034001 (2010). (cited on pages 23 and 29)

[26] W. Moritz, B. Wang, M.-L. Bocquet, T. Brugger, T. Greber, J. Wintterlin, and S. Günther. Structure Determination of the Coincidence Phase of Graphene on Ru(0001). Physical Review Letters **104**, 136102 (2010). (cited on pages 23 and 29)

[27] D. Martoccia, P. Willmott, T. Brugger, M. Björck, S. Günther, C. Schlepütz, A. Cervellino, S. Pauli, B. Patterson, S. Marchini, J. Wintterlin, W. Moritz, and T. Greber. Graphene on Ru(0001): A 25x25 Supercell. Physical Review Letters **101**, 126102 (2008). (cited on pages 23 and 25)

[28] D. Martoccia, M. Björck, C. M. Schlepütz, T. Brugger, S. A. Pauli, B. D. Patterson, T. Greber, and P. R. Willmott. Graphene on Ru(0001): a corrugated and chiral structure. New Journal of Physics **12**, 043028 (2010). (cited on pages 23 and 29)

[29] T. Brugger, S. Günther, B. Wang, J. H. Dil, M.-L. Bocquet, J. Osterwalder, J. Wintterlin, and T. Greber. Comparison of electronic structure and template function of single-layer graphene and a hexagonal boron nitride nanomesh on Ru(0001). Physical Review B **79**, 045407 (2009). (cited on pages 23, 28, and 29)

[30] B. Borca, S. Barja, M. Garnica, M. Minniti, A. Politano, J. M. Rodriguez-García, J. J. Hinarejos, D. Farías, A. L. Vázquez de Parga, and R. Miranda. Electronic and geometric corrugation of periodically rippled, self-nanostructured graphene epitaxially grown on Ru(0001). New Journal of Physics **12**, 093018 (2010). (cited on pages 23, 24, 29, and 42)

[31] B. Wang, M.-L. Bocquet, S. Marchini, S. Günther, and J. Wintterlin. Chemical origin of a graphene moiré overlayer on Ru(0001). Physical chemistry chemical physics **10**, 3530 (2008). (cited on pages 23, 28, and 29)

[32] D. Stradi, S. Barja, C. Díaz, M. Garnica, B. Borca, J. J. Hinarejos, D. Sánchez-Portal, M. Alcamí, A. Arnau, A. L. Vázquez de Parga, R. Miranda, and F. Martín. Electron localization in epitaxial graphene on Ru(0001) determined by moiré corrugation. Physical Review B **85**, 121404 (2012). (cited on p. 23)

[33] D. Stradi, S. Barja, C. Díaz, M. Garnica, B. Borca, J. J. Hinarejos, D. S. Portal, A. Arnau, A. L. Vázquez de Parga, R. Miranda, and F. Martín. Role of dispersion forces in the structure of graphene monolayers over Ru surfaces. Physical Review Letters **106**, 186102 (2011). (cited on pages 23, 26, 28, 29, 50, 60, and 63)

[34] P. Jakob, M. Gsell, and D. Menzel. Interactions of adsorbates with locally strained substrate lattices. The Journal of Chemical Physics **114**, 10075 (2001). (cited on p. 25)

[35] F. Calleja, J. J. Hinarejos, J. Ferrer, A. L. Vázquez de Parga, and R. Miranda. Relationship between strain and the surface electronic structure of Cu(111) films on Ru(0001): Theory and experiment. Physical Review B **71**, 125412 (2005). (cited on p. 25)

[36] D. Stradi. *Charge transfer between organic molecules and epitaxial graphene on metals*. Ph.D. thesis, Universidad Autónoma de Madrid (2013). (cited on pages 25, 38, 39, 60, 78, 79, 82, 83, 90, and 95)

[37] B. Borca, S. Barja, M. Garnica, D. Sánchez-Portal, V. Silkin, E. Chulkov, C. Hermanns, J. Hinarejos, A. L. Vázquez de Parga, A. Arnau, P. Echenique, and R. Miranda. Potential Energy Landscape for Hot Electrons in Periodically Nanostructured Graphene. Physical Review Letters **105**, 036804 (2010). (cited on pages 28, 29, 64, 83, and 90)

[38] D. Jiang, M. Du, and S. Dai. First principles study of the graphene/Ru(0001) interface. The Journal of chemical physics **130**, 074705 (2009). (cited on pages 28 and 29)

[39] G. Küppers, J., Wandelt, K. and Ertl. Influence of the Local Surface Structure on the 5p Photoemission of Adsorbed Xenon. Physical Review Letters **43**, 928 (1979). (cited on p. 28)

[40] S. Barja, M. Garnica, J. J. Hinarejos, A. L. Vázquez de Parga, N. Martín, and R. Miranda. Self-organization of electron acceptor molecules on graphene. Chemical Communications **46**, 8198 (2010). (cited on pages 30 and 46)

[41] E. Loginova, S. Nie, K. Thürmer, N. Bartelt, and K. McCarty. Defects of graphene on Ir(111): Rotational domains and ridges. Physical Review B **80**, 085430 (2009). (cited on pages 31 and 33)

[42] J. Coraux, A. T. N'Diaye, C. Busse, and T. Michely. Structural coherency of graphene on Ir(111). Nano letters **8**, 565 (2008). (cited on pages 31 and 32)

[43] A. T. N'Diaye, J. Coraux, T. N. Plasa, C. Busse, and T. Michely. Structure of epitaxial graphene on Ir(111). New Journal of Physics **10**, 043033 (2008). (cited on pages 31 and 32)

[44] A. T. N'Diaye, T. Gerber, C. Busse, J. Mysliveček, J. Coraux, and T. Michely. A versatile fabrication method for cluster superlattices. New Journal of Physics **11**, 103045 (2009). (cited on pages 32, 33, 46, and 54)

[45] P. Feibelman. Pinning of graphene to Ir(111) by flat Ir dots. Physical Review B **77**, 165419 (2008). (cited on pages 32 and 55)

[46] C. Busse, P. Lazić, R. Djemour, J. Coraux, T. Gerber, N. Atodiresei, V. Caciuc, R. Brako, A. N'Diaye, S. Blügel, J. Zegenhagen, and T. Michely. Graphene on Ir(111): Physisorption with Chemical Modulation. Physical Review Letters **107**, 036101 (2011). (cited on p. 33)

[47] I. Pletikosić, M. Kralj, P. Pervan, R. Brako, J. Coraux, A. N'Diaye, C. Busse, and T. Michely. Dirac Cones and Minigaps for Graphene on Ir(111). Physical Review Letters **102**, 056808 (2009). (cited on pages 33 and 34)

[48] A. T. N'Diaye, R. V. Gastel, A. J. Martínez-Galera, J. Coraux, H. Hattab, D. Wall, F.-J. M. Z. Heringdorf, M. H.-v. Hoegen, J. M. Gómez-Rodríguez, B. Poelsema, C. Busse, and T. Michely. In situ observation of stress relaxation in epitaxial graphene. New Journal of Physics **11**, 113056 (2009). (cited on p. 33)

[49] S. Lin, W. Spicer, and B. Schechtman. Electron escape depth, surface composition, and charge transfer in tetrathiafulvalene tetracyanoquinodimethane (TTF-TCNQ) and related compounds: Photoemission studies. Physical Review B **12**, 4184 (1975). (cited on p. 38)

[50] Z. Zhou, K. Xiao, R. Jin, D. Mandrus, J. Tao, D. B. Geohegan, and S. Pennycook. One-dimensional electron transport in Cu-tetracyanoquinodimethane organic nanowires. Applied Physics Letters **90**, 193115 (2007). (cited on p. 38)

[51] T.-C. Tseng, C. Lin, X. Shi, S. Tait, X. Liu, U. Starke, N. Lin, R. Zhang, C. Minot, M. Van Hove, J. Cerdá, and K. Kern. Two-dimensional metal-organic coordination networks of Mn-7,7,8,8-tetracyanoquinodimethane assembled on Cu(100): Structural, electronic, and magnetic properties. Physical Review B **80**, 155458 (2009). (cited on p. 38)

[52] M. M. Kamna, T. M. Graham, J. C. Love, and P. S. Weiss. Strong electronic perturbation of the Cu {111} surface by 7,7′,8,8′-tetracyanoquinonedimethane. Surface Science **419**, 12 (1998). (cited on p. 38)

[53] T.-C. Tseng, C. Urban, Y. Wang, R. Otero, S. L. Tait, M. Alcamí, D. Écija, M. Trelka, J. M. Gallego, N. Lin, M. Konuma, U. Starke, A. Nefedov, A. Langner, C. Wöll, M. A. Herranz, F. Martín, N. Martín, K. Kern, and R. Miranda. Charge-transfer-induced structural rearrangements at both sides of organic/metal interfaces. Nature chemistry **2**, 374 (2010). (cited on pages 38 and 62)

[54] I. F. Torrente, K. J. Franke, and J. I. Pascual. Structure and electronic configuration of tetracyanoquinodimethane layers on a Au(111) surface. International Journal of Mass Spectrometry **277**, 269 (2008). (cited on pages 38, 45, and 49)

[55] J. Mao, H. Zhang, Y. Jiang, Y. Pan, M. Gao, W. Xiao, and H.-J. Gao. Tunability of supramolecular Kagome lattices of magnetic phthalocyanines using graphene-based moire patterns as templates. Journal of the American Chemical Society **131**, 14136 (2009). (cited on p. 38)

[56] K. Yang, W. D. Xiao, Y. H. Jiang, H. G. Zhang, L. W. Liu, J. H. Mao, H. T. Zhou, and S. X. Du. Molecule-Substrate Coupling between Metal Phthalocyanines and Epitaxial Graphene Grown on Ru(0001) and Pt(111). The Journal of Physical Chemistry C **116**, 14052 (2012). (cited on pages 38, 48, and 54)

[57] A. J. Pollard, E. W. Perkins, N. a. Smith, A. Saywell, G. Goretzki, A. G. Phillips, S. P. Argent, H. Sachdev, F. Müller, S. Hüfner, S. Gsell, M. Fischer, M. Schreck, J. Osterwalder, T. Greber, S. Berner, N. R. Champness, and P. H. Beton. Supramolecular assemblies formed on an epitaxial graphene superstructure. Angewandte Chemie (International ed. in English) **49**, 1794 (2010). (cited on p. 38)

[58] M. Roos, B. Uhl, D. Künzel, H. E. Hoster, A. Groß, and R. J. Behm. Intermolecular vs molecule-substrate interactions: A combined STM and theoretical study of supramolecular phases on graphene/Ru(0001). Beilstein journal of nanotechnology **2**, 365 (2011). (cited on p. 38)

[59] S. K. Hämäläinen, M. Stepanova, R. Drost, P. Liljeroth, J. Lahtinen, and J. Sainio. Self-Assembly of Cobalt-Phthalocyanine Molecules on Epitaxial Graphene on Ir(111). The Journal of Physical Chemistry C **116**, 20433 (2012). (cited on p. 47)

[60] A. J. Martínez-Galera and J. M. Gómez-Rodríguez. Surface Diffusion of Simple Organic Molecules on Graphene on Pt(111). The Journal of Physical Chemistry C **115**, 23036 (2011). (cited on p. 48)

[61] H. Pinto, R. Jones, J. P. Goss, and P. R. Briddon. p-type doping of graphene with F4-TCNQ. Journal of Physics: Condensed Matter **21**, 402001 (2009). (cited on p. 50)

[62] B. n. Milián, R. Pou-Amérigo, R. Viruela, and E. Ortí. On the electron affinity of TCNQ. Chemical Physics Letters **391**, 148 (2004). (cited on p. 50)

[63] N. Koch, S. Duhm, J. Rabe, A. Vollmer, and R. Johnson. Optimized Hole Injection with Strong Electron Acceptors at Organic-Metal Interfaces. Physical Review Letters **95**, 237601 (2005). (cited on p. 50)

[64] B. Maennig, M. Pfeiffer, A. Nollau, X. Zhou, K. Leo, and P. Simon. Controlled p-type doping of polycrystalline and amorphous organic layers: Self-consistent description of conductivity and field-effect mobility by a microscopic percolation model. Physical Review B **64**, 195208 (2001). (cited on p. 50)

[65] W. Chen, S. Chen, D. C. Qi, X. Y. Gao, and A. T. S. Wee. Surface transfer p-type doping of epitaxial graphene. Journal of the American Chemical Society **129**, 10418 (2007). (cited on p. 50)

[66] C. Coletti, C. Riedl, D. S. Lee, B. Krauss, L. Patthey, K. von Klitzing, J. H. Smet, and U. Starke. Charge neutrality and band-gap tuning of epitaxial graphene on SiC by molecular doping. Physical Review B **81**, 235401 (2010). (cited on p. 50)

[67] K. Donner and P. Jakob. Structural properties and site specific interactions of Pt with the graphene/Ru(0001) moiré overlayer. The Journal of chemical physics **131**, 164701 (2009). (cited on p. 50)

[68] T. Katayama, K. Mukai, S. Yoshimoto, and J. Yoshinobu. Reactive rearrangements of step atoms by adsorption and asymmetric electronic states of tetrafluoro-tetracyanoquinodimethane on Cu(100). Physical Review B **83**, 153403 (2011). (cited on p. 52)

[69] S. Grimme. Semiempirical GGA-Type Density Functional Constructed with a Long-Range Dispersion Correction. Journal of Computational Chemistry **27**, 1787 (2006). (cited on p. 60)

[70] G. Mercurio, E. R. McNellis, I. Martin, S. Hagen, F. Leyssner, S. Soubatch, J. Meyer, M. Wolf, P. Tegeder, F. S. Tautz, and K. Reuter. Structure and Energetics of Azobenzene on Ag(111): Benchmarking Semiempirical Dispersion Correction Approaches. Physical Review Letters **104**, 036102 (2010). (cited on p. 60)

[71] K. Toyoda, I. Hamada, K. Lee, S. Yanagisawa, and Y. Morikawa. Density functional theoretical study of pentacene/noble metal interfaces with van der Waals corrections: vacuum level shifts and electronic structures. Journal of Chemical Physics **132**, 134703 (2010). (cited on p. 60)

[72] D. Sun, D.-H. Kim, D. Le, O. Borck, K. Berland, K. Kim, W. Lu, Y. Zhu, M. Luo, J. Wyrick, Z. Cheng, T. L. Einstein, T. S. Rahman, P. Hyldgaard, and L. Bartels. Effective elastic properties of a van der Waals molecular monolayer at a metal surface. Physical Review B **82**, 1201410(R) (2010). (cited on p. 60)

[73] J. D. Wuest and A. Rochefort. Strong adsorption of aminotriazines on graphene. Chemical communications **46**, 2923 (2010). (cited on p. 62)

[74] W. Tang, E. Sanville, and G. Henkelman. A grid-based Bader analysis algorithm without lattice bias. Journal of Physics: Condensed Matter **21**, 084204 (2009). (cited on p. 63)

[75] L. Limot, T. Maroutian, P. Johansson, and R. Berndt. Surface-State Stark Shift in a Scanning Tunneling Microscope. Physical Review Letters **91**, 196801 (2003). (cited on p. 64)

[76] C. Krull. *Electronic structure of metal phthalocyanines on Ag (100)*. Ph.D. thesis, Universitat Autònoma de Barcelona (2012). (cited on p. 64)

[77] A. Kahn, N. Koch, and W. Gao. Electronic Structure and Electrical Properties of Interfaces between Metals and π-Conjugated Molecular Films. Journal of Polymer Science: Part B: Polymer Physics **41**, 2529 (2003). (cited on p. 67)

[78] W. J. D. Haas, J. D. Boer, and G. V. D. Berg. The electrical resistance of gold, copper and lead at low temperatures. Physica **34**, 1115 (1934). (cited on pages 71 and 72)

[79] J. Kondo. Resistance Minimun in Dilute Magnetic Alloys. Progress of Theoretical Physics **32**, 37 (1964). (cited on pages 71 and 72)

[80] J. Li, W.-D. Schneider, R. Berndt, and B. Delley. Kondo Scattering Observed at a Single Magnetic Impurity. Physical Review Letters **80**, 2893 (1998). (cited on pages 71, 75, and 76)

[81] V. Madhavan, W. Chen, T. Jamneala, M. F. Crommie, and N. S. Wingreen. Tunneling into a Single Magnetic Atom: Spectroscopic Evidence of the Kondo Resonance. Science **280**, 567 (1998). (cited on pages 71, 75, 76, and 77)

[82] A. Zhao, Q. Li, L. Chen, H. Xiang, W. Wang, S. Pan, B. Wang, X. Xiao, J. Yang, J. G. Hou, and Q. Zhu. Controlling the Kondo effect of an adsorbed magnetic ion through its chemical bonding. Science (New York, N.Y.) **309**, 1542 (2005). (cited on pages 71, 76, and 77)

[83] V. Iancu, A. Deshpande, and S.-W. Hla. Manipulation of the Kondo Effect via Two-Dimensional Molecular Assembly. Physical Review Letters **97**, 266603 (2006). (cited on pages 71, 76, 77, and 88)

[84] L. Gao, W. Ji, Y. B. Hu, Z. H. Cheng, Z. T. Deng, Q. Liu, N. Jiang, X. Lin, W. Guo, S. X. Du, W. a. Hofer, X. C. Xie, and H.-J. Gao. Site-Specific Kondo Effect at Ambient Temperatures in Iron-Based Molecules. Physical Review Letters **99**, 106402 (2007). (cited on pages 71 and 76)

[85] R. Temirov, A. Lassise, F. B. Anders, and F. S. Tautz. Kondo effect by controlled cleavage of a single-molecule contact. Nanotechnology **19**, 065401 (2008). (cited on p. 71)

[86] I. Fernández-Torrente, K. Franke, and J. Pascual. Vibrational Kondo Effect in Pure Organic Charge-Transfer Assemblies. Physical Review Letters **101**, 217203 (2008). (cited on pages 71, 76, and 81)

[87] T. Choi, S. Bedwani, A. Rochefort, C.-Y. Chen, A. J. Epstein, and J. A. Gupta. A single molecule Kondo switch: multistability of tetracyanoethylene on Cu(111). Nano letters **10**, 4175 (2010). (cited on p. 71)

[88] P. W. Anderson. Localized Magnetic States in Metals. Physical rev **124**, 41 (1961). (cited on pages 72 and 73)

[89] A. C. Hewson. *The Kondo problem to Heavy Fermions* (Cambridge University Press, Cambridge, 1993). (cited on pages 73 and 74)

[90] P. W. Anderson. Local moments and localized states. Reviews of Modern Physics **50**, 191 (1978). (cited on pages 73 and 74)

[91] J. R. Schrieffer and P. A. Wolff. Relation between the Anderson and Kondo Hamiltonians. Physical Review **149**, 491 (1966). (cited on p. 74)

[92] L. Kouwenhoven and L. Glazman. Revival of the Kondo effect. Physics World **14**, 33 (2001). (cited on p. 75)

[93] U. Fano. Effect of Configuration interaction on Intensities and Phase Shifts. Physical Review **124**, 1866 (1961). (cited on p. 75)

[94] A. J. Heinrich, J. A. Gupta, C. P. Lutz, and D. M. Eigler. Single-atom spin-flip spectroscopy. Science (New York, N.Y.) **306**, 466 (2004). (cited on p. 76)

[95] D. Wegner, R. Yamachika, X. Zhang, Y. Wang, T. Baruah, M. Pederson, B. Bartlett, J. Long, and M. Crommie. Tuning Molecule-Mediated Spin Coupling in Bottom-Up-Fabricated Vanadium-Tetracyanoethylene Nanostructures. Physical Review Letters **103**, 087205 (2009). (cited on p. 76)

[96] J. Shuai-Hua, F. Ying-Shuang, Z. Tong, C. Xi, J. Jin-Feng, X. Qi-Kun, and M. Xu-Cun. Kondo Effect in Self-Assembled Manganese Phthalocyanine Monolayer on Pb Islands. Chinese Physics Letters **27**, 087202 (2010). (cited on p. 76)

[97] U. Perera, H. Kulik, V. Iancu, L. Dias da Silva, S. Ulloa, N. Marzari, and S.-W. Hla. Spatially Extended Kondo State in Magnetic Molecules Induced by Interfacial Charge Transfer. Physical Review Letters **105**, 106601 (2010). (cited on p. 76)

[98] Y. Jiang, Y. N. Zhang, J. X. Cao, R. Q. Wu, and W. Ho. Real-space imaging of Kondo screening in a two-dimensional O lattice. Science **333**, 324 (2011). (cited on p. 76)

[99] K. Nagaoka, T. Jamneala, M. Grobis, and M. Crommie. Temperature Dependence of a Single Kondo Impurity. Physical Review Letters **88**, 077205 (2002). (cited on p. 76)

[100] M. Ternes, A. J. Heinrich, and W.-D. Schneider. Spectroscopic manifestations of the Kondo effect on single adatoms. Journal of Physics: Condensed Matter **21**, 053001 (2009). (cited on p. 76)

[101] G. T. Rado and H. Suhl. *Magnetism. Vol. V: Magnetic Properties of Magnetic Alloys* (New York, 1993), academic p edition. (cited on p. 77)

[102] N. Knorr, M. Schneider, L. Diekhöner, P. Wahl, and K. Kern. Kondo Effect of Single Co Adatoms on Cu Surfaces. Physical Review Letters **88**, 096804 (2002). (cited on p. 77)

[103] Laila Souza de Mattos. *Correlated electrons probed by Scanning Tunneling Microscopy*. Ph.D. thesis, Standford University (2009). (cited on p. 77)

[104] T. O. Wehling, A. V. Balatsky, M. I. Katsnelson, A. I. Lichtenstein, and A. Rosch. Orbitally controlled Kondo effect of Co adatoms on graphene. Physical Review B **81**, 115427 (2010). (cited on p. 77)

[105] A. F. Otte, M. Ternes, K. von Bergmann, S. Loth, H. Brune, C. P. Lutz, C. F. Hirjibehedin, and A. J. Heinrich. The role of magnetic anisotropy in the Kondo effect. Nature Physics **4**, 847 (2008). (cited on p. 77)

[106] M. Garnica, D. Stradi, S. Barja, F. Calleja, C. Díaz, M. Alcamí, N. Martín, A. L. Vázquez de Parga, F. Martín, and R. Miranda. Long-range magnetic order in a purely organic 2D kayer adsorbed on epitaxial graphene. Nature Physics **9**, 368 (2013). (cited on pages 78, 79, 85, 90, 95, 96, 98, and 101)

[107] N. O. Lipari, C. Duke, R. Bozio, A. Girlando, C. Pecile, and A. Padva. Electron-Molecular-Vibration coupling in 7,7,8,8-Tetracyano-p-quinodimethane (TCNQ). Chemical Physics Letters **44**, 236 (1976). (cited on p. 81)

[108] M. Rice and N. O. Lipari. Electron-Molecular-Vibration Coupling in Tetrathiafulvalene-Tetracyanoquinodimethane (TTF-TCNQ). Physical review letters **38**, 437 (1977). (cited on p. 81)

[109] J. Paaske and K. Flensberg. Vibrational Sidebands and the Kondo Effect in Molecular Transistors. Physical Review Letters **94**, 176801 (2005). (cited on p. 81)

[110] J. Parks, A. Champagne, G. Hutchison, S. Flores-Torres, H. Abruña, and D. Ralph. Tuning the Kondo Effect with a Mechanically Controllable Break Junction. Physical Review Letters **99**, 026601 (2007). (cited on p. 81)

[111] A. Mugarza, C. Krull, R. Robles, S. Stepanow, G. Ceballos, and P. Gambardella. Spin coupling and relaxation inside molecule-metal contacts. Nature Communications **2**, 490 (2011). (cited on p. 88)

[112] A. Dilullo, S.-H. Chang, N. Baadji, K. Clark, J.-P. Klöckner, M.-H. Prosenc, S. Sanvito, R. Wiesendanger, G. Hoffmann, and S.-W. Hla. Molecular Kondo chain. Nano letters **12**, 3174 (2012). (cited on p. 89)

[113] P. Wahl, L. Diekhöner, M. Schneider, L. Vitali, G. Wittich, and K. Kern. Kondo Temperature of Magnetic Impurities at Surfaces. Physical Review Letters **93**, 176603 (2004). (cited on p. 93)

[114] C. Schneider, P. Bressler, P. Schuster, J. Kirschner, J. J. de Miguel, and R. Miranda. Curie temperature of ultrathin films of fcc-cobalt epitaxially grown on atomically flat Cu(100) surfaces. Physical Review Letters **64**, 1059 (1990). (cited on p. 93)

[115] N. Tsukahara, S. Shiraki, S. Itou, N. Ohta, N. Takagi, and M. Kawai. Evolution of Kondo Resonance from a Single Impurity Molecule to the Two-Dimensional Lattice. Physical Review Letters **106**, 187201 (2011). (cited on p. 93)

[116] J.-W. Yoo, C.-Y. Chen, H. W. Jang, C. W. Bark, V. N. Prigodin, C. B. Eom, and A. J. Epstein. Spin injection/detection using an organic-based magnetic semiconductor. Nature materials **9**, 638 (2010). (cited on p. 94)

[117] J. M. Manriquez, G. T. Yee, R. S. McLean, A. J. Epstein, and J. S. Miller. A room-temperature molecular/organic-based magnet. Science (New York, N.Y.) **252**, 1415 (1991). (cited on p. 94)

[118] R. Jain, K. Kabir, J. B. Gilroy, K. A. R. Mitchell, K.-C. Wong, and R. G. Hicks. High-temperature metal-organic magnets. Nature **445**, 291 (2007). (cited on p. 94)

[119] P. M. Allemand, K. C. Khemani, A. Koch, F. Wudl, K. Holczer, S. Donovan, G. Grüner, and J. D. Thompson. Organic molecular soft ferromagnetism in a fullerene C60. Science **253**, 301 (1991). (cited on p. 94)

[120] R. Arita, Y. Suwa, K. Kuroki, and H. Aoki. Gate-Induced Band Ferromagnetism in an Organic Polymer. Physical Review Letters **88**, 127202 (2002). (cited on p. 94)

[121] F. H. L. Essler, H. Frahm, F. Göhmann, A. Klümper, and V. E. Korepin. *The One-Dimensional Hubbard model* (2005), cambridge edition. (cited on p. 94)

[122] Y. Nagaoka. Ferromagnetism in a Narrow, Almost Half-Filled s Band. Physical Review **147**, 392 (1966). (cited on p. 94)

[123] E. H. Lieb. Two Theorems on the Hubbard Model. Physical Review Letters **62**, 1201 (1989). (cited on p. 94)

[124] A. Mielke. Ferromagnetism in the Hubbard model on line graphs and further considerations. Journal of Physics A: Mathematical and General **24**, 3311 (1991). (cited on p. 94)

[125] H. Tasaki. Ferromagnetism in the Hubbad Models with Degenerate Single-Electron Ground States. Physical Review Letters **69**, 1608 (1992). (cited on p. 94)

[126] M. Bode, R. Pascal, M. Getzlaff, and R. Wiesendanger. Surface state of Gd(0001) films on W(110): Scanning tunneling spectroscopy study. Acta Physica Polonica **93**, 273 (1998). (cited on p. 102)

Publications

1. "*Periodically modulated geometric and electronic structure of graphene on Ru(0001)*"

   B. Borca, S. Barja, M. Garnica, J. J. Hinarejos, A. L. Vázquez de Parga, R. Miranda and F. Guinea.
   Semiconductor Science and Technology **25**, 034001 (2010).

2. "*Electronic and geometric corrugation of periodically rippled, self-nanostructured graphene epitaxially grown on Ru(0001)*"

   B. Borca, S. Barja, M. Garnica, M. Minniti, A. Politano, J.M. Rodríguez, J. J. Hinarejos, D. Farías, A.L. Vázquez de Parga and R. Miranda.
   New Journal of Physics **12**, 036804 (2010).

3. "*Potential Energy Landscape for Hot Electrons in Periodically Nanostructured Graphene*"

   B. Borca, S. Barja, M. Garnica, D. Sánchez-Portal, V. M. Silkin, E. V. Chulkov, F. Hermanns, J. J. Hinarejos, A. Arnau, P. M. Echenique, A. L. Vázquez de Parga and R. Miranda.
   Physical Review Letters **105**, 036804 (2010).

4. "*Borca et al. Reply*"

   B. Borca, S. Barja, M. Garnica, D. Sánchez-Portal, V. M. Silkin, E. V. Chulkov, F. Hermanns, J. J. Hinarejos, A. Arnau, P. M. Echenique, A. L. Vázquez de Parga and R. Miranda.
   Physical Review Letters **105**, 219702 (2010).

5. "*Self-organization of electron acceptor molecules on graphene*"

   S. Barja, M. Garnica, J. J. Hinarejos, A. L. Vázquez de Parga, N. Martín and R. Miranda.
   Chemical Communication, **46**, 8198 (2010).

6. "*Role of Dispersion Forces in the Structure of Graphene Monolayers on Ru Surfaces*"

   D. Stradi, S. Barja, C. Díaz, M. Garnica, B. Borca, J. J. Hinarejos, D. Sánchez-Portal, M. Alcamí, A. Arnau, A. L. Vázquez de Parga, R. Miranda and F. Martín.
   Physical Review Letters **106**, 186102 (2011).

7. "*Electron localization in epitaxial graphene on Ru(0001) determined by moiré corrugation*"

   D. Stradi, S. Barja, C. Díaz, M. Garnica, B. Borca, J. J. Hinarejos, D. Sánchez-Portal, M. Alcamí, A. Arnau, A. L. Vázquez de Parga, R. Miranda and F. Martín.
   Physical Review B. **85**, 121404(R) (2010).

8. "*Highly reproducible low temperature scanning tunneling microscopy and spectroscopy with in situ prepared tips*"

   A. Castellanos-Gomez, G. Rubio-Bollinger, M. Garnica, S. Barja, A. L. Vázquez de Parga, R. Miranda and N. Agraït.
   Ultramicroscopy **112**, 1 (2012).

9. "*Periodic spatial variation of the electron-phonon interaction in epitaxial graphene on Ru(0001)*"

   A. Castellanos-Gomez, G. Rubio-Bollinger, M. Garnica, S. Barja, A. L. Vázquez de Parga, R. Miranda and N. Agraït.
   Applied Physics Letter **102**, 063114 (2013).

10. "*Long-range magnetic order in a purely organic 2D layer adsorbed on epitaxial graphene*"

    M. Garnica, D. Stradi, S. Barja, F. Calleja, C. Díaz, M. Alcamí, N. Martín, A. L. Vázquez de Parga, F. Martín and R. Miranda.
    Nature Physics, **9**, 368 (2013).

11. "*Ordered arrays of metal-organic magnets at surfaces*"

    S. Barja, D. Stradi, B. Borca, M. Garnica, C. Díaz, J. M. Rodríguez-García, M. Alcamí, A. L. Vázquez de Parga, F. Martín and R. Miranda.
    Journal of Physics: Condensed Matter, accepted (2013).

Agradecimientos/Acknowledgments

Ha sido mucha la gente que ha contribuido, de una u otra manera, a que hoy esta tesis esté acabada y a todos ellos quiero agradecérselo.

A Amadeo López quiero agradecerle profundamente que me diese la oportunidad de entrar en este mundo, así como su dedicación y paciencia durante estos años. A Rodolfo Miranda le agradezco su disposición en todo momento. Su pasión por la ciencia es algo altamente contagioso. A Juan José Hinarejos le agradezco todo el trabajo dedicado sin el cual esta tesis nunca hubiese sido posible. Me siento realmente afortunada de haber tenido la oportunidad de aprender tanto a tu lado.

A todos los miembros del Laboratorio de Superficies y de IMDEA-Nanociencia, los que ya se fueron y los que acaban de llegar, por contribuir siempre a un magnífico ambiente de trabajo. En especial a Sara por abrirme las puertas en el labo y por todos los años junto a Luisete. Parte de esta tesis es también tuya. A Fabián, con quien he tenido la oportunidad de compartir y aprender mucho en estos últimos tiempos. A Roberto Otero y José María Gallego por las fructíferas discusiones en los journal clubs. A Nikolai, por sus buenos consejos y su gran ayuda con Latex y Mathematica. A Isabel Rodríguez, José Luis Casillas, María Jesús Villa y Bonifacio Vega por su permanente disponibilidad. A Amjad por su ayuda con mi inglés y su amistad. Y a Jonathan y Miguel Ángel, los perfectos compañeros de despacho.

A todos los técnicos del departamento de Física de la Materia Condensada, José Rodríguez, Santiago Márquez, Andrés Buendía, José Luis Romera, Rosa Díez y Juan Benayas, y de los talleres del SEGAINVEX, en especial al servicio de criogenia, por su indudable labor para el desarrollo de esta tesis. A Elsa Sánchez-Fuentes por su entera disposición ante cualquier trámite o consulta.

A todas las personas con las que he tenido oportunidad de colaborar. Al equipo teórico de San Sebastián y del Departamento de Química de la UAM sin los que entender todo lo descrito en esta tesis no hubiese sido posible. En especial a Andrés Arnau por su entusiasmo y discusiones que han resultado fundamentales para el desarrollo de esta tesis y a Daniele Stradi, compañero de fatigas, por revelarme todos los misterios del DFT. También agradezco a Andrés Castellanos, Gabino Rubio-Bollinger y Nicolás Agraït de cuya colaboración ha salido un bonito trabajo. Y a Anna de cuya colaboración nació una amistad que espero dure mucho, te deseo lo mejor en el futuro.

I want to thank to Roman Fasel and Pascal Ruffieux for giving me the opportunity to visit their group, and for their hospitality. During my stay in Zürich, I had the opportunity to

obtain really interesting results part of them are included in this thesis. The friendly and innovate atmosphere of the nanotech@surfaces group made my stay very profitable and enjoyable. In particular, I would like to thank Jimmy, Hajo, Fréderic, Lukas, Roland, Thomas and Jan for their dedication and our time together in and outside of the lab. Gracias también a Juanra por abrirme las puertas al grupo de españoles y hacerme sentir como en casa.

A las chicas: Bogdana, Erika, Cecilia, Jose, Fabiola y Cintia. Si algo bueno me llevo de esta tesis es haber tenido la oportunidad de conoceros. A Bogdana quien ha sido para mi como una hermana mayor de la ciencia, espero haber podido heredar tu pasión y entrega por todo lo que haces. A Erika y su eterna sonrisa, por siempre sacar un momento para mi. A Cecilia, por su claridad y buenos consejos. Y a Jose, quien con su manera de ver la vida me ha hecho entender qué es lo importante.

A todos los compañeros de la carrera y el máster con los que he pasado tan buenos momentos. Muy especialmente a los chicos de las mesas quienes han sido fundamentales en estos últimos años. A Paloma, con quien he tenido la oportunidad de compartir muchas cosas entre ellas largas horas de biblioteca, gracias porque este camino ha sido más fácil contigo al lado. A Yago, quien con su visión práctica siempre consigue que entienda mejor las cosas. A Fito, con quien discutir es un placer y reír mucho más. A Miguel, por todos esos viajes en coche juntos donde pacientemente me escuchaba, gracias. Al equipo de biofísica: Paula, Adriana y Vicky, porque sois la alegría de la huerta. A Edu y Luis por ser una fuente incansable de diversión. Y a aquellos que en la distancia todavía siguen ahí: Drino, Peibol, Alba, Pepe (y su flow), Emilio y Clara.

A Clara por estar ahí a lo largo de los años. La próxima visita te toca a ti. A mis pejinucas, Inés y Julia, y a sus Javis. Gracias por saber que puedo contar con vosotros en cualquier momento y por las risas que nos hemos echado y nos echaremos.

A mi otra familia, el grupo scout Águila. Creo que no hubiese podido afrontar de mejor manera lo que hacer la tesis significa sin todo lo que en el grupo he aprendido. Gracias a todos de principio a fin, a los que me aguantaron de pequeña como a los que me han tenido que aguantar de mayor. Muy especialmente al grupo de las quedadas y, por supuesto, a la familia de Zaragoza.

A mi gran familia. Muy especialmente a mis abuelas, Carmiña y Tere, quienes aunque nunca entendieron lo que he hecho durante estos años siempre me han animado. A mi familia política quienes me han visto crecer y aguantado. Gracias Pilar, Jose y Marta por vuestro cariño. A mis "sisters", Marta y Carmen, gracias por siempre intentar sacarme una sonrisa aunque a veces me resista. Seré la mayor pero yo también he aprendido mucho de vosotras. A mis padres, sin cuyo apoyo incondicional hubiese sido imposible llegar hasta aquí. Gracias por apoyarme en cada una de mis decisiones y por esforzaros por entenderme. Y ya por último, gracias Nacho. Gracias por estar siempre ahí, por cuidarme, por quererme y por todo tu trabajo detrás de esta tesis.